# COMPUTATIONAL ASPECTS OF THE INTEGRATED
# MULTI-DISCIPLINARY DESIGN OF A TRANSPORT WING

by

Eric Robert Unger

Thesis submitted to the Faculty of the

Virginia Polytechnic Institute and State University

in partial fulfillment of the requirements for the degree of
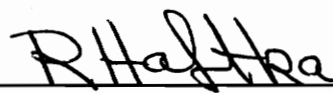
## MASTER OF SCIENCE

in

Aerospace Engineering

APPROVED:

B. Grossman, Chairman

R. T. Haftka          W. H. Mason

March, 1990

Blacksburg, Virginia

C.2

# COMPUTATIONAL ASPECTS OF THE INTEGRATED MULTI-DISCIPLINARY DESIGN OF A TRANSPORT WING

by

Eric Robert Unger

Committee Chairman: Bernard Grossman

Aerospace Engineering

(ABSTRACT)

Past research at this university has proven the feasibility of multi-disciplinary design of a complex system involving the complete interaction of aerodynamics and structural mechanics. Critical to this design process, is the ability to accurately and efficiently calculate the sensitivities of the involved quantities (such as drag and dynamic pressure) with respect to the design variables. These calculations had been addressed in past research, but it was felt that insufficient accuracy had been obtained. The focus of this research was to improve the accuracy of these sensitivity calculations with a thorough investigation of the computational aspects of the problem. These studies led to a more complete understanding of the source of the errors that plagued previous results and provided substantially improved sensitivity calculations.

Additional research led to an improvement in the aerodynamic–structural interface which aided in the accuracy of the sensitivity computations. Furthermore, this new interface removed discontinuities in the calculation of the drag which the previous model tended to yield. These improvements were made possible with application of shape functions in surface deflection analysis, instead of the previous

'zonal' approach. Other factors which led to accuracy improvements were changes to the aerodynamic model and the paneling scheme.

Final studies with the optimization process demonstrated the ability of the improved sensitivities to accurately approximate the design problem and provided useful results. Additional studies on the optimization process itself provided information on move limit restrictions and various constraint problems.

# ACKNOWLEDGEMENTS

# TABLE OF CONTENTS

# LIST OF FIGURES

# LIST OF TABLES

# LIST OF SYMBOLS

$\mathbf{A}$ – Aerodynamic influence matrix

$\mathbf{A}'$ – Derivative of the $\mathbf{A}$ matrix with respect to $p$

$AR$ – Aspect ratio

$b$ – Total wing span

$c$ – Local wing chord

$c'$ – Thrust specific fuel consumption

$\mathbf{C}$ – Geometric influence matrix for induced velocities

$C_d$ – Section drag coefficient

$C_D$ – Drag coefficient

$C_D'$ – Incompressible drag coefficient

$C_{D_{a/c_0}}$ – Drag coefficient of reference aircraft at $\alpha = 0°$

$C_{D_{ft}}$ – Drag coefficient of fuselage and tail

$C_{D_{ft}}$ – Drag coefficient of fuselage and tail

$C_{D_i}$ – Induced drag coefficient

$C_{D_v}$ – Viscous drag coefficient

$C_l$ – Section lift coefficient

$C_L$ – Lift coefficient

$C_L'$ – Incompressible lift coefficient

$C_P$ – Pressure coefficient

$C_P'$ – Incompressible pressure coefficient

$dl$ – Vector length of vortex filament

$D$ – Drag

$D_{ind_j}$ – Induced drag on $j^{th}$ panel

$D_m$ – Drag at optimum range altitude

$\mathbf{D}$ – Interface transformation matrix for shape function approach

$\mathbf{D}_0$ – Interface transformation matrix for previous approach

$e$ – Span efficiency

$f_1$ – Aerodynamic 'black box'

$f_2$ – Balanced flight equation

$f_3$ – Structural 'black box'

$F_a$ – Force at load set nodes

$F_{aD}$ – Force at load set nodes at divergence

$F_{ar}$ – Force at load set nodes for rigid wing conditions

$F_{z_i}$ – Force at $i^{th}$ aerodynamic control point

$F_I$ – Gravitational and inertial force vector

$F_z$ – Lift forces at aerodynamic control points

$g_s$ – Vector of design constraints

$\mathbf{I}$ – Identity matrix

$\mathbf{J}$ – Jacobian matrix

$\mathbf{K}$ – Stiffness matrix

$l_i$ – Section lift on $i^{th}$ aerodynamic control point

$L$ – Lift

$L_i$ – Lift on $i^{th}$ aerodynamic control point

$M_\infty$ – Freestream Mach number

$n$ – Load factor

$n_a$ – Number of aerodynamic panels

$n_p$ – Number of design variables

$p$ – Vector of design variables

$q$ – Dynamic pressure

$q_D$ – Divergence dynamic pressure

$q_m$ – Dynamic pressure at optimum range altitude

$\mathbf{r}$ – Position vector to vortex filament

$r_{cp}$ – Perpendicular distance for control point to vortex filament

$\mathbf{R}$ – Incremental aerodynamic force vector

$R_c$ – Calculated design aircraft range

$R_r$ – Reference aircraft range

$S$ – Total wing area

$\mathbf{S}$ – Flexibility matrix

$\mathbf{S}'$ – Derivative of flexibility matrix with repect to $\mathbf{p}$

$\mathbf{T}$ – Boolean matrix

$U$ – Vector of displacements

$U_\infty$ – Freestream velocity vector

$V$ – Velocity vector induced by vortex filament

$V_c$ – Cruise velocity

$V_{j_{ind}}$ – Induced velocity vector at $j^{th}$ aerodynamic control point

$V_r$ – Required wing volume

$V_s$ – Wing volume

$W_{0r}$ – Reference aircraft total weight

$W_h$ – Total aircraft weight at half fuel condition

$W_p$ – Payload weight

$W_t$ – Total aircraft weight

$W_{uf}$ – Usable fuel weight

$W_w$ – Design wing weight

$W_{wr}$ – Reference aircraft wing weight

$x, y, z$ – Cartesian coordinates

$x', y', z'$ – Transformed coordinates

$\hat{i}, \hat{j}, \hat{k}$ – Unit vectors in cartesian coordinates

$\hat{n}$ – Unit normal vector

$\alpha$ – Angle of attack

$\alpha_r$ – Rigid angle of attack

$\beta$ – $\sqrt{1 - M_\infty^2}$

$\boldsymbol{\Gamma}$ – Vorticity vector

$\boldsymbol{\Gamma}_i$ – Vorticity vector on $i^{th}$ panel

$\kappa$ – $dC_D/dC_L$

$\phi$ – Perturbation velocity potential

$\phi'$ – Incompressible perturbation velocity potential vector

$\boldsymbol{\Psi}$ – Vector of shape functions

$\rho_\infty$ – Freestream density

$\boldsymbol{\theta}$ – Vector of displacements at the load set nodes

$\xi, \eta$ – normalized coordinates

# 1. INTRODUCTION

In an ideal world, an aircraft would perform its mission in an optimal fashion. The designer would have perfectly balanced the demands of performance, cost, and safety in all respects through complete analysis of the various behavior characteristics of the project. Since an improvement in one characteristic frequently degrades another, this designer would apply optimization techniques to simple and exact equations which define the interactions within the problem. The result would be the best design which meets the requirements with a minimal amount of effort.

Unfortunately, in all but the most trivial problems, this process is virtually impossible. In a general problem, even the concept of a 'perfect' balance of characteristics is ill defined. At best, a set of desirable attributes is selected and the designer attempts to satisfy requirements as best as possible. But problem specification is the least of the designers' challenges. The majority of the difficulty lies in the fact that the trade-off analysis is generally a tremendously complicated process since exact equations which clearly define the interactions are rarely encountered. To further exacerbate the problem, many vehicles exhibit a cross interaction between several disciplines (such as interactions between aerodynamics and structural mechanics). For a design to be successful in the modern world, these interactions must be analyzed with available knowledge and resources.

The modern design process relies on a keen sense of intuition and experience to account for as much of an aircraft's behavior as possible. This approach does an excellent job where one discipline is involved. For example, with a well defined planform and load requirements, current optimization techniques have been successful at designing a minimum weight wing. The weakness in this design process

is the limited consideration of multi-disciplinary effects beyond the preliminary design phase. While it is obvious that a vast number of very successful aerospace vehicles have been achieved within this limitation, inclusion of multi-disciplinary effects during the design phase should enhance the final product. Furthermore, the increased use of composite materials in aircraft construction has virtually made such considerations a requirement. Vehicles built from such composite materials have strong aeroelastic interactions which must be accounted for. A great barrier to the inclusion of these effects, has been the tremendous cost considerations due to a lack of efficient multi-disciplinary design techniques.

Past research at this university has focused on efficient multi-disciplinary design optimization. The first example of this focus was the design of a sailplane wing.[1] In this example, the aerodynamic and structural models were kept simple (lifting line theory for the aerodynamics, and beam theory for the structures) to demonstrate the feasibility and superiority of the approach. The complexity of the design problem was increased by incorporating a vortex lattice method for the aerodynamics and a finite element model for the structures.[2] This increase in complexity resulted in a design problem which would have been prohibitively expensive had not approximate optimization techniques and new cross sensitivity analysis been employed.[3] The research was then further continued in the design of a forward swept transport wing.[4,5,&6] Although this model still retained the vortex lattice and finite element models, additional complexity was introduced through a refinement of the aeroelastic interaction. Work progressed to incorporate more efficient cross-sensitivity analysis through the use of a modular sensitivity approach which treats each separate discipline as a 'black box'.[4,5,&6] Reference 4 demonstrated the advantages of the new analysis and proved the feasibility and success of designing the significantly more complex system. Unfortunately, Ref. 4 contained results where the

accuracy of the sensitivities was not very good, and it was felt that this aspect of the research should be improved. Furthermore, the drag calculations tended to yield discontinuities as the design parameters changed and values which seemed low.

This study builds on the work of Ref. 4 and attempts to correct the problems present in that study. A detailed analysis of the numerical calculations required for the design problem is made with an emphasis on the aerodynamics and the aerodynamic-structural interface. This detailed analysis has revealed the source of the errors in Ref. 4 and provides further information on the behavior of the optimization process. In addition, this study has included the divergence sensitivity calculations which were absent in past research for the transport wing.

Chapter 2 outlines the entire design problem to provide necessary background to begin the design process. Chapter 3 details the aerodynamic model and highlights the structural model. In this chapter the problems in the past aerodynamic model are discussed and corrected to provide more consistent results. Chapter 4 outlines the aeroelastic formulation as found in Ref. 6. Chapter 5 makes an indepth study of the aerodynamic-structural interface and replaces the past model with a model that employs surface shape functions. Chapter 6 presents the drag sensitivity analysis and calculations. This chapter considers the results obtained in the previous research and generates improvements through a careful reexamination of the details of the finite differencing process. In addition, the effects of the new interface model are studied. Chapter 7 follows along the lines of chapter 6, dealing with the divergence calculations. In this chapter, the unique problems associated in the numerical calculations of the divergence sensitivity is addressed. Chapter 8 gives the details involved with the approximate optimization process and presents the optimization results, old and new. An additional analysis on move limit size and the addition of constraints is also discussed. The final chapter outlines the results obtained, and reflects on the impact they made on the drag and divergence approximations and the final optimization cycles.

# 2.   THE DESIGN PROBLEM

## 2.0. Introduction

In the detailed analysis which will follow in the next few chapters, it is important not to lose sight of the design problem as a whole. The goal is to design a minimum weight aircraft which meets several constraints. The resulting design will be compared to a reference aircraft[7] whose characteristics are given in table 2.1. A major difference between the reference wing and the current one is the sweep. The present design wing has a forward sweep at the initial design point while the reference aircraft has a standard aft sweep. The initial assignment of forward sweep may bring more aeroelastic effects into consideration during the optimization process. Due to the excessive computational costs associated with transonic analysis, the Mach number for the design will be limited to .48 while the reference aircraft has a design Mach number of .78. The following sections detail the set-up of the design problem and its associated objective and constraint functions.

**Table 2.1.** Reference Aircraft Design Specifications

| Average Cruise Conditions | |
|---|---|
| Mach Number | 0.78 |
| Lift Coefficient | 0.672 |
| L/D (Lift to Drag Ratio) | 20.7 |
| $c'$ (Specific Fuel Consumption) | 0.430 |

| Weights(N) | | Wing/Tail Data | |
|---|---|---|---|
| | | Aspect Ratio | 14.0 |
| Gross Weight | $4.494 \times 10^5$ | Area(m$^2$) | 84.0 |
| Std. Empty Weight | $2.852 \times 10^5$ | Span(m) | 34.3 |
| Wing Weight | $3.020 \times 10^4$ | Sweep at c/4, (deg) | 15.0 |
| Usable Fuel Weight | $2.738 \times 10^4$ | Taper Ratio | 0.25 |
| Payload Weight | $1.368 \times 10^5$ | Thickness(%) | 12.0 |
| | | Horiz. Tail Area (m$^2$) | 11.71 |
| | | Vert. Tail Area (m$^2$) | 17.74 |
| **Range(m):** | | | $2.34 \times 10^6$ |

## 2.1. The Design Variables and Wing Layout

For any optimization problem, a set of variables must be selected which can be changed to modify the problem. These terms are known as the design variables and the forward-swept transport wing has 39 (see table 2.2). The first 6 define the planform of the wing (see Fig. 2.1), and the next two give the twist at the wing breakpoint and tip. These twist variables are included so the optimization can define a 'jig shape', thus allowing the wing to deform into an optimal shape.
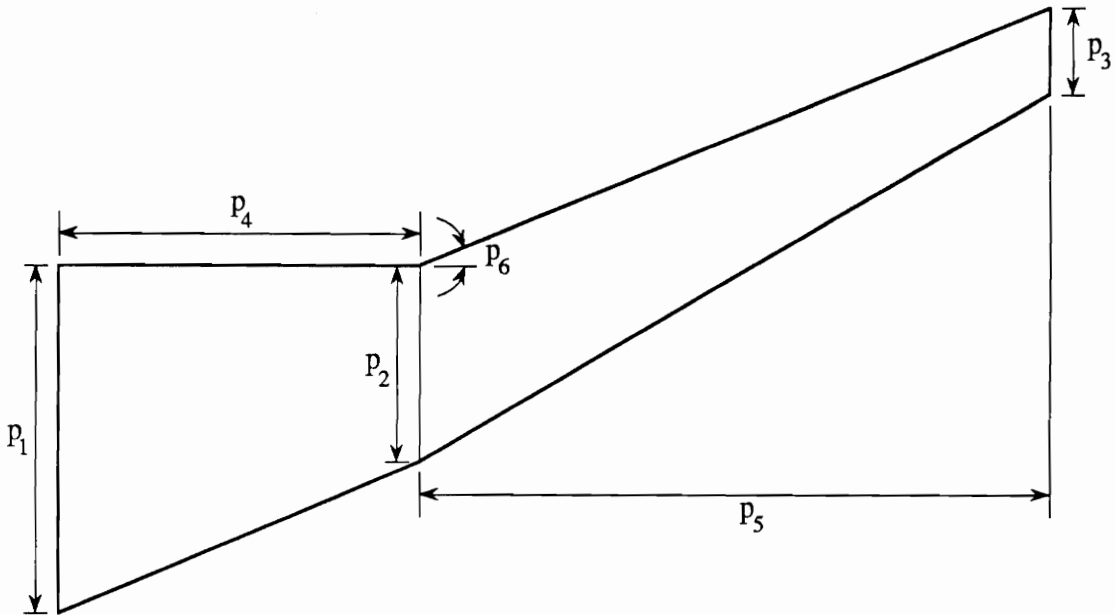


**Figure 2.1.** Planform Design Variables

Design variables 9 and 10 represent performance quantities, with the first representing the cruise dynamic pressure, and the second giving the usable fuel. The dynamic pressure optimization is referred to in section 2.4 and is essential to the calculation of the optimal range.

The remaining 29 variables represent the structural panel thicknesses, the spar cap areas, and the ply orientation. The panels are organized by dividing the wing

into four sections, with two inboard the break and two outboard (See Fig. 2.2 where A-A divides the wing inboard the break and B-B divides the wing outboard the break). Each of these sections is covered in a graphite-epoxy laminate with plies of $0°$, $\pm 45°$, and $90°$. The thickness of each of these plies is an independent design variable which gives a total of 24 (12 for the upper surface and 12 for the lower surface). The next four variables represent the cap areas for each of the spars, and the last design variable gives the reference orientation of the $0°$ ply with respect to the chord normal. The internal layout of the wing is held constant (i.e. the number of spars, ribs, panels, etc.), but the shape of the arrangement changes as the wing planform is changed (see Fig. 2.2).
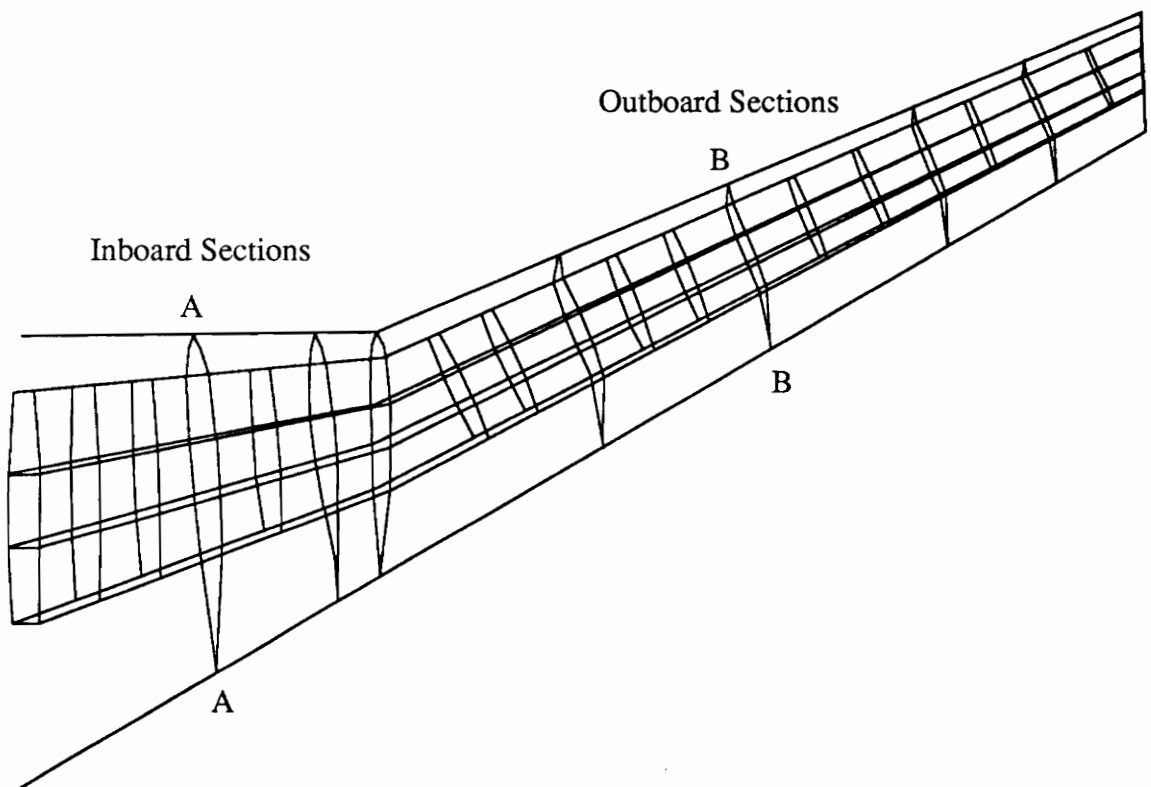


**Figure 2.2.** Structural Layout of the Wing

**Table 2.2.** Design Variables for the Forward-Swept Wing Transport

| Planform Design Variables | Performance Design Variables |
|---|---|
| 1. Chord length at the root | 9. Dynamic pressure at cruise |
| 2. Chord length at the break | 10. Usable fuel weight |
| 3. Chord length at the tip | **Structural Design Variables** |
| 4. Distance from root to break | 11–34. Panel thicknesses |
| 5. Distance from break to tip | 35–38. Spar cap areas |
| 6. Sweep angle at the break | 39. Ply orientation |
| 7. Jig twist at the break w.r.t. root | |
| 8. Jig twist at the tip w.r.t. break | |

## 2.2. The Objective Function

As mentioned previously, the objective of the design is to minimize the total weight of the aircraft. The total weight is given by the summation of the aircraft empty weight, $W_0$, the usable fuel weight, $W_{uf}$, and the payload weight, $W_p$.

$$W_t = W_0 + W_{uf} + W_p \tag{2.1}$$

The empty weight is calculated with the use of the empty weight of the reference aircraft, $W_{0r}$, by subtracting the wing weight savings times a growth factor, $\eta$. The justification for this factor lies in the fact that as the structural wing weight is decreased, weight associated with the rest of the aircraft will also be reduced. Therefore, we express $W_0$ as:

$$W_0 = W_{0r} - \eta(W_{wr} - W_w) \tag{2.2}$$

where $W_{0r}$ and $W_{wr}$ give the empty weight and wing weight for the reference aircraft, and $W_w$ gives the wing weight for the design aircraft. The amplification factor, $\eta$, is selected to be 2 as in Ref. 6.

## 2.3. The Design Constraints

Simply put, the structural constraints require the wing to not fail during during a 2.5g maneuver at 2.5 times the cruise dynamic pressure. The factor of 2.5 is included due to FAA requirements (this maneuver is assumed to occur during a dive). In addition, these constraints must allow for a factor of safety of 1.5. The strain constraints are applied to the skin plies and require a maximum strain of .012 in the normal and fiber directions, and in shear. The stress constraints are applied to the internal spar caps with .262 GPa. being the allowable maximum. An additional constraint requires the divergence speed to be 1.2 times the maneuver speed.

The range constraint is that which drives the aerodynamic design. This constraint is set to be equal to that of the reference aircraft at $2.34 \times 10^3$Km. The range is calculated assuming the drag is proportional to the weight during the cruise phase, with the constant of proportionality being calculated when half of the usable fuel is burned off. The following section details the range calculation

## 2.4. The Range Calculation

The range calculation considered here is exactly the same as that of Ref. 6. The calculation begins by assuming the changes in aircraft weight (due to the burning of fuel) have a negligible effect on the elastic deformation. With this assumption we can write:

$$D = qSC_D(C_L) \tag{2.3}$$

where $q$ is the cruise dynamic pressure, $S$ is the wing area, and $C_D$ is the drag coefficient which is a function of only the lift coefficient $C_L$. Since the cruise is in balanced flight we have that the lift coefficient is

$$C_L = \frac{W}{qS} \tag{2.4}$$

where $W$ is the aircraft's total weight. By differentiating $D$ with respect to $q$, and setting the result equal to zero,

$$SC_D - \frac{W}{q}\frac{dC_D}{dC_L} = 0 \qquad (2.5)$$

and

$$q_m = \frac{W}{SC_D}\frac{dC_D}{dC_L} \qquad (2.6)$$

Rewriting Eq.(2.6) for the drag at the optimum range altitude, $D_m$, with $q_m$ and $C_{L_m}$ also representing the optimum values, we get

$$D_m = W\frac{dC_D}{dC_L}(C_{L_m}) \qquad (2.7)$$

which gives a value of $D_m$ that is proportional to the weight. If we assume that the minimum drag of the elastic wing is also proportional the the weight and that the proportionality constant, $\kappa = dC_D/dC_L$, is constant during the cruise, we can write

$$D_m = \kappa W_h \qquad (2.8)$$

during the entire cruise phase where $W_h$ is the half-fuel condition.

The rate at which the aircraft burns fuel is given by

$$\frac{dW}{dt} = -c'T = -c'D = -c'\kappa W_h \qquad (2.9)$$

where $c'$ is the thrust specific fuel consumption of the engine and $T$ is the thrust. Performing an integration from some initial time $t_i$ to some final time $t_f$, we get

$$\log\left(\frac{W_i}{W_f}\right) = \kappa c'(t_f - t_i) \qquad (2.10)$$

where $W_i$ and $W_f$ are the initial and final weight respectively. Since we will set the cruise at a constant speed $V_c$, the range during cruise, $R_c$, will be given by

$$R_c = V_c(t_f - t_i) = \frac{V_c}{\kappa c'}\log\left(\frac{W_i}{W_f}\right) \qquad (2.11)$$

The calculation of $\kappa$ assumes we know the value of optimum dynamic pressure, $q_m$, which could be calculated from equation 2.6. However, we allow the dynamic pressure to be a design variable, which causes $q$ to optimized with the rest of the aircraft.

# 3. THE AERODYNAMIC AND STRUCTURAL MODELS

## 3.0. Introduction

While the Vortex-Lattice Method (VLM) is an old approach for the solution of aerodynamic forces, it is ideally suited for the subsonic design problem being considered in this research. The accuracy of the method is sufficient for this preliminary design[8], and the results can be obtained quickly, even over complex wing shapes. More sophisticated models certainly exist, but most have considerable computational costs associated with them. Without further research, these methods are far too expensive for design optimization. The VLM model used in this study is the same as that used in previous research[4], however some modifications are made to the calculation of the forces in hopes of making the procedure more robust.

The structural model considered here, is also retained from previous research.[5] The model employs the Finite-Element Method (FEM) to determine the deflections the wing undergoes during loading. The FEM model provides excellent results without the overwhelming computational costs that can be associated with sophisticated aerodynamic analysis.

## 3.1. The Vortex-Lattice Method

In the VLM approach, a thin wing is broken up into a discrete number of swept panels. Each of these panels lies on the mean camber surface of the wing. Attached to the quarter chord of each of these panels is a horseshoe vortex (see Fig. 3.1). If we follow the development of Ref. 9, the ends of the vortex filaments go to infinity, parallel to the x-axis of the wing. This approach is only an approximation, but it will provide sufficient accuracy.[9] The individual circulations all contribute an induced velocity on every panel. The boundary conditions require that the total induced

velocity is tangent to the surface of each individual panel at its control point, which is located at the three-quarter chord of the panel. With the application of these boundary conditions, we end up with a system of 2N equations in terms of the unknown circulation strengths, where N is the number of panels on one wing (both wings have to be accounted for). Previous work set the number of panels at 120, with 10 along each chord and 12 along the half-span. This study found that to be an inadequate number, and the panels were increased to 190, with 10 along the chord and 19 along the half-span.
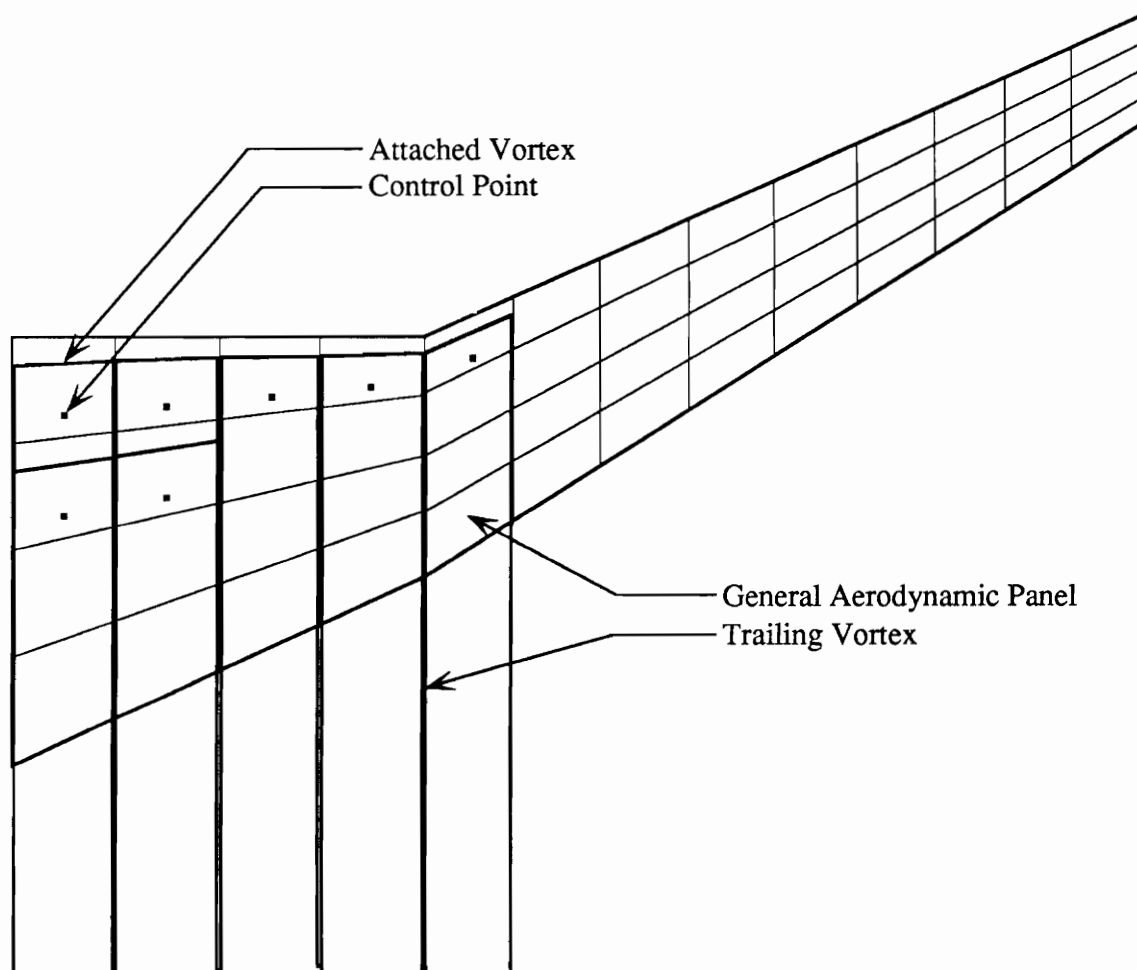


**Figure 3.1.** Wing Panels with Sample Horseshoe Vorticies

The determination of the velocity caused by a vortex filament can be found through the application of the Biot-Savart Law:

$$dV = \frac{\Gamma(d\boldsymbol{l} \times \boldsymbol{r})}{4\pi r^3} \tag{3.1}$$

where $\Gamma$ is the strength of the given vortex and $d\boldsymbol{l}$ is its length. The magnitude of the velocity is easily seen to be:

$$dV = \frac{\Gamma dl \sin\theta}{4\pi r^2} \tag{3.2}$$

where $\theta$ is the angle between $d\boldsymbol{l}$ and $\boldsymbol{r}$. If we again follow the procedure outlined in Ref. 9, the velocity induced by a vortex from Point $A$ to $B$ can be found to be:

$$V_{AB} = \frac{\Gamma}{4\pi r_{cp}} \int_{\theta_1}^{\theta_2} \sin\theta d\theta = \frac{\Gamma}{4\pi r_{cp}}(\cos\theta_1 - \cos\theta_2) \tag{3.3}$$

See Fig. 3.2 for an illustration of the terms involved. If we note the following relationships:

$$r_{cp} = \frac{|\boldsymbol{r}_1 \times \boldsymbol{r}_2|}{r_0}$$

$$\cos\theta_1 = \frac{\boldsymbol{r}_0 \cdot \boldsymbol{r}_1}{r_0 r_1}$$

$$\cos\theta_2 = \frac{\boldsymbol{r}_0 \cdot \boldsymbol{r}_2}{r_0 r_2}$$

and substitute them into Eq.(3.3), we obtain the following:

$$V_{AB} = \frac{\Gamma}{4\pi} \frac{\boldsymbol{r}_1 \times \boldsymbol{r}_2}{|\boldsymbol{r}_1 \times \boldsymbol{r}_2|^2} \left[ \boldsymbol{r}_0 \cdot \left( \frac{\boldsymbol{r}_1}{r_1} - \frac{\boldsymbol{r}_2}{r_2} \right) \right] \tag{3.4}$$

which gives us the general equation for the induced velocity vector.

If a general horseshoe vortex, $i$, is analyzed, the following position vectors are obtained for the vortex segment $AB$ (see Fig. 3.3):

$$\boldsymbol{r}_0 = (x_{2i} - x_{1i})\hat{\boldsymbol{i}} + (y_{2i} - y_{1i})\hat{\boldsymbol{j}} + (z_{2i} - z_{1i})\hat{\boldsymbol{k}}$$

$$\boldsymbol{r}_1 = (x - x_{1i})\hat{\boldsymbol{i}} + (y - y_{1i})\hat{\boldsymbol{j}} + (z - z_{1i})\hat{\boldsymbol{k}}$$

$$\boldsymbol{r}_2 = (x - x_{2i})\hat{\boldsymbol{i}} + (y - y_{2i})\hat{\boldsymbol{j}} + (z - z_{2i})\hat{\boldsymbol{k}}$$

These vectors can be substituted into Eq.(3.4) and an equation can be obtained for $V_{AB}$:[9]

$$V_{AB} = \frac{\Gamma_i}{4\pi}\{F_1\}(F_2) \tag{3.5}$$

where

$$F_1 = \{[(y - y_{1i})(z - z_{2i}) - (y - y_{2i})(z - z_{1i})]\hat{i}$$
$$-[(x - x_{1i})(z - z_{2i}) - (x - x_{2i})(z - z_{1i})]\hat{j}$$
$$+[(x - x_{1i})(y - y_{2i}) - (x - x_{2i})(y - y_{1i})]\hat{k}\}/$$
$$\{[(y - y_{1i})(z - z_{2i}) - (y - y_{2i})(z - z_{1i})]^2$$
$$-[(x - x_{1i})(z - z_{2i}) - (x - x_{2i})(z - z_{1i})]^2$$
$$+[(x - x_{1i})(y - y_{2i}) - (x - x_{2i})(y - y_{1i})]^2\}$$

and

$$F_2 = \frac{[(x_{2i} - x_{1i})(x - x_{1i}) + (y_{2i} - y_{1i})(y - y_{1i}) + (z_{2i} - z_{1i})(z - z_{1i})]}{\sqrt{(x - x_{1i})^2 + (y - y_{1i})^2 + (z - z_{1i})^2}}$$
$$- \frac{[(x_{2i} - x_{1i})(x - x_{2i}) + (y_{2i} - y_{1i})(y - y_{2i}) + (z_{2i} - z_{1i})(z - z_{2i})]}{\sqrt{(x - x_{2i})^2 + (y - y_{2i})^2 + (z - z_{2i})^2}}$$

Next, if the vortex segment $AD$ is considered, the position vectors will be:

$$r_0 = (x_{1i} - x_{3i})\hat{i}$$
$$r_1 = (x - x_{3i})\hat{i} + (y - y_{1i})\hat{j} + (z - z_{1i})\hat{k}$$
$$r_2 = (x - x_{1i})\hat{i} + (y - y_{1i})\hat{j} + (z - z_{1i})\hat{k}$$

If the same calculations are made as for Eq.(3.5) then the following can be obtained as $x_{3i} \rightarrow \infty$:[9]

$$V_{A\infty} = \frac{\Gamma_i}{4\pi}\left\{\frac{(z - z_{1i})\hat{j} + (y_{1i} - y)\hat{k}}{[(z - z_{1i})^2 + (y_{1i} - y)^2]}\right\}\left[1 + \frac{(x - x_{1i})}{\sqrt{(x - x_{1i})^2 + (y - y_{1i})^2 + (z - z_{1i})^2}}\right]$$

$$(3.6)$$

For opposite segment, $B\infty$, we obtain:[9]

$$V_{B\infty} = \frac{\Gamma_i}{4\pi} \left\{ \frac{(z - z_{2i})\hat{j} + (y_{2i} - y)\hat{k}}{[(z - z_{2i})^2 + (y_{2i} - y)^2]} \right\} \left[ 1 + \frac{(x - x_{2i})}{\sqrt{(x - x_{2i})^2 + (y - y_{2i})^2 + (z - z_{2i})^2}} \right]$$

(3.7)

To obtain the total induced velocity for the given horseshoe vortex, Eqs.(3.5, 3.6, and 3.7) are summed together.

If all the horseshoe vorticies over both wing surfaces are summed together, then the total induced velocity at some control point $j$, would be represented as:

$$V_{j_{ind}} = \sum_{i=1}^{2N} C_{ij}\Gamma_i$$

(3.8)

where $C_{ij}$ is an geometrical influence coefficient relating the induced velocity at control point $j$ due to the bound horseshoe vortex $i$. A system of 2N equations can now be formulated with the application of the boundary conditions.
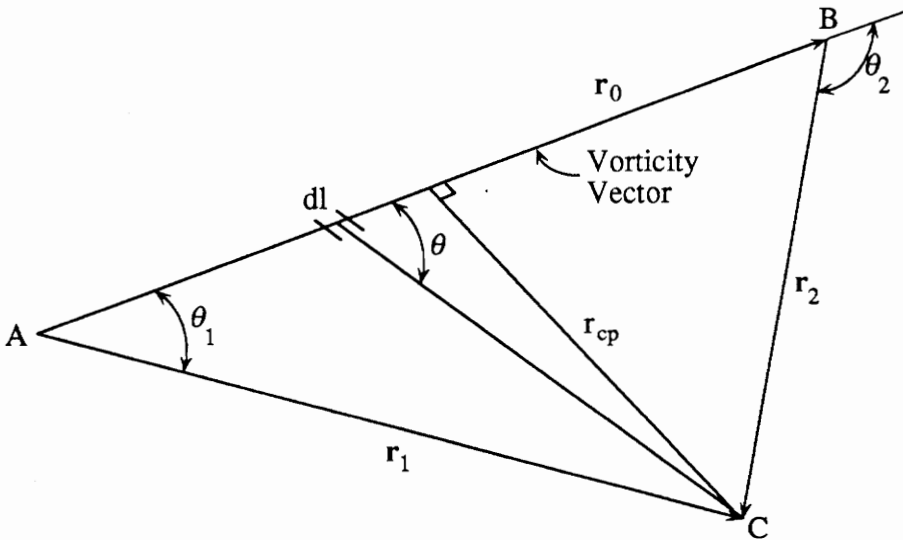


**Figure 3.2.** Nomenclature for Induced Velocity by a Finite Length Vortex [9]
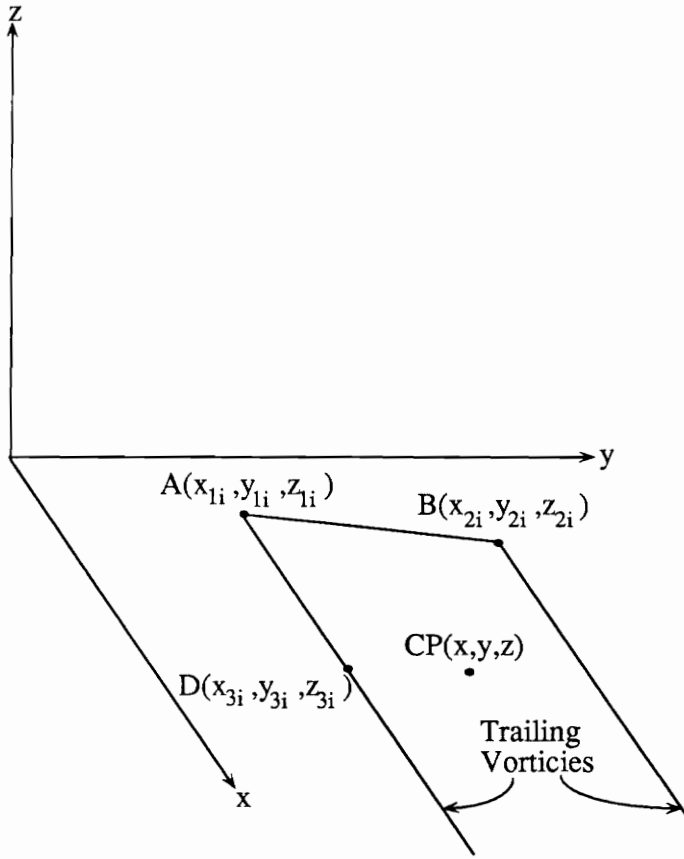
**Figure 3.3.** Sample Horseshoe Vortex

The boundary condition requires the total velocity to be tangent to the surface of the wing at all of the control points.

$$V_{j_{ind}} \cdot \hat{n}_j = 0 \tag{3.9}$$

The total velocity is represented by the sum of the freestream velocity,

$$U_\infty = U_\infty \cos \alpha \hat{\imath} + 0\hat{\jmath} + U_\infty \sin \alpha \hat{k} \tag{3.10}$$

and the induced velocity vector at control point $j$.

$$V_{j_{ind}} = u_j \hat{\imath} + v_j \hat{\jmath} + w_j \hat{k} \tag{3.11}$$

Employing Eq.(3.9) we get the boundary condition to be:

$$U_\infty \sin \alpha - U_\infty \cos \alpha \left(\frac{\partial F}{\partial x}\right)_j - u_j \left(\frac{\partial F}{\partial x}\right)_j - v_j \left(\frac{\partial F}{\partial y}\right)_j + w_j = 0 \qquad (3.12)$$

where $F(x, y)$ represents the mean camber surface. If we let $\delta$ be the angle the surface forms in the $x - z$ plane, and $\phi$ be the angle in the $y - z$ plane, then with some rearrangement we can write:

$$-u_j \sin \delta_j \cos \phi_j - v_j \cos \delta_j \sin \phi_j + w_j \cos \phi_j \cos \delta_j + U_\infty \sin (\alpha - \delta_j) \cos \phi_j = 0$$

$$(3.13)$$

Finally, Eqs.(3.8 and 3.13) can be combined and a system of equations is generated of the form:

$$\mathbf{C\Gamma} = \mathbf{R} \qquad (3.14)$$

which can be solved for the unknown $\boldsymbol{\Gamma}$.

## 3.2. Lift and Drag Calculations

Once the circulation over each panel is known, it is possible to determine the lift and induced drag acting on the wing. If we follow the calculations performed in Ref. 4, then the Kutta-Joukowski theorem shows that the force per unit length on panel $j$ is given by:

$$\boldsymbol{F}_j = \rho \boldsymbol{V}_j \times \boldsymbol{\Gamma}_j \qquad (3.15)$$

where $\boldsymbol{V}_j$ is the total velocity on panel $j$. The lift and drag can then be extracted to yield:[4]

$$L_j = (F_{z_j} \cos \alpha - F_{x_j} \sin \alpha) \Delta y_j$$

$$(3.16)$$

$$D_{ind_j} = (F_{z_j} \sin \alpha - F_{x_j} \cos \alpha) \Delta y_j$$

This approach is recommended in Ref. 10. However, in the current study, it was determined that this approach tended to give values for drag which gave span efficiencies, $e$, greater than one. This indicated that the computed values for drag were low. These drag calculations were also highly dependent on the paneling scheme selected. It was later learned that this method is rarely used for drag determination in industry computer codes.[11] Furthermore, results given in Ref. 12, indicate that a near-field drag calculation is in fact sensitive to the paneling scheme and the geometrical layout. Since this approach does calculate the drag using near-field information, it is subjected to panel sensitivity. This sensitivity is highly undesirable because as the design changes, the shape of the wing is changed. The new shape would require a different paneling scheme for optimal accuracy, and that is difficult to automate. A new approach needs to be used which is insensitive to the paneling scheme (providing the initial scheme has enough panels)

A common alternative is found by calculating the induced drag in the far-field using the Trefftz plane.[11] In this approach, we note that in the far field the flow does not vary in the streamwise coordinate and is therefore 2-D. Furthermore, we know that in a plane perpendicular to the streamwise coordinate (the Trefftz plane) the 2-D flow is induced entirely by the trailing vortex sheet where the circulation along this sheet can be represented with the following Fourier sine series:[13]

$$\Gamma(\theta) = 2bU_\infty \sum_{n=1}^{\infty} A_n \sin n\theta \qquad (3.17)$$

where $\theta$ is defined by

$$\cos\theta = 2y/b$$

Since the circulation distribution has already been calculated, the coefficients of the series can be determined. In terms of this series representation, the downwash, $w$, is:[13]

$$w = U_\infty \sum_{n=1}^{\infty} nA_n \frac{\sin n\theta}{\sin \theta} \qquad (3.18)$$

The induced drag is given by[13]

$$\delta D_{ind}(\theta) = -\rho_\infty \frac{b}{2} w(\theta) \Gamma(\theta) \sin\theta d\theta$$

thus

$$\delta D_{ind}(\theta) = -\rho_\infty U_\infty^2 b^2 \sum_{n=1}^{\infty} n A_n^2 \sin^2 n\theta d\theta \tag{3.19}$$

which is then integrated and nondimensionalized to yield the induced drag coefficient, $C_{D_i}$, as:[13]

$$C_{D_i} = \frac{C_L^2}{\pi AR} \left[ 1 + \sum_{n=2}^{\infty} n \left( \frac{A_n}{A_1} \right)^2 \right] \tag{3.20}$$

where $AR$ is the aspect ratio. The lift coefficient, $C_L$, is defined by:

$$C_L = \frac{L}{qS} \tag{3.21}$$

where $q$ is the dynamic pressure and $S$ is the wing area. The total lift, $L$, is given by integrating the lift per unit span,

$$L = 2 \int_0^{b/2} l dy \tag{3.22a}$$

Or, in terms of the individual spanwise sections, $j$:

$$L = 2 \sum_{j=1}^{m} l_j \Delta y_j \tag{3.22b}$$

where m is the number of spanwise panels. The lift per unit span can be obtained with:

$$l_j = \rho U_\infty \Gamma_j \tag{3.23}$$

Equation (3.20) can be written in terms of the span efficiency, $e$, as:

$$C_D = \frac{C_L^2}{\pi AR e} \tag{3.24}$$

where

$$e = \left[1 + \sum_{n=2}^{\infty} n \left(\frac{A_n}{A_1}\right)^2\right]^{-1}$$

The actual determination of the induced drag coefficient was done using the LIDRAG[14] fortran code present in TRO3D.[24] This routine determines the coefficients of the Fourier series and returns the span efficiency, $e$, for a given lift distribution. The code uses the principles given above with a 32 term series approximation. It should be noted that small errors will be incurred due to the dihedral caused by deflection because the LIDRAG routine does not account for this. However, Ref. 15 gives some information which indicates that the error in $e$ is negligible for small dihedral angles. Since the dihedral angles due to deflection encountered during this study were in fact small, this error will be neglected.

The viscous drag on the wing is obtained by first determining the local section drag in the streamwise direction, $C_{d_v}$, from the airfoil drag polar.[16] The total viscous drag, $C_{D_v}$, can then be determined with the following integral:

$$C_{D_v} = \frac{2}{S} \int_0^{b/2} C_{d_v} c \, dy \tag{3.25a}$$

Or, in terms of the individual sections:

$$C_{D_v} = \frac{2}{S} \sum_{j=1}^{m} C_{d_{v_j}} c_j \Delta y_j \tag{3.25b}$$

where c is the local chord.

The remaining drag is associated with the fuselage and tail, $C_{D_{ft}}$. Since the aerodynamic shape of these surfaces is not being designed in this study, their contribution is assumed constant. This constant was determined in previous research by looking at a reference aircraft (see table 2.1), and subtracting the total wing drag coefficient from the aircraft's total drag coefficient,[4]

$$C_{D_{ft}} = C_{D_{a/c_0}} - C_{D_{w_0}} \tag{3.26}$$

where $C_{D_{a/c_0}}$ is the drag coefficient of the reference aircraft at zero angle of attack, and $C_{D_{w_0}}$ is the drag coefficient of the design wing at the same angle of attack. While this above approximation is very crude, a detailed analysis of the fuselage and tail is beyond the scope of this study.

## 3.3. Compressibility Correction

Through the use of a Göthert transformation, the necessary compressiblity corrections can be applied to the aerodynamic analysis. The process is detailed in Ref. 17 and begins with the statement of the linearized potential equation,

$$\beta^2 \frac{\partial^2 \phi}{\partial x^2} + \frac{\partial^2 \phi}{\partial y^2} + \frac{\partial^2 \phi}{\partial z^2} = 0 \tag{3.27}$$

where $\beta \equiv \sqrt{1 - M_\infty^2}$, and $\phi$ is the perturbation potential. Under this linearization, the flow velocities are defined as follows:

$$V = (U_\infty \cos \alpha + u)\hat{i} + v\hat{j} + (U_\infty \sin \alpha + w)\hat{k} \tag{3.28}$$

where the perturbation velocities $u, v$, and $w$ are:

$$u = \frac{\partial \phi}{\partial x}; \quad v = \frac{\partial \phi}{\partial y}; \quad w = \frac{\partial \phi}{\partial z}$$

Returning to the boundary conditions given in Eq.(3.12), we have:

$$(U_\infty \cos \alpha + u)\frac{\partial f}{\partial x} + v\frac{\partial f}{\partial y} + (U_\infty \sin \alpha + w)\frac{\partial f}{\partial z} = 0 \tag{3.29}$$

where $f(x, y, z)$ gives the parametric equation for the surface.

Since the VLM model given in section 3.1 is based on an incompressible flow, it is necessary to perform a transformation on Eq.(3.27) which gives it the same

form as the incompressible potential equation ($\beta \equiv 1$). This can be accomplished with the use of an affine transformation as follows:[17]

$$x' \equiv x; \quad y' \equiv \beta y; \quad z' \equiv \beta z; \quad \phi' \equiv \beta^2 \phi$$

If these expressions are substituted into Eq.(3.27), we indeed get the incompressible form.

$$\frac{\partial^2 \phi'}{\partial x'^2} + \frac{\partial^2 \phi'}{\partial y'^2} + \frac{\partial^2 \phi'}{\partial z'^2} = 0 \tag{3.30}$$

In these transformed coordinates, the boundary conditions would be:

$$(U_\infty \cos \alpha' + u') \frac{\partial f'}{\partial x'} + v' \frac{\partial f'}{\partial y'} + (U_\infty \sin \alpha' + w') \frac{\partial f'}{\partial z'} = 0 \tag{3.31}$$

Now it is possible to use VLM method as before, but first the coordinates of the wing surface must undergo the affine transformation. Once the forces on the transformed wing are obtained, it is necessary to find the compressible values for these forces (or coefficients). Since the incompressible pressure coefficient is given as:

$$C_p' = -2U_\infty u' \tag{3.32}$$

and $u'$ can be found to be $\beta^2 u$, then clearly:

$$C_p = \frac{1}{\beta^2} C_p' \tag{3.33}$$

The lift and induced drag coefficients are determined from integration of the pressure coefficient, therefore:

$$\begin{aligned} C_L &= \frac{1}{\beta^2} C_L' \\ C_{D_i} &= \frac{1}{\beta^2} C_{D_i}' \end{aligned} \tag{3.34}$$

## 3.4. The Structural Model

The structural analysis employs a modification of the WIDOWAC[18] program and the details of this analysis can be found in Ref. 5. In short, the analysis uses the FEM with 1093 elements and 534 degrees of freedom. The wing is composed of 684 anisotropic membrane elements for the graphite-epoxy wing skin, and 138 shear webs for the wing spars. Truss elements are utilized to model the spar caps and the vertical stiffness of the ribs.[4] A simplified representation of the wing structure can be seen in Fig. 2.2.

# 4. THE AEROELASTIC FORMULATION

## 4.0. Introduction

The backbone of the multi-disciplinary design is the aeroelastic formulation which accounts for the interaction between the structural deformation and the aerodynamic response. This interaction is complex and a set of simplifying assumptions must be made. We will make the same assumptions as in Ref. 6. First, it is assumed that all the aerodynamic response can be represented by a vector of forces, $F_a$, acting at a predetermined set of structural points known as the load set.* Furthermore, it is also assumed that the full deformation of the structure can also be represented at this load set with a vector of deflections, $\theta$. Finally, we assume that wing is affected by the aircraft only through the root angle of attack, $\alpha$. With these simplifying assumptions, it is now possible to develop the wing's full response to any given flight condition (provided the individual models are still valid) as in Ref. 6.

## 4.1. The Functional Dependencies

In chapter 3 we saw that we could determine the forces acting on the wing if we knew the strength of the circulation acting on each panel. Additionally, we know that this force is also dependent on the angle of attack, the dynamic pressure, and the geometry and deflection of the wing. Since the wing's geometry and the dynamic pressure are represented by the design vector, $p$, and the deflection is given by $\theta$, we can write

$$F_a = F_a(p, \alpha, \theta, \Gamma) \tag{4.1}$$

---

\* Chapter 5 details the complete process of representing all the aerodynamic forces at the load set.

We also recall from chapter 3, that $\boldsymbol{\Gamma}$ can be determined from

$$\mathbf{C}\boldsymbol{\Gamma} = \boldsymbol{R} \qquad (3.14)$$

where the matrix $\mathbf{C}$ is dependent on $\boldsymbol{p}$ and $\boldsymbol{\theta}$, and the vector $\boldsymbol{R}$ is dependent on $\boldsymbol{p}$, $\boldsymbol{\theta}$, and $\alpha$. With this information, we can conclude that

$$\boldsymbol{\Gamma} = \boldsymbol{\Gamma}(\boldsymbol{p}, \alpha, \boldsymbol{\theta}) \qquad (4.2)$$

By combining Eqs.(4.1 and 4.2), the following functional dependence will be obtained.[6]

$$\boldsymbol{F_a} = \boldsymbol{f_1}(\boldsymbol{p}, \alpha, \boldsymbol{\theta}) \qquad (4.3)$$

The performance requirement that requires the aircraft to remain balanced at all times yields another functional equation[6]

$$f_2(\boldsymbol{p}, \boldsymbol{F_a}) = \tfrac{1}{2}nW(\boldsymbol{p}) - \mathbf{N}^T \boldsymbol{F_a} = 0 \qquad (4.4)$$

where $n$ is the load factor, $W$ is the weight, and $\mathbf{N}^T$ is the summation vector. From this equation it is possible to determine the angle of attack.

From Refs. 5 and 6 we see that we can write the complete set of nodal deflections, $\boldsymbol{U}$ (determined from finite element analysis), by solving

$$\mathbf{K}(\boldsymbol{p})\boldsymbol{U} = \mathbf{T}\boldsymbol{F_a} + n\boldsymbol{F_I}(\boldsymbol{p}) \qquad (4.5)$$

where $\mathbf{K}$ is the stiffness matrix, $\mathbf{T}$ is a Boolean matrix to expand $\boldsymbol{F_a}$ to the full degree of freedom (DOF) model (see Ref. 5), and $\boldsymbol{F_I}$ is the gravitational and inertial force vector. To obtain $\boldsymbol{\theta}$ we simply multiply it by the transpose of the Boolean matrix.

$$\boldsymbol{\theta} = \mathbf{T}^T \boldsymbol{U} \qquad (4.6)$$

And finally, the combination of Eqs.(4.5 and 4.6) yields

$$\boldsymbol{\theta} = \boldsymbol{f_3}(\boldsymbol{p}, \boldsymbol{F_a}) \qquad (4.7)$$

## 4.2. The Solution Process

The three equations given in last section (4.3, 4.4, and 4.7) represent a system of coupled non-linear equations for which $\theta$, $\alpha$, and $F_a$ are the unknowns. The solution procedure is given in Ref. 6 and will be detailed here. First we assume that each of the functions, $f_1$, $f_2$, and $f_3$, behave as 'black boxes' to which no modifications will be made during the solution process.[6] The function $f_1$ represents the aerodynamic processes and the function $f_3$ gives us the structural processes. These equations can be solved through the use of the Newton's method.

The first step involved in the solution process is setting up the system in homogeneous form.

$$F_a - f_1(p, \alpha, \theta) = 0 \tag{4.8a}$$

$$-f_2(p, F_a) = N^T F_a - \tfrac{1}{2} nW(p) = 0 \tag{4.8b}$$

$$\theta - f_3(p, F_a) = 0 \tag{4.8c}$$

The iterative step is then written as

$$J \Delta X = \Delta f \tag{4.9}$$

where

$$\Delta X = \left\{ \begin{array}{c} \Delta F_a \\ \Delta \alpha \\ \Delta \theta \end{array} \right\} \tag{4.10}$$

and

$$\Delta f = \left\{ \begin{array}{c} f_1(p, \alpha^0, \theta^0) - F_a^0 \\ f_2(p, F_a^0) \\ f_3(p, F_a^0) - \theta^0 \end{array} \right\} \tag{4.11}$$

where the Jacobian, $J$, is given by

$$J = \begin{bmatrix} I & -\partial f_1/\partial \alpha & -\partial f_1/\partial \theta \\ -\partial f_2/\partial F_a & 0 & 0 \\ -\partial f_3/\partial F_a & 0 & I \end{bmatrix} \tag{4.12a}$$

or

$$J = \begin{bmatrix} \mathbf{I} & -qR & -q\mathbf{A} \\ \mathbf{N}^T & 0 & 0 \\ -\mathbf{S} & 0 & \mathbf{I} \end{bmatrix} \qquad (4.12b)$$

This gives us the Jacobian in terms of the incremental aerodynamic force vector, $qR$, the aerodynamic influence matrix, $q\mathbf{A}$, and the structural flexibility matrix $\mathbf{S}$.[6] The incremental force vector element $qr_i$ describes the change in force at node $i$ due to a unit change in angle of attack, and the flexibility matrix element $s_{ij}$ describes the change in deflection at node $i$ due to a unit change of force at node $j$. The aerodynamic influence matrix will be discussed in detail in chapter 5.

With the above information, it is now possible to partially solve the above matrix equation for the unknowns $\Delta F_a$, $\Delta\alpha$, and $\Delta\theta$ as follows:

$$(\mathbf{I} - q\mathbf{S}\mathbf{A}^x)\Delta\theta = \mathbf{S}\mathbf{B}\Delta f_1 + \frac{\mathbf{S}R}{\mathbf{N}^T R}\Delta f_2 + \Delta f_3 \qquad (4.13)$$

$$\Delta\alpha = \frac{\Delta f_2 - \mathbf{N}^T\Delta f_1 - q\mathbf{N}^T\mathbf{A}\Delta\theta}{q\mathbf{N}^T R} \qquad (4.14)$$

$$\Delta F_a = \Delta f_1 + qR\Delta\alpha + q\mathbf{A}\Delta\theta \qquad (4.15)$$

where

$$\mathbf{B} \equiv \mathbf{I} - \frac{R\mathbf{N}^T}{\mathbf{N}^T R} \qquad (4.16)$$

and

$$\mathbf{A}^x \equiv \mathbf{B}\mathbf{A} \qquad (4.17)$$

To begin the iteration we select the initial conditions to be the rigid wing approximation,

$$F_a^0 = F_{ar}; \quad \alpha^0 = \alpha_r; \quad \theta^0 = 0 \qquad (4.18)$$

where

$$F_{ar} = f_1(p, 0, 0) + q\alpha_r R \tag{4.19}$$

$$\alpha_r = \frac{\frac{1}{2}nW - N^T f_1(p, 0, 0)}{qN^T R} \tag{4.20}$$

Now the vector of unknowns can be approximated by a single Newton iteration with Eqs.(4.13 – 4.15).

Also critical to the aeroelastic considerations is the calculation of the divergence dynamic pressure, $q_D$. We proceed as in Ref. 6 and assume that the calculation can be made at a fixed angle of attack because we assume that the wing diverges much faster than the pilot can change the angle of attack. Then it is possible to represent the system (Eq. 4.9) as

$$\begin{bmatrix} I & -qA \\ -S & I \end{bmatrix} \left\{ \begin{array}{c} \Delta F_a \\ \Delta \theta \end{array} \right\} = 0 \tag{4.21}$$

where we have an eigenvalue problem for $q$ which represents the divergence dynamic pressure (the lowest eigenvalue is $q_D$). The corresponding eigenvector is represented as $[F_{aD}, \theta_D]^T$. If we wish to reduce the problem to a standard linear eigenvalue problem, $\Delta \theta$ can be represented in terms of $\Delta F_a$ which yields:[6]

$$(AS - \frac{1}{q}I)\Delta F_a = 0 \tag{4.22}$$

# 5. THE AERODYNAMIC–STRUCTURAL INTERFACE

## 5.0. Introduction

In any multi-disciplinary analysis, separate models describe each physical process. For the work involved here, the models represent static structural and aerodynamic responses of a wing. Each of these models has specific control points (i.e. points where displacements and/or forces are applied and calculated). For the structural model, we generally have control points at each of the finite element nodes, and the aerodynamic control points would be the vortex lattice control points.

As mentioned in section 4.0, the design problem necessitates the selection of load set points. The aerodynamic and structural nodes are possible candidates for these points. Unfortunately, use of either of these sets would result in an enormous problem with large demands on storage and computational time because many of the aeroelastic and sensitivity terms have dimensions which are defined by the number of load set nodes. Furthermore, many of the calculations necessary in the aeroelastic formulation and sensitivity calculations have a run time which is dependent on the dimensions of these terms (i.e. the $\mathbf{A}$ matrix). An alternate choice is found by selecting a small subset of the structural control points. For this study, the set contains only 48.* All forces applied to the structure are applied only at these points (designated by the vector $F_a$), and all deflections are given only at these points (designated by the vector $\theta$). Figure 5.1 shows a sample set of aerodynamic and load set points. In general, the load set and aerodynamic control points will be different. Therefore, there is a need to interface the load set nodes and the aerodynamic control points, so that information can be passed between the two systems. For

---

* The relationships between this subset and the full DOF finite element model can be found in Ref. 5.

this specific problem, the interface involves the transference of displacements at the load set to the aerodynamic control points, and the transference of forces on the aerodynamic control points to the load set. This study looks at two different approaches to the interface model.



● – Aerodynamic Control Points
○ – Load Set Nodes
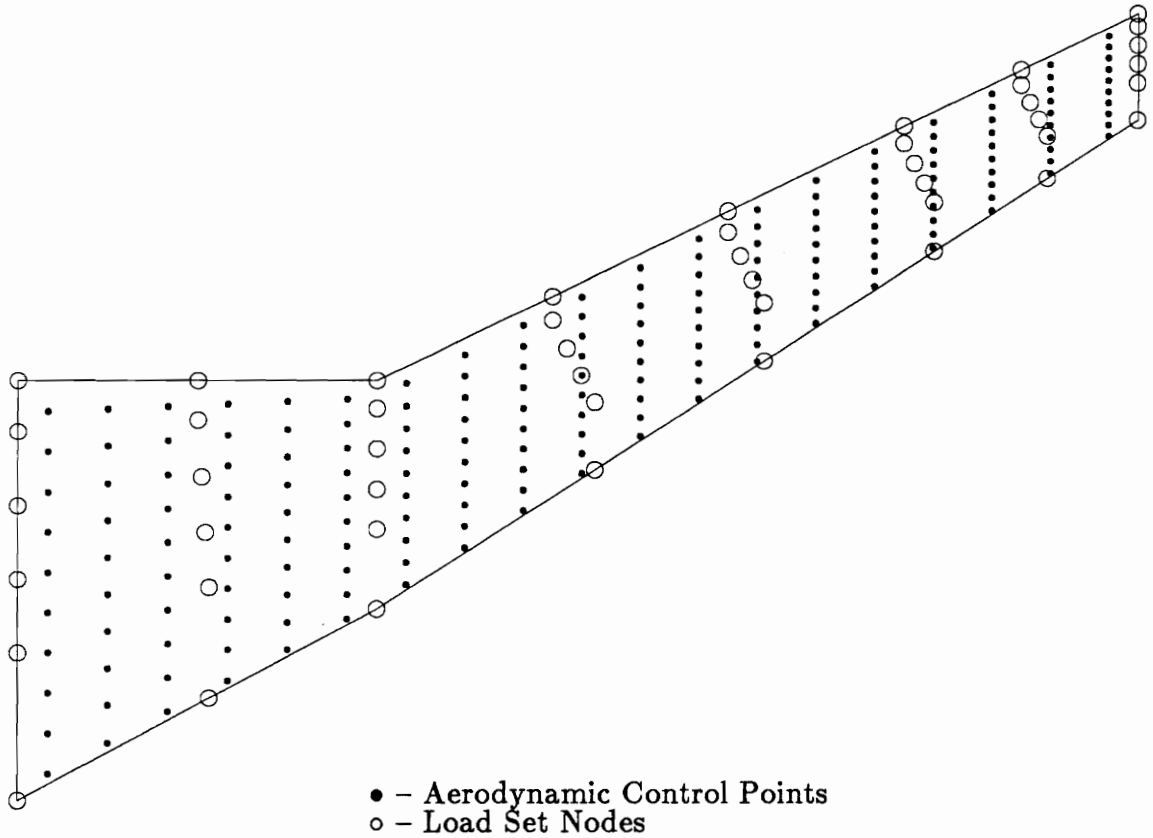
**Figure 5.1.** Aerodynamic Points and Load Set Nodes

## 5.1. Previous Work

The first model is a discrete zonal scheme developed in previous research by D. Polen.[4] The basis for Polen's approach lies in a force and moment balance which conserves the force and moment totals of the entire force vector. For example, if a force is known at a particular aerodynamic point $F_{z_j}$, and that point is surrounded

by three load set points, then the forces at the load set points $F_{a_i}$ can be calculated from

$$\sum_{i=1}^{3} F_{a_i} = F_{z_j} \qquad (5.1)$$

$$\sum_{i=1}^{3} F_{a_i}(x_{a_i} - x_0) = F_{z_j}(x_{z_j} - x_0) \qquad (5.2)$$

$$\sum_{i=1}^{3} F_{a_i}(y_{a_i} - y_0) = F_{z_j}(y_{z_j} - y_0) \qquad (5.3)$$

This balancing process is repeated for each aerodynamic node, and the resulting contributions to each structural node is stored in a matrix format such that

$$F_a = D_0 F_z \qquad (5.4)$$

where $F_a$ and $F_z$ are the vectors of forces at the load set and aerodynamic points respectively, and $D_0$ is the transformation matrix. The deflections at each of the aerodynamic points $(Z_z)$ can be determined by requiring the work done by the aerodynamic forces and the load set forces to be the same. We get

$$F_a^T \theta = F_z^T Z_z$$

$$(D_0 F_z)^T \theta = F_z^T Z_z$$

$$F_z^T D_0^T \theta = F_z^T Z_z$$

so that

$$Z_z = D_0^T \theta \qquad (5.5)$$

This gives us a result in terms of our previously determined transformation matrix.

Essential to the Vortex Lattice Method is the correct calculation of the slope at the surface of the wing. The zonal scheme makes slope calculations trivial since each aerodynamic point lies in a 'zone' formed by three structural points. The

normal to plane which passes through those points will give the slope (see Fig. 5.2). From this figure, it is easy to see the linear interpolation of the approach.
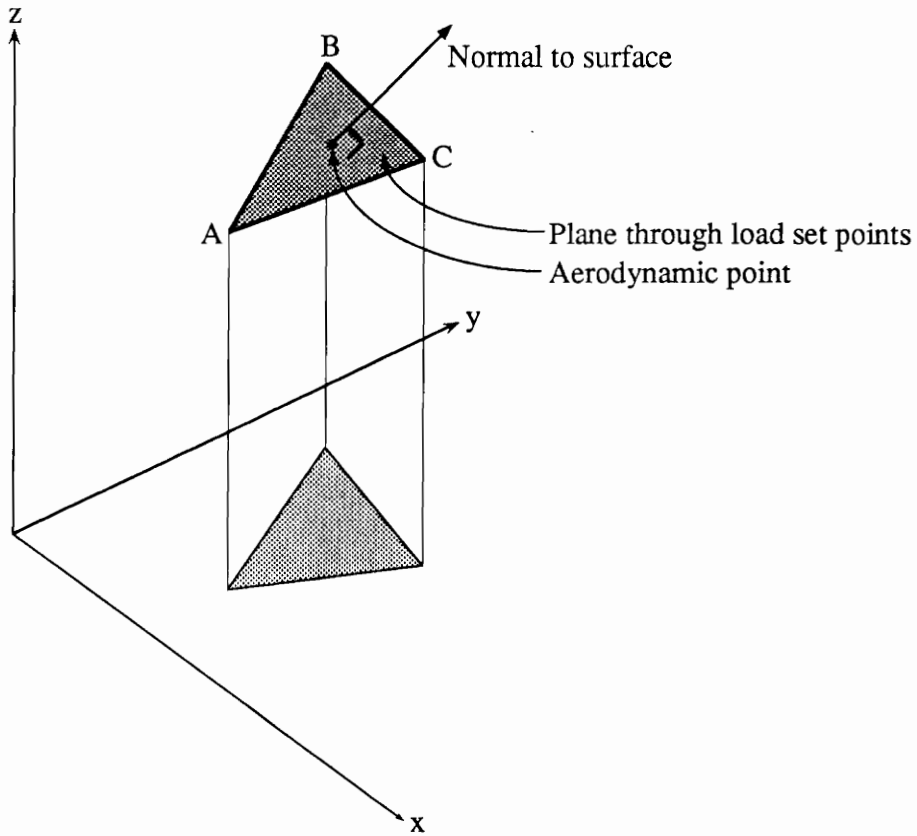


**Figure 5.2.** Plane Through Three Load Set Nodes

This approach is very straightforward and conceptually sound. Table 5.1 gives a sample of the resulting force and moment totals for the transference of forces at the aerodynamic points to the load set. The almost exact agreement given is due to the limited number of necessary calculations. Unfortunately, this method has drawbacks. The first of which is the difficulty in finding the most optimal 'zone' for each aerodynamic point. Clearly, there is almost an infinite number of combinations

for each point and some criteria must be determined for proper selection. Reference 4 addresses this problem, but the end result is a model with extensive logic and significant computational costs. Another problem is not so obvious but is more critical. As the wing changes shape (which can happen if a design parameter is changed), an aerodynamic point can change its 'zone'. This switch in zones can lead to discontinuities in drag as a design parameter is changed. Figure 5.3 illustrates this as the tip span is increased. If a change should happen while a design parameter is perturbed, tremendous errors in sensitivities would incur. Lastly, the interpolation the method performs is linear. Since a linear approach may not give us the best accuracy, we have another reason to look at an additional model and compare the two.

**Table 5.1.** Force and Moment Totals for Old Approach

|  | Lift | X-Moment | Y-Moment |
|---|---|---|---|
| Exact | $7.9659 \times 10^3$N | $4.9710 \times 10^4$N·m | $-1.6975 \times 10^4$N·m |
| Transferred | $7.9659 \times 10^3$N | $4.9710 \times 10^4$N·m | $-1.6975 \times 10^4$N·m |
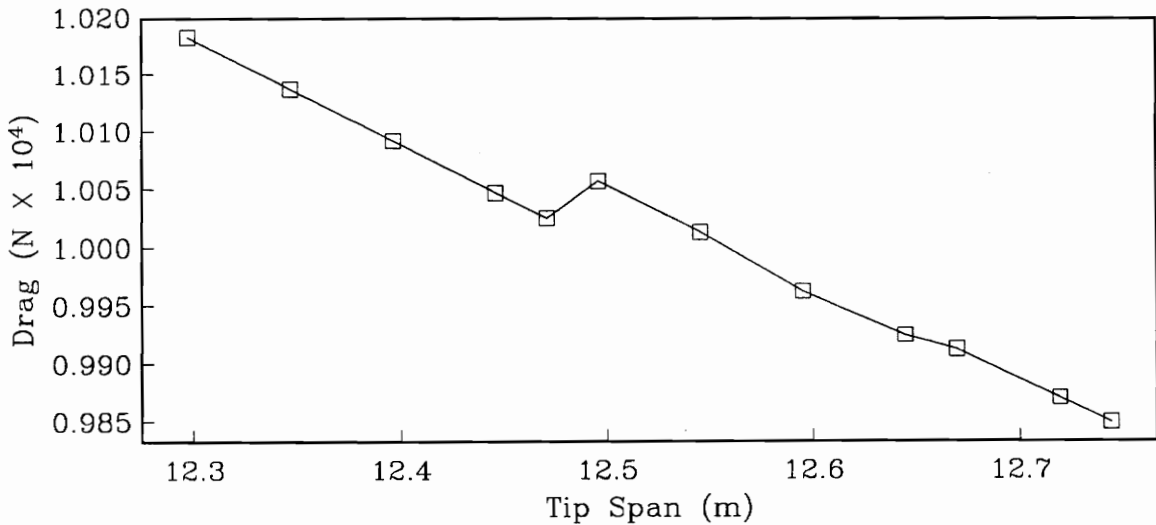


**Figure 5.3.** Drag vs. Tip Span for Previous Model

## 5.2. Shape Function Method

An alternate approach can be found if the problem is viewed in the opposite direction. If we first examine deflections instead of forces, shape functions can be employed to represent the deformation in functional form. With this formulation, shape functions interpolate the deflection of the load set points to the aerodynamic points. This approach is by no means new; Ref. 19 lists a few of the multitudes of schemes that have been proposed, most using plate theory. Reference 19 also presents its own approach which doesn't require any particular grid structure for the aerodynamic or structural points. Since our load set points do in fact have a particular grid structure (see Fig. 5.4a), we can take advantage of that and transform this grid into rectangular cells (see Fig. 5.4b). Next, we can employ the following cubic interpolation functions on the serendipity cells:[20]

$$\Psi_1 = \tfrac{1}{32}(1 - \xi)(1 - \eta)[-10 + 9(\xi^2 + \eta^2)] \tag{5.6a}$$

$$\Psi_2 = \tfrac{1}{32}(1 + \xi)(1 - \eta)[-10 + 9(\xi^2 + \eta^2)] \tag{5.6b}$$

$$\Psi_3 = \tfrac{1}{32}(1 + \xi)(1 + \eta)[-10 + 9(\xi^2 + \eta^2)] \tag{5.6c}$$

$$\Psi_4 = \tfrac{1}{32}(1 - \xi)(1 + \eta)[-10 + 9(\xi^2 + \eta^2)] \tag{5.6d}$$

$$\Psi_5 = \tfrac{9}{32}(1 - \eta)(1 - \xi^2)(1 - 3\xi) \tag{5.6e}$$

$$\Psi_6 = \tfrac{9}{32}(1 - \eta)(1 + \xi^2)(1 - 3\xi) \tag{5.6f}$$

$$\Psi_7 = \tfrac{9}{32}(1 + \xi)(1 - \eta^2)(1 - 3\eta) \tag{5.6g}$$

$$\Psi_8 = \tfrac{9}{32}(1 + \xi)(1 - \eta^2)(1 + 3\eta) \tag{5.6h}$$

$$\Psi_9 = \tfrac{9}{32}(1 + \eta)(1 - \xi^2)(1 + 3\xi) \tag{5.6i}$$

$$\Psi_{10} = \tfrac{9}{32}(1 + \eta)(1 - \xi^2)(1 - 3\xi) \tag{5.6j}$$

$$\Psi_{11} = \tfrac{9}{32}(1 - \xi)(1 - \eta^2)(1 + 3\eta) \tag{5.6k}$$

$$\Psi_{12} = \tfrac{9}{32}(1 - \xi)(1 - \eta^2)(1 - 3\eta) \tag{5.6l}$$

The normalized coordinates, $\xi$ and $\eta$, are defined in Fig. 5.4c which shows a rectangular element with the necessary nodes. Since we only have data for the four corner nodes, we must interpolate values to the other 8 side nodes. This can be accomplished by using a linear or cubic spline along each grid line. The use of a linear spline results in linear surface splines, and a cubic spline gives cubic surface splines, which in effect gives us two separate models to consider. It should be noted that the use of a linear spline with cubic shape functions is an inefficient approach to a linear surface spline. In this case, the best method would employ linear isoparametric functions given by:[20]

$$\Psi_1 = \tfrac{1}{4}(1 - \xi)(1 - \eta) \tag{5.7a}$$

$$\Psi_2 = \tfrac{1}{4}(1 + \xi)(1 - \eta) \tag{5.7b}$$

$$\Psi_3 = \tfrac{1}{4}(1 - \xi)(1 + \eta) \tag{5.7c}$$

$$\Psi_4 = \tfrac{1}{4}(1 + \xi)(1 + \eta) \tag{5.7d}$$

Clearly, only the four corner nodes are necessary and no iterpolation along grid lines is needed.

While each approach will result in a linear surface spline, the cubic functions will have a slight penalty in CPU time. The advantage in using the cubic functions for both the linear and cubic surface splines lies in the fact that the same code can be used for the two different cases, which simplifies the comparison process. However, once the best model is selected the most efficient technique should be used.

A possible problem with the cubic surface spline lies in the boundaries of the grid. It is necessary to select the value of the second derivative at these boundaries, and a poor selection may adversely effect the results. A linear boundary will be used for this study because of the limited number of grid points along any given grid line (This would result in a linear spline only near the boundaries of the surface).
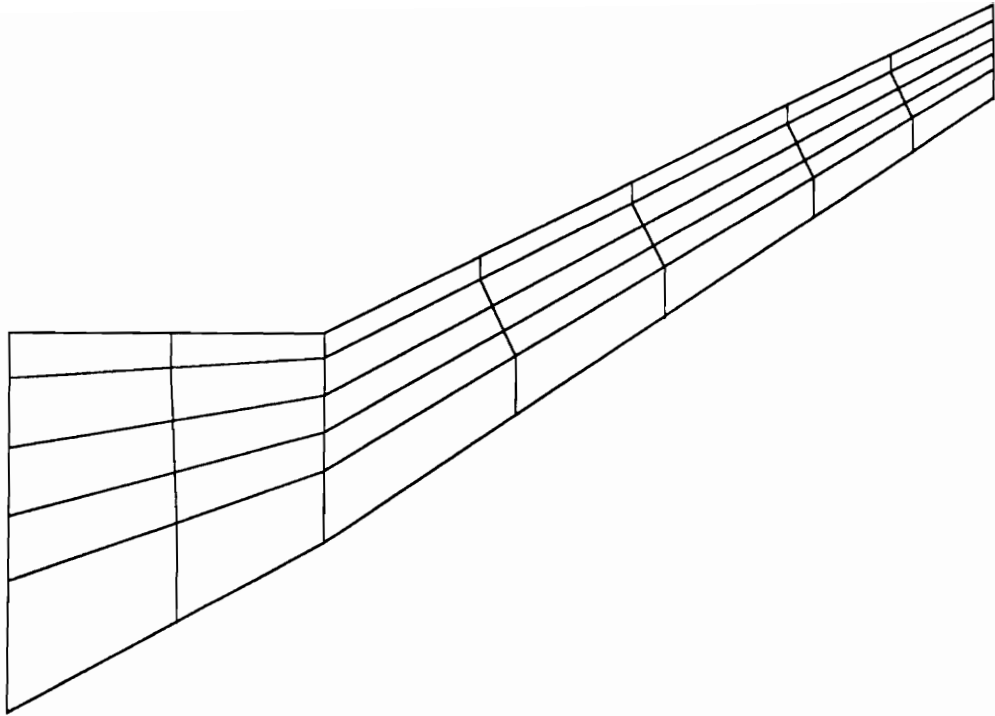
(A) Grid Structure of Load Set Nodes
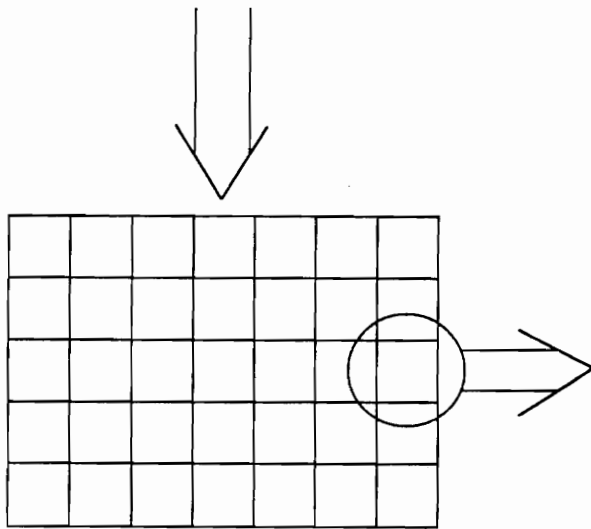
(B) Transformed Grid
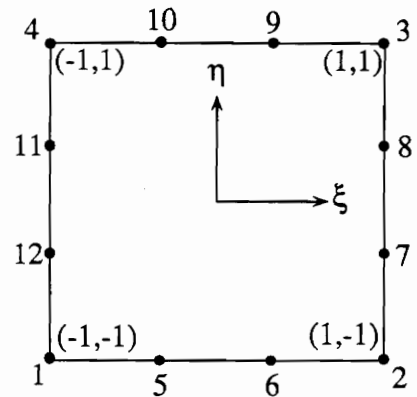
(C) Serendipity Element with Nodes

**Figure 5.4.** Sample of Node Grid Structure and Serendipity Element

As before, it is convenient to put the interpolation in a matrix format. This result can be obtained by making a unit perturbation at a single load set point and calculating the resulting displacement at each of the aerodynamic points. The amount of displacement at each aerodynamic point is determined by first locating the cell in which the point lies, and then using the following summation[20]

$$Z_p = \sum_{i=1}^{12} z_i \Psi_i \tag{5.8}$$

Once the unit perturbation is cycled through each load set point, a transformation matrix can be obtained and we have the vector of displacements at each aerodynamic point,

$$Z_z = \mathbf{D}\theta \tag{5.9}$$

where $\mathbf{D}$ is now the transformation matrix. The forces applied to the load set points can be found with

$$F_a = \mathbf{D}^T F_z \tag{5.10}$$

where this equation is derived as before for Eq.(5.5).

The calculation of slopes with the shape function method is more involved than that of the previous method, but it is not difficult. The first step is to represent the surface deflection in its series formulation and take the derivatives with respect to $x$ and $y$

$$\frac{dZ_z}{dx} = \sum_{i=1}^{12} z_i \left( \frac{d\Psi_i}{dx} \right) \tag{5.11}$$

$$\frac{dZ_z}{dy} = \sum_{i=1}^{12} z_i \left( \frac{d\Psi_i}{dy} \right) \tag{5.12}$$

where $z_i$ are the nodal deflections for the given cell. The complication arises because we do not know the shape functions in terms of $x$ and $y$. However, we do know $x$, $y$, and $\Psi_i$ in terms of $\xi$ and $\eta$, so we can write the following

$$\left\{ \begin{array}{c} \frac{d\Psi_i}{d\xi} \\ \frac{d\Psi_i}{d\eta} \end{array} \right\} = \left[ \begin{array}{cc} \frac{\partial x}{\partial \xi} & \frac{\partial y}{\partial \xi} \\ \frac{\partial x}{\partial \eta} & \frac{\partial y}{\partial \eta} \end{array} \right] \left\{ \begin{array}{c} \frac{d\Psi_i}{dx} \\ \frac{d\Psi_i}{dy} \end{array} \right\} \tag{5.13}$$

where

$$\frac{\partial x}{\partial \xi} = \sum_{j=1}^{12} x_j \left( \frac{\partial \Psi_j}{\partial \xi} \right) \tag{5.14}$$

$$\frac{\partial x}{\partial \eta} = \sum_{j=1}^{12} x_j \left( \frac{\partial \Psi_j}{\partial \eta} \right) \tag{5.15}$$

$$\frac{\partial y}{\partial \xi} = \sum_{j=1}^{12} y_j \left( \frac{\partial \Psi_j}{\partial \xi} \right) \tag{5.16}$$

$$\frac{\partial y}{\partial \eta} = \sum_{j=1}^{12} y_j \left( \frac{\partial \Psi_j}{\partial \eta} \right) \tag{5.17}$$

Once again, it would be more appropriate to use the linear isoparametric functions given in Eq.(5.7) because $x$ and $y$ only vary linear along each grid line. However, for ease of programming, the cubic shape functions were used with a linear spline along the grid lines to determine the values of $x$ and $y$ along the side nodes.

Finally, the necessary derivatives of $\Psi_i$ can be found through a simple inversion.

$$\left\{ \begin{array}{c} \frac{d\Psi_i}{dx} \\ \frac{d\Psi_i}{dy} \end{array} \right\} = \left[ \begin{array}{cc} \frac{\partial x}{\partial \xi} & \frac{\partial y}{\partial \xi} \\ \frac{\partial x}{\partial \eta} & \frac{\partial y}{\partial \eta} \end{array} \right]^{-1} \left\{ \begin{array}{c} \frac{d\Psi_i}{d\xi} \\ \frac{d\Psi_i}{d\eta} \end{array} \right\} \tag{5.18}$$

These calculation can be found in almost any finite element text (see Ref. 20).

Again we have a very simple model to the interface, but now with a more general approach and significantly less logic. The order of interpolation of this method can easily be changed from linear to cubic, which may produce more accuracy in the results. Table 5.2 gives the resulting force and moment totals for a transfer of aerodynamic forces to the load set for the new method. The small difference between the aerodynamic set and the structural set occurs because the shape function method involves more equations, and truncation errors build up. The following sections will compare the results of the two methods and make a selection on which one to choose.

**Table 5.2.** Force and Moment Totals for Shape Functions

|  | Lift | X-Moment | Y-Moment |
|---|---|---|---|
| Linear | | | |
|    Exact | $1.5527 \times 10^4$N | $1.1137 \times 10^5$N·m | $-8.9618 \times 10^3$N·m |
|    Transferred | $1.5527 \times 10^4$N | $1.1137 \times 10^5$N·m | $-8.9633 \times 10^3$N·m |
| Cubic | | | |
|    Exact | $1.5527 \times 10^4$N | $1.1137 \times 10^5$N·m | $-8.9618 \times 10^3$N·m |
|    Transferred | $1.5527 \times 10^4$N | $1.1136 \times 10^5$N·m | $-8.7014 \times 10^3$N·m |

### 5.3. The A Matrix

Mentioned in section 4.2, the **A** matrix defines the influence of deformation on the aerodynamic forces, where $qa_{ij}$ is the change in force at node $i$, due to a unit displacement at node $j$. By thinking of the **A** matrix in this way, a method for its calculation is clear. A small perturbation is made at node $j$, and the resulting change in forces is divided by the magnitude of the perturbation and stored in the $j$th column of the **A** matrix. Once all of the nodes have been cycled through, the complete matrix has been found. Clearly, the accuracy of the **A** matrix is highly dependent on the aerodynamic–structural interface. Because of this dependence, we have a way to at least partially check the integrity of the interface model.

The first step in checking the **A** matrix (and consequently the interface model) is the proper selection of perturbation size. Since a uniform deflection of the wing should result in no change in force, the sum of the **A** matrix elements should be zero. Figure 5.5 represents the sum the of the **A** matrix verses the perturbation size for each of the interface models. Values larger than $1.0 \times 10^{-5}$m are to large because the response is non-linear, and values smaller than $1.0 \times 10^{-9}$m result in large truncation errors. The optimum perturbation size is around $1.0 \times 10^{-7}$m. All calculations are made on an IBM 3090 at double precision.

The next check of the models involves a measure of the accuracy of the **A** matrix. The accuracy for this test is a measure of how well $\mathbf{A}\boldsymbol{\theta}$ approximates the exact changes in the forces. The deformation is the same for all of the models so that an accurate comparison can be made. The comparison will be made by plotting the exact lift verses the approximate lift.

$$F_a = f_1(p, \alpha_0, \epsilon\boldsymbol{\theta}_0) \tag{5.19}$$

$$L_{exact} = \sum_{i=1}^{n} F_{a_i} \tag{5.20}$$

$$L_{approx} = L_0 + \sum_{i=1}^{n} q[a_{ij}][\epsilon\theta_{0_j}] \tag{5.21}$$

Where $\boldsymbol{\theta}_0$ is a set of deflections which is multiplied by a scalar $\epsilon$ that is varied from 0 to 1, and $\alpha_0$ is some initial angle of attack.* Figure 5.6 gives $L_{exact}$ and $L_{approx}$ for the previous interface model, while Figs. 5.7 and 5.8 give it for the linear and cubic surface splines respectively. It is easy to see that each method's approximation is linear and tangent to the exact calculations at the origin. Unfortunately, a direct comparison of the three plots cannot be made because the exact calculations also depend of the interface model used. What we can compare, is how well each of the models approximate their own exact solutions, with the error given by

$$\varepsilon = \sum_{i=1}^{n_p} \left| \Delta F_{a_{i_{exact}}} - \Delta F_{a_{i_{approx}}} \right| \Big/ \sum_{i=1}^{n_p} \left| \Delta F_{a_{i_{exact}}} \right| \tag{5.22}$$

$$\Delta F_{a_{exact}} = F_a - F_{a_0} \tag{5.23}$$

$$\Delta F_{a_{approx}} = q\mathbf{A}[\epsilon\boldsymbol{\theta}_0] \tag{5.24}$$

Figure 5.9 compares the error of each method as $\epsilon$ is increased. In each case the error is caused by the non-linearity of the response. From this figure it would seem that the cubic surface splines produce the lowest errors, but not by enough to justify its use based on accuracy alone.

---

\* $\theta_0$ was actually the elastic response of the wing at the initial design conditions with the linear shape function interface, and $\alpha_0$ was the rigid wing angle of attack.
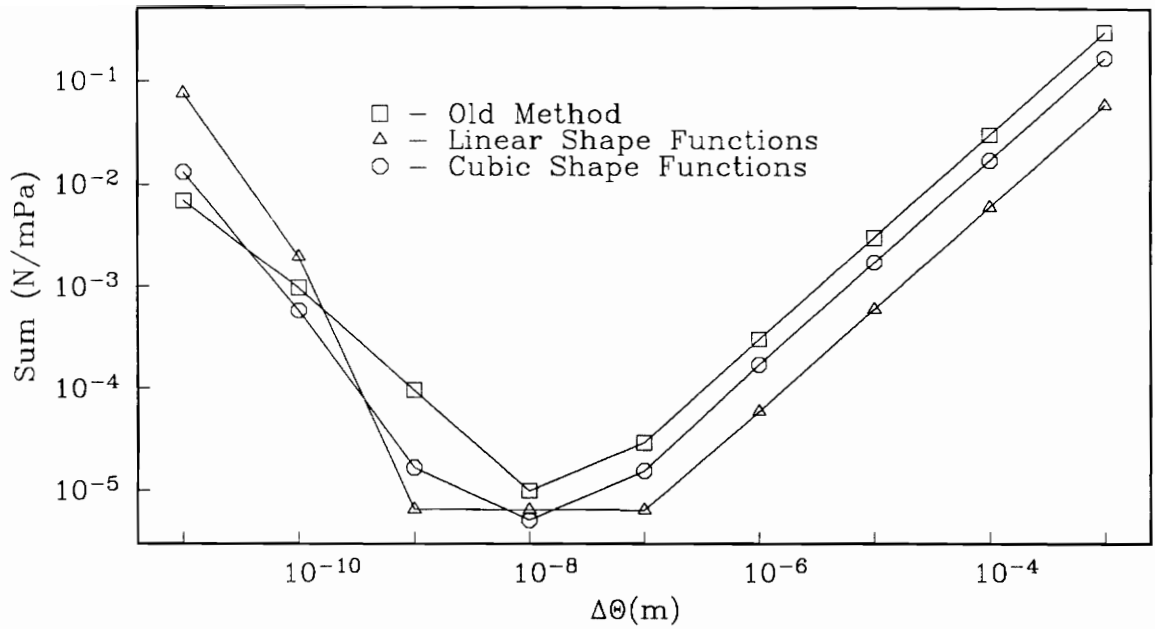
**Figure 5.5.** Sum of the **A** Matrix verses Step Size
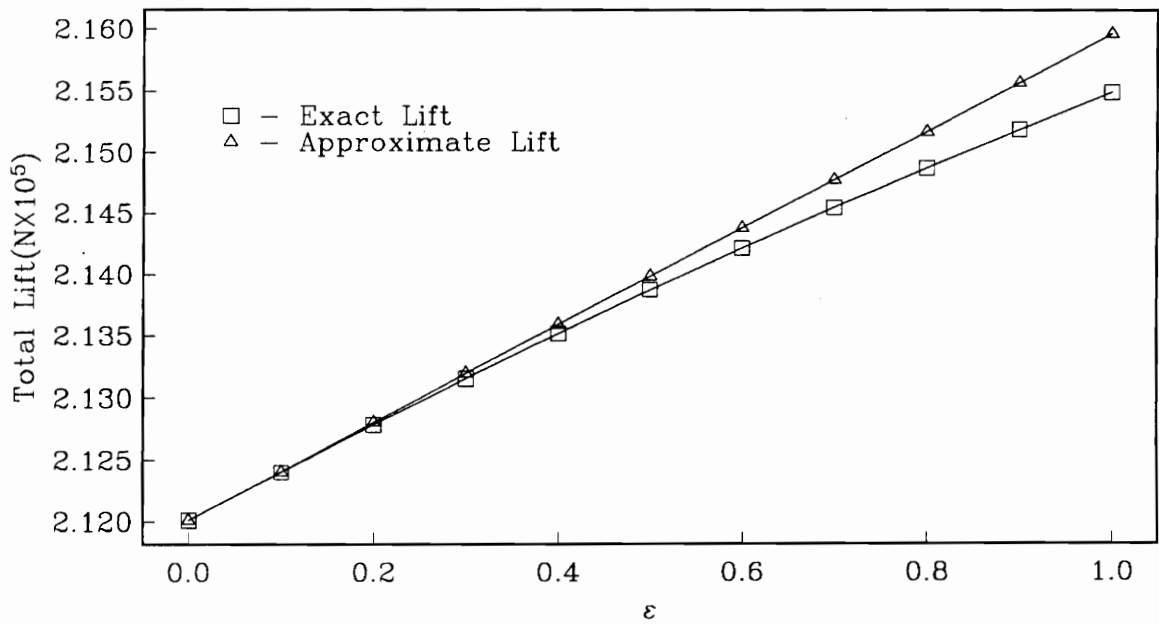


**Figure 5.6.** Exact and Approximate Lift for Old Approach
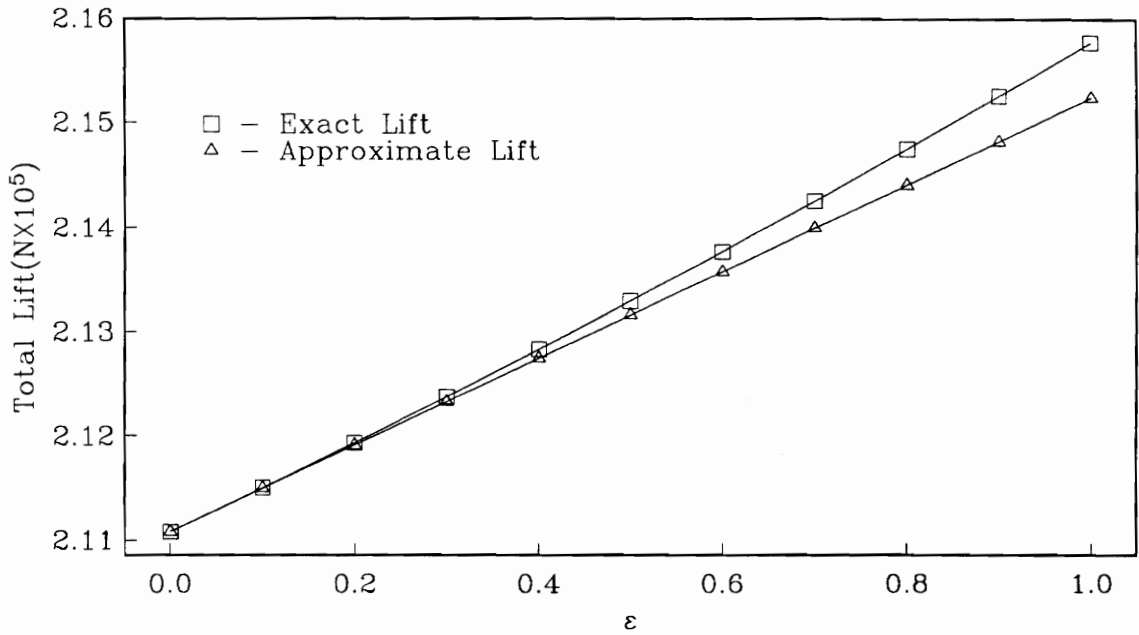
**Figure 5.7.** Exact and Approximate Lift for Linear Surface Splines
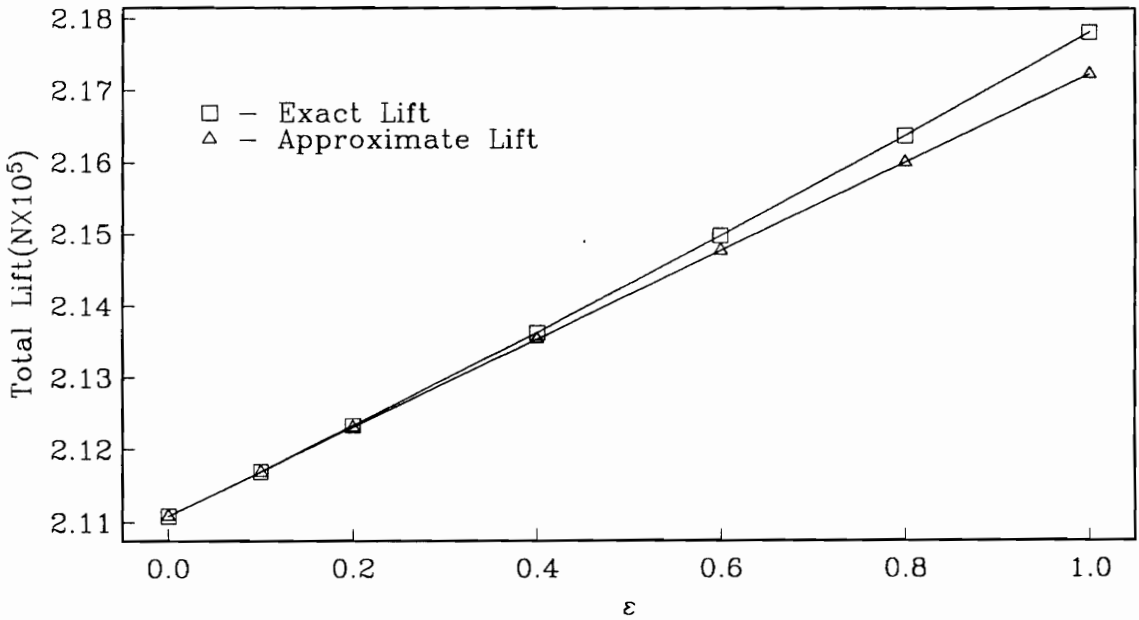


**Figure 5.8.** Exact and Approximate Lift for Cubic Surface Splines
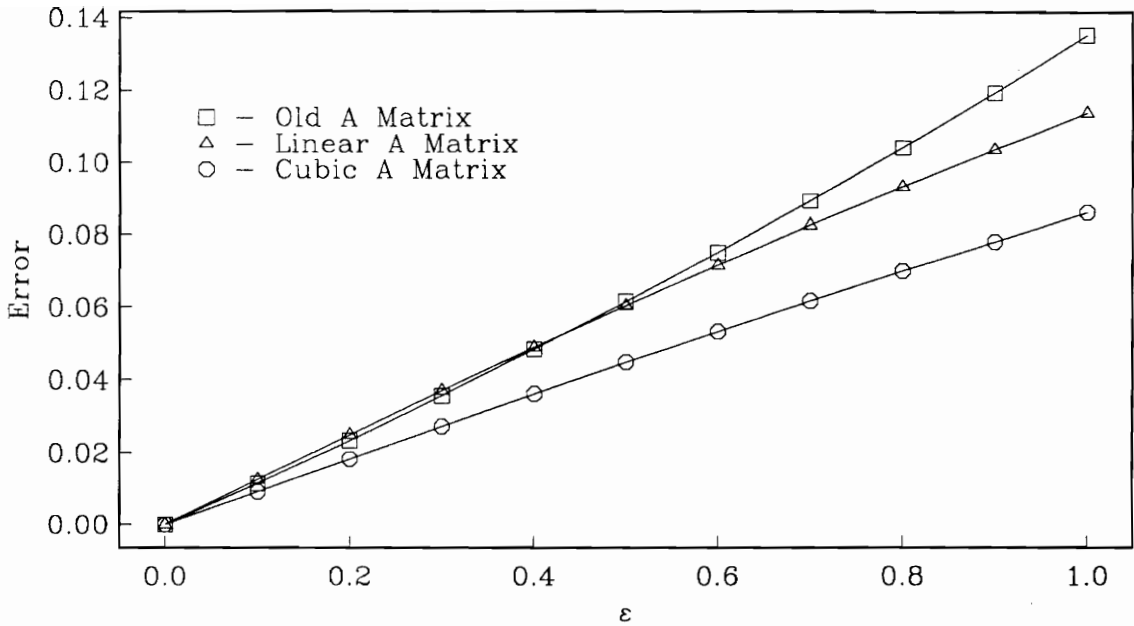
**Figure 5.9.** Error Comparison of the Three Methods

## 5.4. Interface Model Selection

In order to select an interface model one must consider not only the accuracy of the given method, but its computational cost. Based on the error calculations made in the previous section, the shape function approaches look to be the most accurate, with the cubic version slightly more accurate than the linear one. The shape function approaches also use much less CPU time than the previous method.* This savings is important because the transformation matrix will have to be calculated each time the planform is perturbed. Furthermore, the discontinuous behavior of the previous method as discussed in section 5.1 makes it very undesirable. Therefore, the shape function method will be used throughout the rest of the study with

---

* See table 5.3 and note that the CPU time for the linear approach could be reduced by approximately 20% if the four linear isoparametric functions are used.

the selection of the order to be determined when the accuracy of the sensitivity calculations is being considered (Chaps. 6 and 7).

Table 5.3. Run Time to Compute Interface Transformation Matrix

| Old Method | Linear Splines | Cubic Splines |
|:---:|:---:|:---:|
| 120.85s | 9.08s | 9.18s |

# 6. THE DRAG SENSITIVITY

## 6.0. Introduction

Crucial to the approximate optimization (Chap. 8), is the accurate calculation of the drag sensitivity. With this sensitivity, one can make a linear approximation of the drag which is assumed to be accurate in some small neighborhood near the design point in question. Since the sensitivity is the derivative of the drag with respect to each design variable, the computational cost could be considerable if efficient methods are not followed. The following sections detail the derivation of the sensitivities as given in Ref. 6, and discuss the numerical procedures necessary to obtain accurate results. These results are then presented for various cases to justify the final numerical approach, and to determine the source of any errors. Finally, the results obtained are compared to past research.

## 6.1. The Drag Sensitivity Formulation

As stated above, the drag sensitivity is simply the derivative of the drag with respect to each of the design variables. A simple brute force approach to this calculation would be to apply a forward difference with a small perturbation on a single design variable. Each forward difference would provide the derivative of the drag with respect to that design variable, holding the other variables constant.

$$D_i' = \frac{D(p + \Delta p_i) - D(p)}{||\Delta p_i||} \tag{6.1}$$

where $p$ is the vector of design variables and $\Delta p_i$ is a vector with the $i^{th}$ element equal to the perturbation and all other entries equal to zero. While this direct approach would calculate a very accurate tangent to the drag (providing that the correct $\Delta p_i$ is selected), it would be an extremely expensive method to employ. This

direct calculation of the flexible wing drag sensitivity would result in 3.25 hours of CPU time.* Since the drag needs to be approximated at several times during the design process, this large amount of CPU time is unacceptable. A more sensible approach can be found by recognizing a functional form of the drag in terms of $\alpha$, $\theta$, and $p$.

Looking back at section 4.1, we recall that the functional dependence for $F_a$ is as follows:

$$F_a = f_1(p, \alpha, \theta) \tag{4.3}$$

Since drag is a function of the lift, the drag can also be written as:

$$D = D(p, \alpha, \theta) \tag{6.2}$$

where we say that the drag is a function of the design variables, $p$, the angle of attack, $\alpha$, and the vertical deflections, $\theta$. Note that $\alpha$ and $\theta$ are actually functions of $p$, so Eq.(6.2) ultimately reduces to $D = D(p)$ to which Eq.(6.1) is applicable.

To determine the drag derivative in this form, the chain rule is employed to obtain:

$$D' = \left(\frac{\partial D}{\partial p}\right)_{\alpha,\theta} + \left(\frac{\partial D}{\partial \alpha}\right)_{p,\theta} \alpha' + \left(\frac{\partial D}{\partial \theta}\right)_{p,\alpha} \theta' \tag{6.3}$$

where

$$\alpha' = \frac{\partial \alpha}{\partial p}; \qquad \theta' = \frac{\partial \theta}{\partial p} \tag{6.4}$$

Traditionally, the values of $\alpha'$ and $\theta'$ are evaluated by differentiating Eqs.(4.13–4.15)[6], but this approach requires differentiating the **A** and **S** matrices with respect to $p$. This process is very expensive, and the total cost would approach that of the

---

* The majority of this time is in the evaluation of the A matrix and the aeroelastic formulation

direct analysis. If instead, we follow Ref. 6 and differentiate Eqs.(4.3, 4.4, and 4.7), we can obtain:

$$\mathbf{J}Y' = f'$$

where

$$Y' = \left\{ \begin{array}{c} F'_a \\ \alpha' \\ \theta' \end{array} \right\} \tag{6.5}$$

and

$$f' = \left\{ \begin{array}{c} f'_1 \\ f'_2 \\ f'_3 \end{array} \right\} \tag{6.6}$$

$$f'_i = \left( \frac{\partial f_i}{\partial p} \right)_{F_a, \alpha, \theta} \qquad i = 1, 2, 3 \tag{6.7}$$

Note that the Jacobian, $\mathbf{J}$, is exactly the same as that in Eq.(4.12), and once again we can partially solve the system to yield

$$(\mathbf{I} - q\mathbf{S}\mathbf{A}^x)\theta' = \mathbf{S}\mathbf{B}f'_1 + \frac{\mathbf{S}R}{\mathbf{N}^T R} f'_2 + f'_3 \tag{6.8}$$

$$\alpha' = \frac{f'_2 - \mathbf{N}^T f'_1 - q\mathbf{N}^T \mathbf{A}\theta'}{q\mathbf{N}^T R} \tag{6.9}$$

$$F'_a = f'_1 + qR\alpha' + q\mathbf{A}\theta' \tag{6.10}$$

This approach clearly uses no derivatives of $\mathbf{A}$ and $\mathbf{S}$; only the partial derivatives of $f_1$, $f_2$, and $f_3$ with respect to $p$ are needed ($F_a$, $\alpha$, and $\theta$ are fixed). Since these calculations are fairly inexpensive, this approach is considerably less expensive than that of the traditional and direct methods.* In the following sections, the numerical methods used for the evaluation of these sensitivities are analyzed.

---

\* This approach needs only an additional 163 seconds

## 6.2. The Numerical Evaluation of Sensitivity Terms

The first step necessary to evaluate Eqs.(6.8–6.10) is the determination of $f_1'$, $f_2'$, and $f_3'$. Each of these terms will be calculated using a forward difference and will result in either a vector or matrix quantity. Since these functions are treated as 'black boxes' as in section 4.2 the calculations are straightforward.

The $f_1$ function represents the aerodynamic processes, and returns a vector of forces at the load set nodes. A forward difference for $f_1'$ yields:

$$f_{1_j}' = \frac{f_1(p + \Delta p_j, \alpha, \theta) - f_1(p, \alpha, \theta)}{||\Delta p_j||} \tag{6.11}$$

where $f_{1_j}'$ is a vector which gives the derivative of the load set forces with respect to the $j^{th}$ design variable. The perturbation vector $\Delta p_j$ is exactly the same as that in section 6.1. Since the values of $\alpha$ and $\theta$ are held constant, $f_1$ is only affected by changes of the planform and the dynamic pressure. Therefore, $j$ only needs to be varied from 1 to 9, and the last 30 columns of the $f_1'$ matrix are set to zero. The final dimensions of $f_1'$ are the number of load set nodes $\times$ the number of design variables ($48 \times 39$).

The $f_2$ function represents a force balance for the aircraft. Recalling Eq.(4.4) we have

$$f_2(p, F_a) = \tfrac{1}{2} n W(p) - \mathbf{N}^T F_a \tag{4.4}$$

The derivative of this equation with respect to $p$ yields

$$f_2' = \tfrac{1}{2} n \frac{\partial W}{\partial p} \tag{6.12}$$

A forward difference gives us the following

$$f_{2_j}' = \tfrac{1}{2} n \frac{W(p + \Delta p_j) - W(p)}{||\Delta p_j||} \tag{6.13}$$

where $f_{2_j}$ is a scalar which represents the derivative of total aircraft weight with respect to the $j^{th}$ design variable. Note that weight does not depend on the dynamic pressure or the twist of the wing, so the derivatives with respect to the $7^{th}$, $8^{th}$, and $9^{th}$ design variables are zero. The final dimensions of $f_2'$ are $1 \times 39$.

The function $f_3$, gives the structural response of the wing and returns a vector of deflections at the load set nodes. The forward difference yields

$$f_{3_j}' = \frac{f_3(p + \Delta p_j, F_a) - f_3(p, F_a)}{||\Delta p_j||} \tag{6.14}$$

where $f_{3_j}'$ is a vector which represents the derivative of the deflections with respect to the $j^{th}$ design variable. Since the forces are held constant, the columns of $f_3'$ for the twists, dynamic pressure, and usable fuel are zero. The final dimensions for $f_3'$ are the same as that of $f_1'$.

The final function is the flexible wing drag. The calculation of this term is performed at the same time as that of $f_1'$. However, instead of a vector of force derivatives for each design variable, we get the scalar quantity of the drag derivative for each variable (Note that $\alpha$ and $\theta$ are still held fixed). The forward difference yields

$$\left(\frac{\partial D}{\partial p}\right)_{\alpha,\theta} = \frac{D(p + \Delta p_j, \alpha, \theta) - D(p, \alpha, \theta)}{||\Delta p_j||} \tag{6.15}$$

As for $f_1'$, the last 30 derivatives will be zero.

Looking at Eq.(6.3), we see the derivatives $\partial D/\partial \alpha$ and $\partial D/\partial \theta$. These terms are related to the $R$ vector and $A$ matrix respectively (recalling that $R = \partial F_a/\partial \alpha$ and $A = \partial F_a/\partial \theta$). Of these derivatives, $\partial D/\partial \alpha$ and the $R$ vector are the most trivial to calculate. For each, a forward difference with a small perturbation in angle of attack, yields the respective derivative.

$$R = \frac{f_1(p, \alpha + \Delta \alpha, \theta) - f_1(p, \alpha, \theta)}{\Delta \alpha} \tag{6.16}$$

and

$$\partial D / \partial \alpha = \frac{D(\boldsymbol{p}, \alpha + \Delta\alpha, \boldsymbol{\theta}) - D(\boldsymbol{p}, \alpha, \boldsymbol{\theta})}{\Delta\alpha} \qquad (6.17)$$

The final dimensions of the $\boldsymbol{R}$ vector are $48 \times 1$, while $\partial D / \partial \alpha$ is a scalar. The final unknown terms are the $\mathbf{A}$ matrix and $\partial D / \partial \boldsymbol{\theta}$. The calculation of the $\mathbf{A}$ matrix was discussed in detail in section 5.3, and $\partial D / \partial \boldsymbol{\theta}$ is calculated the same way with the result being a vector of drag derivatives, with dimensions $1 \times 48$, instead of a matrix of force derivatives.

## 6.3. Discussion and Comparison of Results

To this point the sensitivity analysis has been developed and computed in the same manner as that of previous research (with the exception of the aerodynamic-structural interface and the aerodynamic model). The results obtained in the past contained a significant number of assumptions which greatly affected the results. Furthermore, a parametric study of the accuracy was never performed so that a greater depth of understanding for the numerics was not possible. Figure 6.1 shows the exact and approximate drag verses relative design change for past research, where the change in design variables is given in table 6.1 (note that the structural terms represent values above the minimum gauge). Ideally, the approximation would be perfectly tangent to the exact drag at the initial point.* Clearly, there is a significant disparity between the approximation and the tangent. While some error may be expected because of the large number of calculations and finite difference approximations involved in the chaining process, it was felt that the error was excessive and some attempt should be made to improve it.

As mentioned in chapter 5, the selection of the interface model needs to be made at this time. The most rigorous approach to this selection would be to make the error

---

\* This would be obtained with the direct sensitivity calculation, but at a prohibitive cost

analysis that follows on each method. Unfortunately, preliminary investigations on the use of the cubic approach yielded problems with the calculation of divergence pressure and the associated sensitivity. For these calculations, unreasonable results were obtained for the case with the linear endpoints on the spline. The endpoint scheme was changed to a quadratic one and the result were no longer unreasonable. However, since a robust approach to the interface is desirable, further investigations will be limited to the linear surfaces, which still yield very good results. A more detailed explanation associated with the cubic interface will be reserved for the following chapter on divergence sensitivity.
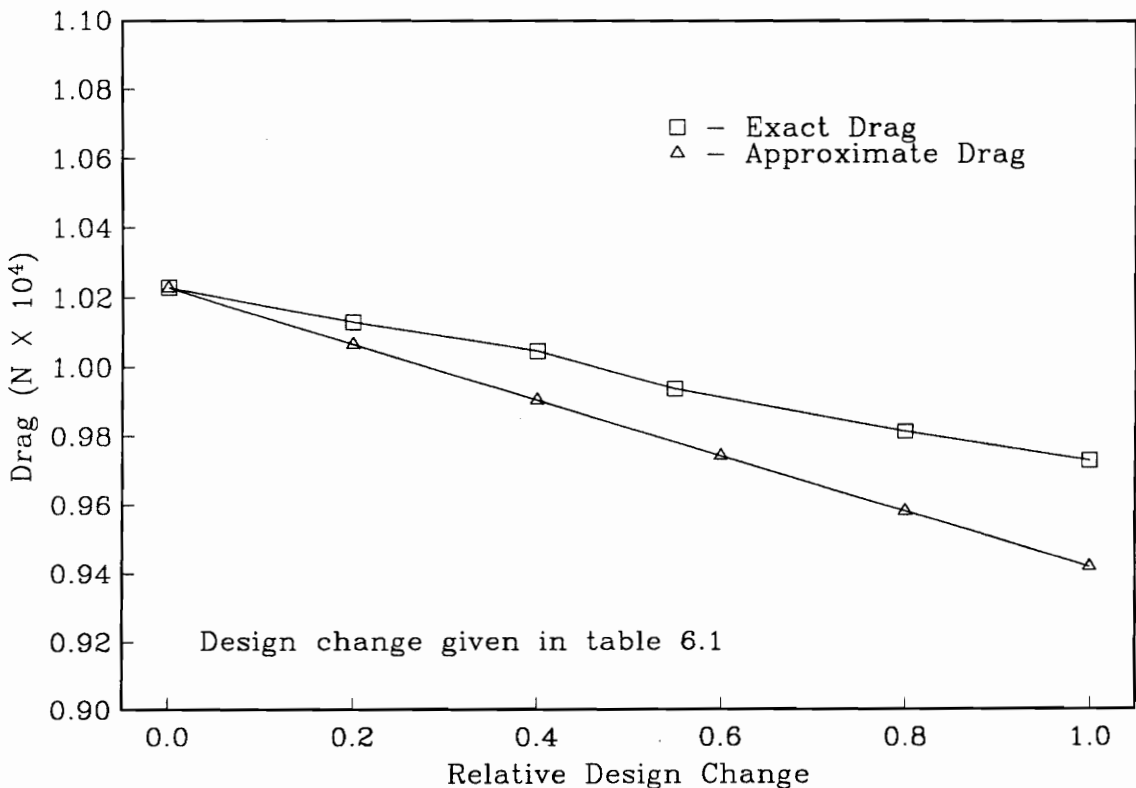


**Figure 6.1.** Exact and Approximate Drag for Previous Results

**Table 6.1.** Initial and Final States of Relative Design Change

| Variable | Initial State | Final State |
|---|---|---|
| 1 | $6.9163 \times 10^0$ m | $6.6402 \times 10^0$ m |
| 2 | $3.7650 \times 10^0$ m | $3.8706 \times 10^0$ m |
| 3 | $1.7250 \times 10^0$ m | $1.6570 \times 10^0$ m |
| 4 | $5.7537 \times 10^0$ m | $5.9919 \times 10^0$ m |
| 5 | $1.2248 \times 10^1$ m | $1.2744 \times 10^1$ m |
| 6 | $4.5500 \times 10^{-1}$ Rad | $3.9362 \times 10^{-1}$ Rad |
| 7 | $0.0000 \times 10^0$ Rad | $-3.1210 \times 10^{-2}$ Rad |
| 8 | $0.0000 \times 10^0$ Rad | $7.5000 \times 10^{-3}$ Rad |
| 9 | $2.6740 \times 10^3$ Pa | $2.8268 \times 10^3$ Pa |
| 10 | $2.1902 \times 10^4$ N | $2.3457 \times 10^4$ N |
| 11 | $7.6200 \times 10^{-7}$ m | $4.2207 \times 10^{-4}$ m |
| 12 | $7.6200 \times 10^{-7}$ m | $1.3149 \times 10^{-6}$ m |
| 13 | $7.6200 \times 10^{-7}$ m | $1.5642 \times 10^{-8}$ m |
| 14 | $7.6200 \times 10^{-7}$ m | $2.0236 \times 10^{-7}$ m |
| 15 | $8.5950 \times 10^{-5}$ m | $1.6315 \times 10^{-6}$ m |
| 16 | $4.2000 \times 10^{-4}$ m | $3.6612 \times 10^{-7}$ m |
| 17 | $7.6200 \times 10^{-7}$ m | $6.3300 \times 10^{-8}$ m |
| 18 | $7.6200 \times 10^{-6}$ m | $2.4323 \times 10^{-7}$ m |
| 19 | $2.0697 \times 10^{-3}$ m | $2.1523 \times 10^{-3}$ m |
| 20 | $2.3910 \times 10^{-3}$ m | $2.4862 \times 10^{-3}$ m |
| 21 | $3.2640 \times 10^{-3}$ m | $3.1336 \times 10^{-3}$ m |
| 22 | $2.3145 \times 10^{-3}$ m | $2.2222 \times 10^{-3}$ m |
| 23 | $7.6200 \times 10^{-3}$ m | $1.6375 \times 10^{-3}$ m |
| 24 | $7.6200 \times 10^{-3}$ m | $4.8575 \times 10^{-4}$ m |
| 25 | $7.6200 \times 10^{-3}$ m | $2.0868 \times 10^{-4}$ m |
| 26 | $7.6200 \times 10^{-3}$ m | $1.9452 \times 10^{-4}$ m |
| 27 | $9.3510 \times 10^{-2}$ m | $2.9506 \times 10^{-4}$ m |
| 28 | $7.6200 \times 10^{-3}$ m | $7.8316 \times 10^{-4}$ m |
| 29 | $7.6200 \times 10^{-3}$ m | $1.7946 \times 10^{-4}$ m |
| 30 | $7.6200 \times 10^{-3}$ m | $2.3646 \times 10^{-4}$ m |
| 31 | $2.3460 \times 10^{-3}$ m | $2.2535 \times 10^{-3}$ m |
| 32 | $3.3150 \times 10^{-3}$ m | $3.1830 \times 10^{-3}$ m |
| 33 | $4.7430 \times 10^{-3}$ m | $4.5535 \times 10^{-3}$ m |
| 34 | $2.2128 \times 10^{-3}$ m | $2.1247 \times 10^{-3}$ m |
| 35 | $1.4025 \times 10^{-3}$ m$^2$ | $1.2622 \times 10^{-3}$ m$^2$ |
| 36 | $8.1930 \times 10^{-4}$ m$^2$ | $3.1662 \times 10^{-9}$ m$^2$ |
| 37 | $7.5330 \times 10^{-5}$ m$^2$ | $4.8013 \times 10^{-8}$ m$^2$ |
| 38 | $3.1620 \times 10^{-5}$ m$^2$ | $5.6171 \times 10^{-8}$ m$^2$ |
| 39 | $4.7439 \times 10^{-1}$ Rad | $3.3350 \times 10^{-1}$ Rad |

**Table 6.2.** Direct Drag Sensitivity Results

| Variable | $\alpha'$ (Rad/m) | $D'$ (N/m) |
|---|---|---|
| 1 | $-3.190\times10^{-3}$ | $2.385\times10^{2}$ |
| 2 | $-2.204\times10^{-2}$ | $1.579\times10^{2}$ |
| 3 | $-1.702\times10^{-2}$ | $-1.301\times10^{2}$ |
| 4 | $-2.134\times10^{-2}$ | $-8.386\times10^{2}$ |
| 5 | $-1.366\times10^{-2}$ | $-8.536\times10^{2}$ |
| 6 | $3.135\times10^{-2}$ | $1.939\times10^{3}$ |
| 7* | $-7.463\times10^{-1}$ | $-7.428\times10^{3}$ |
| 8* | $-2.233\times10^{-1}$ | $-3.429\times10^{3}$ |
| * Derivatives are per radian | | |

Table 6.2 gives the results for the direct sensitivity calculation for the first eight design variables with the nominal set of initial conditions (see table 8.1). Since the direct calculation will in fact give the exact tangent to drag calculation, this table will give us results with which to compare the computed sensitivities. While more than the first eight variables would be useful, the excessive cost of the calculation limited the list to the planform variables. This was considered only a minor problem because these derivatives are significantly larger (thus having the greatest impact on the analysis) than the others, and they had the largest error. A preliminary investigation determined that the total error in drag prediction with respect to the other 31 variables was approximately 3%, which is quite acceptable.

### 6.3.1. The Initial Results and Improvements

The first step in the error analysis was the selection of a baseline case with which to start. This case makes most of the same assumptions as in the past but with the new interface and aerodynamic models. Another major difference between this case and the old one involves the transformation matrix calculated in the interface model. In the past is was assumed that this matrix was not significantly changed

by small perturbations in the planform design variables. While this assumption is obviously not true, the computational costs associated with the previous interface model probably eliminated the possibility of updating this matrix as needed. Since the new model uses significantly less computational time, there is no need to continue this assumption.

The results in the baseline case for the angle of attack sensitivity, $\alpha'$, and the drag sensitivity, $D'$, are given in table 6.3. A listing of $\theta'$ and $F'_a$ would also be useful, but since each of these is a matrix, it would be difficult to represent them with any brevity. One quickly notices that the error associated with the angle of attack sensitivities is reasonably small and acceptable, so it is reasonable to assume that $\theta'$ has a similar amount of error. $F'_a$ may have a slightly larger amount of error because any small amount of error in $\theta'$ and $\alpha'$ will have an effect on this calculation. However, it is still reasonable to assume that the error is acceptable. The sensitivity associated with the drag has a significantly larger error especially with design variables 2, 3, 6, and 7. A similar table of derivatives and errors for the previous results would be useful, but such calculations were never performed. However, figure 6.2 illustrates that there is still a significant improvement in the overall drag prediction as compared to previous results over the same variation in design variable (see table 6.1).

**Table 6.3.** Baseline Drag Sensitivity Results

| Variable | $\alpha'$ (Rad/m) | $|\text{Error}(\alpha')|$ | $D'$ (N/m) | $|\text{Error}(D')|$ |
|---|---|---|---|---|
| 1 | $-3.127\times10^{-3}$ | 2.0% | $2.443\times10^{2}$ | 2.4% |
| 2 | $-2.184\times10^{-2}$ | 0.9% | $2.360\times10^{2}$ | 49.5% |
| 3 | $-1.709\times10^{-2}$ | 0.4% | $-1.060\times10^{2}$ | 18.5% |
| 4 | $-2.076\times10^{-2}$ | 2.7% | $-7.819\times10^{2}$ | 6.8% |
| 5 | $-1.312\times10^{-2}$ | 4.0% | $-8.389\times10^{2}$ | 1.7% |
| 6 | $2.915\times10^{-2}$ | 7.0% | $1.115\times10^{3}$ | 42.5% |
| 7* | $-7.286\times10^{-1}$ | 2.4% | $-5.341\times10^{3}$ | 28.1% |
| 8* | $-2.188\times10^{-1}$ | 2.0% | $-3.019\times10^{3}$ | 12.0% |
| * Derivatives are per radian | | | | |
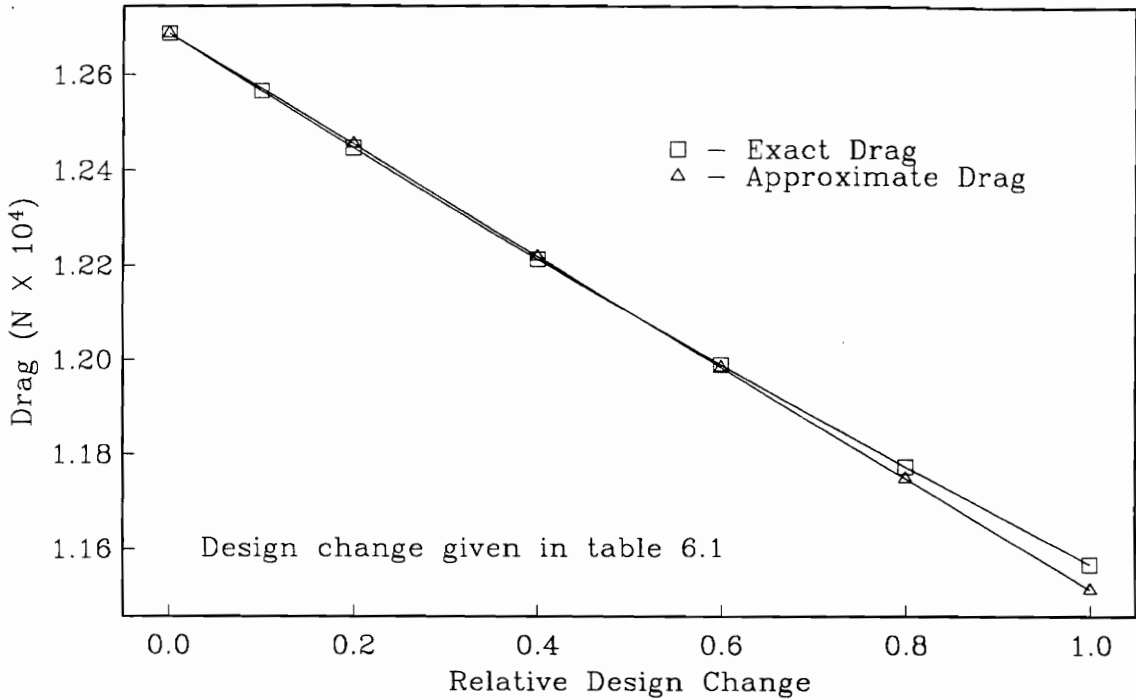
**Figure 6.2.** Exact and Approximate Drag for Baseline Case

The second assumption to be considered was the design point at which $\partial D/\partial \theta$ is calculated. In previous research, this quantity was determined at the rigid wing conditions $(\alpha = \alpha_r,\ \theta = 0)$ and assumed to not change much from that point. This term should be calculated at the flexible wing conditions, since the flexible wing drag is the quantity being approximated. The justification behind this assumption may again have been computational time considerations. Since $\partial D/\partial \theta$ and the **A** matrix are calculated at exactly the same time, the derivative is at the rigid wing conditions where the **A** matrix is first calculated. Table 6.4 gives the new sensitivity results with the removal of this assumption. There is clearly a very significant improvement in the second, third, and sixth terms, with a slight degradation in a few of the terms. The overall result in drag prediction is more accurate, and this increased accuracy more than justifies the additional 225 second cost.

**Table 6.4.** Drag Sensitivity Results with Correct $\partial D/\partial \theta$

| Variable | $\alpha'$ (Rad/m) | \|Error($\alpha'$)\| | $D'$ (N/m) | \|Error($D'$)\| |
|:---:|:---:|:---:|:---:|:---:|
| 1 | $-3.127\times10^{-3}$ | 2.0% | $2.435\times10^{2}$ | 2.1% |
| 2 | $-2.184\times10^{-2}$ | 0.9% | $1.762\times10^{2}$ | 11.6% |
| 3 | $-1.709\times10^{-2}$ | 0.4% | $-1.346\times10^{2}$ | 3.5% |
| 4 | $-2.076\times10^{-2}$ | 2.7% | $-7.919\times10^{2}$ | 5.6% |
| 5 | $-1.312\times10^{-2}$ | 4.0% | $-8.089\times10^{2}$ | 5.2% |
| 6 | $2.915\times10^{-2}$ | 7.0% | $1.788\times10^{3}$ | 7.8% |
| 7* | $-7.286\times10^{-1}$ | 2.4% | $-5.261\times10^{3}$ | 29.2% |
| 8* | $-2.188\times10^{-1}$ | 2.0% | $-2.875\times10^{3}$ | 16.2% |
| * Derivatives are per radian | | | | |

### 6.3.2. Perturbation Size Considerations

At this time, it was decided to analyze some of the step size selections for the various sensitivity calculations. In section 5.3 this analysis was made for the calculation of the **A** matrix. Since this matrix is closely related to $\partial D/\partial \theta$, this analysis was assumed to also be adequate for $\partial D/\partial \theta$, and the perturbation in $\theta$ was left at its optimal value.

Another step size selected in the past involves the structural 'black box', $f_3$, and the weight. The selection of a step size for the weight sensitivity, $W'$, proved to be a difficult task. A 'flat region' where there is little variation in the finite difference calculation verses the perturbation size was never found. At perturbations smaller than $1\times10^{-2}$m, the difference calculation yielded erratic results.* The final decision was to leave the perturbation at these lower bounds, which is the value selected by P.J. Kao[5] and M. Rais-Rohani. The step size selections for $f_3'$ was also left at the value selected by P.J. Kao[5].

---

    *   Note that the structural thicknesses were scaled by $1\times10^{3}$ so the perturbation for these terms would be $1\times10^{-5}$m. The usable fuel was scaled by $1\times10^{-4}$ which yields a perturbation size of $1\times10^{2}$N. The step size for the dynamic pressure was fixed at 10Pa. For the twist and sweep terms the units are in radians.

The selection in the perturbation size for the calculation of the $R$ vector and $\partial D/\partial \alpha$ also proved to be difficult. A similar lack of a 'flat region' as before was responsible for for the problem. Values of $\Delta \alpha$ smaller than $1 \times 10^{-2}$deg also produced erratic results due to truncation error. The final selection of this perturbation size was left at $1°$ as selected by D. Polen[6] in previous research as it seems to produce reasonably good results.

The final perturbation size to be considered is the one for $f_1'$ and $(\partial D/\partial p)_{\alpha,\theta}$. The easiest way to analyze the impact of the perturbation on these terms is to vary the step size and look at the resulting changes in the angle of attack and drag sensitivities. The baseline case above, has a perturbation of $1 \times 10^{-2}$m (units are in radians for the twist, sweep, and orientation terms, and in Pa. for the dynamic pressure). This value was reduced to $1 \times 10^{-5}$m in order of magnitude steps. The results are given in tables 6.5–6.7. The reduction in step size to $1 \times 10^{-3}$m clearly has a positive impact on some of the sensitivities. This gives the conclusion that baseline value of $1 \times 10^{-2}$m is too large. Since the sensitivities do not significantly change when the value is reduced further, the value was selected to be $1 \times 10^{-3}$m.

**Table 6.5.** Drag Sensitivity Results with $\Delta p_i = 1 \times 10^{-3}$m

| Variable | $\alpha'$ (Rad/m) | $|\text{Error}(\alpha')|$ | $D'$ (N/m) | $|\text{Error}(D')|$ |
|:---:|:---:|:---:|:---:|:---:|
| 1 | $-3.130 \times 10^{-3}$ | 1.9% | $2.435 \times 10^2$ | 2.1% |
| 2 | $-2.185 \times 10^{-2}$ | 0.9% | $1.749 \times 10^2$ | 10.8% |
| 3 | $-1.710 \times 10^{-2}$ | 0.5% | $-1.360 \times 10^2$ | 4.6% |
| 4 | $-2.076 \times 10^{-2}$ | 2.7% | $-7.916 \times 10^2$ | 5.6% |
| 5 | $-1.312 \times 10^{-2}$ | 4.0% | $-8.089 \times 10^2$ | 5.2% |
| 6 | $2.740 \times 10^{-2}$ | 12.6% | $1.733 \times 10^3$ | 10.7% |
| 7* | $-7.298 \times 10^{-1}$ | 2.2% | $-6.036 \times 10^3$ | 18.7% |
| 8* | $-2.191 \times 10^{-1}$ | 1.9% | $-3.083 \times 10^3$ | 10.1% |
| * Derivatives are per radian | | | | |

**Table 6.6.** Drag Sensitivity Results with $\Delta p_i = 1\times10^{-4}$m

| Variable | $\alpha'$ (Rad/m) | $|\text{Error}(\alpha')|$ | $D'$ (N/m) | $|\text{Error}(D')|$ |
|---|---|---|---|---|
| 1 | $-3.131\times10^{-3}$ | 1.8% | $2.435\times10^2$ | 2.1% |
| 2 | $-2.185\times10^{-2}$ | 0.9% | $1.747\times10^2$ | 10.6% |
| 3 | $-1.711\times10^{-2}$ | 0.5% | $-1.362\times10^2$ | 4.8% |
| 4 | $-2.076\times10^{-2}$ | 2.7% | $-7.916\times10^2$ | 5.6% |
| 5 | $-1.312\times10^{-2}$ | 4.0% | $-8.089\times10^2$ | 5.2% |
| 6 | $2.732\times10^{-2}$ | 12.9% | $1.730\times10^3$ | 10.8% |
| 7* | $-7.300\times10^{-1}$ | 2.2% | $-6.113\times10^3$ | 17.7% |
| 8* | $-2.191\times10^{-1}$ | 1.9% | $-3.104\times10^3$ | 9.5% |
| * Derivatives are per radian | | | | |

**Table 6.7.** Drag Sensitivity Results with $\Delta p_i = 1\times10^{-5}$m

| Variable | $\alpha'$ (Rad/m) | $|\text{Error}(\alpha')|$ | $D'$ (N/m) | $|\text{Error}(D')|$ |
|---|---|---|---|---|
| 1 | $-3.131\times10^{-3}$ | 2.1% | $2.435\times10^2$ | 2.1% |
| 2 | $-2.185\times10^{-2}$ | 0.9% | $1.745\times10^2$ | 10.5% |
| 3 | $-1.711\times10^{-2}$ | 0.5% | $-1.362\times10^2$ | 4.8% |
| 4 | $-2.076\times10^{-2}$ | 2.7% | $-7.916\times10^2$ | 5.6% |
| 5 | $-1.312\times10^{-2}$ | 4.0% | $-8.089\times10^2$ | 5.2% |
| 6 | $2.731\times10^{-2}$ | 12.9% | $1.729\times10^3$ | 10.8% |
| 7* | $-7.300\times10^{-1}$ | 2.2% | $-6.121\times10^3$ | 17.6% |
| 8* | $-2.191\times10^{-1}$ | 1.9% | $-3.106\times10^3$ | 9.4% |
| * Derivatives are per radian | | | | |

### 6.3.3. The Final Investigations

Recalling the past assumption made in the calculation of $\partial D/\partial\theta$, we see the same assumption has been made for the **A** matrix and $R$ vector. These quantities are needed for the rigid angle of attack determination and aeroelastic formulation, so they obviously do not initially use the deflection information or the flexible angle of attack. Again the assumption states that these terms are not affected by the inclusion of the flexible terms. Since both the **A** matrix and $R$ vector are involved

in Eqs.(6.8–6.10) this may have a detrimental effect on the sensitivity calculations. Tables (6.8–6.10) present the results for variously updating one or both of the terms (compare with table 6.5). Quite surprisingly, any updating of the **A** matrix results in adverse effects on the sensitivities. A possible explanation of this result could be a lower accuracy in the calculation of the **A** matrix when deflections are present. Since the entire problem is very sensitive to any errors in the **A** matrix, even small disturbances to accuracy can have drastic results. In any case, the errors associated with not updating the **A** matrix are not extremely significant. Updating the *R* vector alone actually improves the results significantly. Unfortunately, updating the *R* vector alone is not mathematically sound, so no updating of either term is performed.

A final analysis was performed to determine the effect of not updating the influence transformation matrix. While this is an incorrect assumption it is consistent to what was done in the past, and it would save some computational time (approximately 60 seconds per design cycle). The results are presented in table 6.11 and the sensitivities are actually not affected too adversely (compare with table 6.5). Unfortunately, this result does not hold true for the divergence sensitivity (see Chap. 7) so the updates are performed.

Table **6.8.** Drag Sensitivity Results with Updated **A** and *R*

| Variable | $\alpha'$ (Rad/m) | $|\text{Error}(\alpha')|$ | **D'** (N/m) | $|\text{Error}(D')|$ |
|:---:|:---:|:---:|:---:|:---:|
| 1 | $-3.140\times10^{-3}$ | 1.6% | $2.420\times10^{2}$ | 1.5% |
| 2 | $-2.122\times10^{-2}$ | 3.7% | $2.213\times10^{2}$ | 40.2% |
| 3 | $-1.683\times10^{-2}$ | 1.1% | $-1.174\times10^{2}$ | 9.7% |
| 4 | $-2.077\times10^{-2}$ | 2.6% | $-7.974\times10^{2}$ | 4.9% |
| 5 | $-1.360\times10^{-2}$ | 0.4% | $-8.507\times10^{2}$ | 0.3% |
| 6 | $1.970\times10^{-2}$ | 37.2% | $1.111\times10^{3}$ | 42.7% |
| 7* | $-7.358\times10^{-1}$ | 1.4% | $-6.679\times10^{3}$ | 10.1% |
| 8* | $-2.224\times10^{-1}$ | 0.4% | $-3.399\times10^{3}$ | 0.9% |
| * Derivatives are per radian | | | | |

Table 6.9. Drag Sensitivity Results with Updated **A**

| Variable | $\alpha'$ (Rad/m) | \|Error($\alpha'$)\| | D' (N/m) | \|Error(D')\| |
|---|---|---|---|---|
| 1 | $-3.119\times10^{-3}$ | 2.2% | $2.444\times10^{2}$ | 2.5% |
| 2 | $-2.107\times10^{-2}$ | 4.4% | $2.374\times10^{2}$ | 50.3% |
| 3 | $-1.671\times10^{-2}$ | 1.8% | $-1.046\times10^{2}$ | 19.5% |
| 4 | $-2.064\times10^{-2}$ | 3.3% | $-7.815\times10^{2}$ | 6.8% |
| 5 | $-1.351\times10^{-2}$ | 1.1% | $-8.404\times10^{2}$ | 1.5% |
| 6 | $1.957\times10^{-2}$ | 37.6% | $1.096\times10^{3}$ | 43.5% |
| 7* | $-7.309\times10^{-1}$ | 2.1% | $-6.119\times10^{3}$ | 17.6% |
| 8* | $-2.209\times10^{-1}$ | 1.1% | $-3.230\times10^{3}$ | 5.8% |
| * Derivatives are per radian | | | | |

Table 6.10. Drag Sensitivity Results with Updated **R**

| Variable | $\alpha'$ (Rad/m) | \|Error($\alpha'$)\| | D' (N/m) | \|Error(D')\| |
|---|---|---|---|---|
| 1 | $-3.153\times10^{-3}$ | 1.2% | $2.410\times10^{2}$ | 1.0% |
| 2 | $-2.201\times10^{-2}$ | 0.1% | $1.574\times10^{2}$ | 0.3% |
| 3 | $-1.723\times10^{-2}$ | 1.2% | $-1.497\times10^{2}$ | 15.1% |
| 4 | $-2.091\times10^{-2}$ | 2.0% | $-8.082\times10^{2}$ | 3.6% |
| 5 | $-1.321\times10^{-2}$ | 3.3% | $-8.193\times10^{2}$ | 4.0% |
| 6 | $2.760\times10^{-2}$ | 12.0% | $1.755\times10^{3}$ | 9.5% |
| 7* | $-7.350\times10^{-1}$ | 1.5% | $-6.619\times10^{3}$ | 10.9% |
| 8* | $-2.207\times10^{-1}$ | 1.2% | $-3.258\times10^{3}$ | 5.0% |
| * Derivatives are per radian | | | | |

Table 6.11. Drag Sensitivity Results with no Update on **D**

| Variable | $\alpha'$ (Rad/m) | \|Error($\alpha'$)\| | D' (N/m) | \|Error(D')\| |
|---|---|---|---|---|
| 1 | $-3.138\times10^{-3}$ | 1.6% | $2.442\times10^{2}$ | 2.4% |
| 2 | $-2.195\times10^{-2}$ | 0.4% | $1.776\times10^{2}$ | 12.5% |
| 3 | $-1.680\times10^{-2}$ | 1.3% | $-1.336\times10^{2}$ | 2.8% |
| 4 | $-2.079\times10^{-2}$ | 2.6% | $-7.913\times10^{2}$ | 5.6% |
| 5 | $-1.339\times10^{-2}$ | 2.0% | $-8.133\times10^{2}$ | 4.7% |
| 6 | $3.881\times10^{-2}$ | 23.8% | $1.856\times10^{3}$ | 4.3% |
| 7* | $-7.298\times10^{-1}$ | 2.2% | $-6.036\times10^{3}$ | 18.7% |
| 8* | $-2.191\times10^{-1}$ | 1.9% | $-3.083\times10^{3}$ | 10.1% |
| * Derivatives are per radian | | | | |

## 6.4. Conclusions for the Drag Sensitivity

This analysis indicated that the best results where obtained with updating the influence transformation matrix, performing the $\partial D/\partial \theta$ calculation at the flexible wing conditions, and selecting the perturbation for the design variable vector to be $1 \times 10^{-3}$m for the calulation of $f_1'$ and $\partial D/\partial p$ (other perturbations were left at their previous values). Furthermore, the new interface and aerodynamic models clearly had a very positive impact with the majority of this improvement coming from the new drag calculations. The net results of this analysis provided a much improved drag approximation which is verified in figure 6.3 (range of design variables is once again given in table 6.1). An additional test of the analysis is provided in figure 6.4, where approximate and exact drags are compared over a different set of initial and final conditions. And finally as indicated in chapter 5, the discontinuous behavior of the exact drag was eliminated. The next chapter looks at obtaining similar success for the divergence sensitivity.
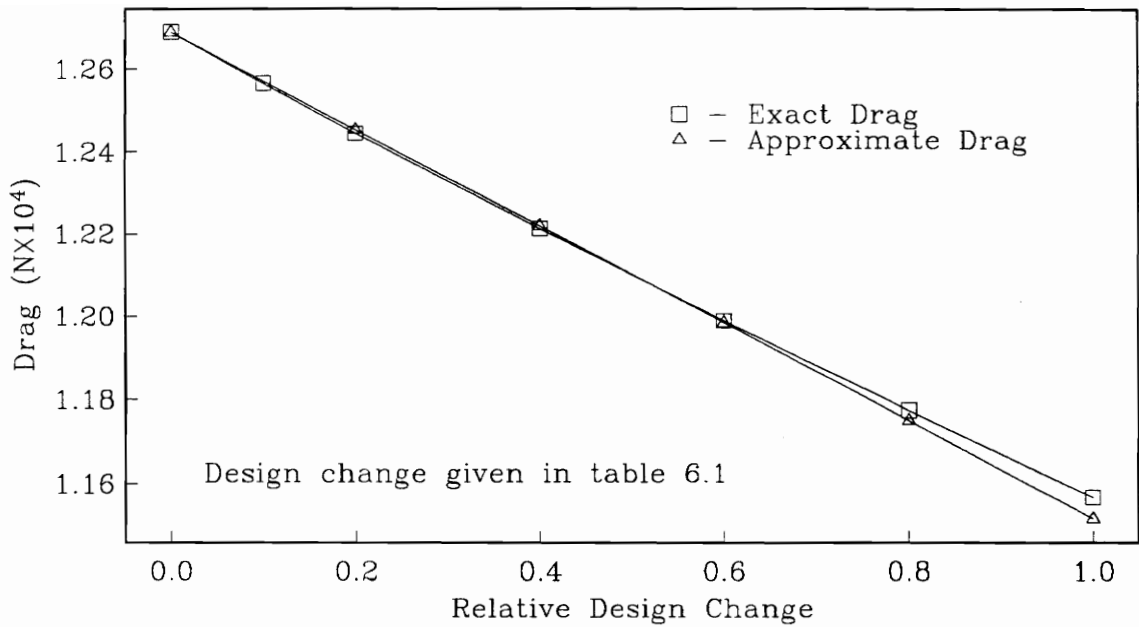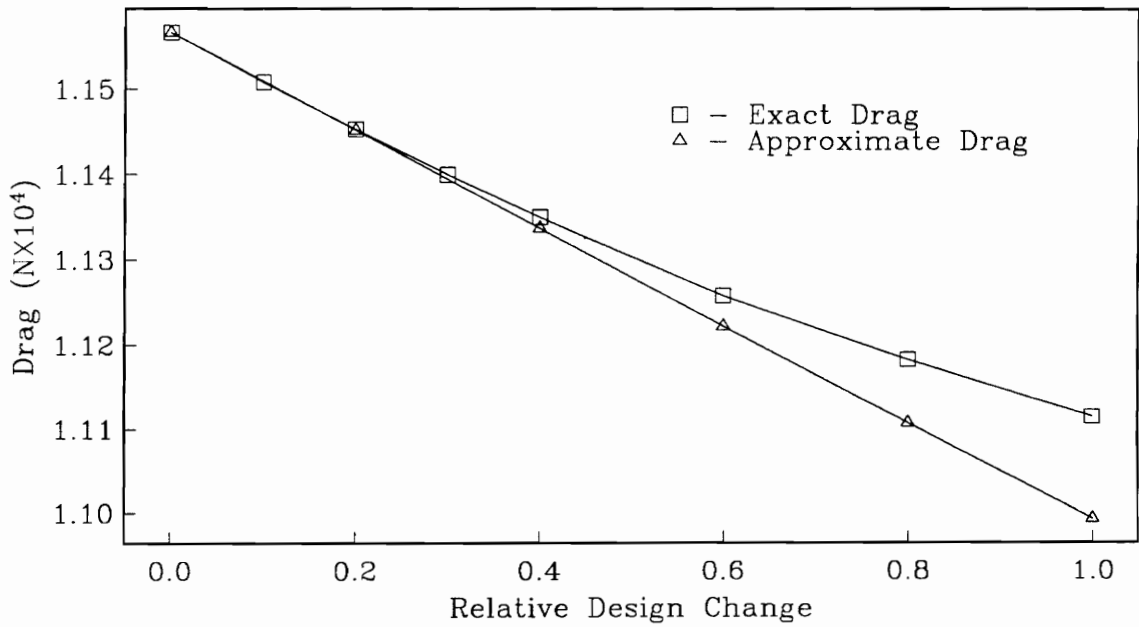
**Figure 6.3.** Final Approximation of the Drag



**Figure 6.4.** Drag Approximation with Different Range of Design Variables

# 7. THE DIVERGENCE SENSITIVITY

## 7.0. Introduction

As with the drag, the divergence sensitivity is an important part of the approximate optimization. Once again, a linear approximation will be used to model the divergence pressure in some small neighborhood. In many aircraft, the divergence pressure is a critical constraint which influences the design. For the present wing design study, the divergence may or may not be critical. Certainly the use of a forward sweep adversely effects the divergence pressure, but this will hopefully be offset with the variability of the ply orientation. The formulation which follows was developed in previous research, however the numerical modeling of the problem was never successfully completed.

## 7.1. The Divergence Sensitivity Formulation

A simple brute force approach to the divergence sensitivity could be applied here just as it could for the drag

$$\left(\frac{\partial q_D}{\partial p_i}\right) = \frac{q_D(p + \Delta p_i) - q_D(p)}{||\Delta p_i||} \tag{7.1}$$

where $p$ and $\Delta p_i$ are defined as in Eq.(6.1). Again, the drawback of this approach is the prohibitive cost. However, the application of the direct approach will provide values that can be used for accuracy checks. Once again, it is necessary to determine a much more efficient approach to extract the derivatives of the divergence pressure.

This efficient approach can be found in Ref. 6 and involves differentiating Eq.(4.21) with respect to $p$ to yield

$$\begin{bmatrix} \mathbf{I} & -q_D\mathbf{A} \\ -\mathbf{S} & \mathbf{I} \end{bmatrix} \left\{ \begin{matrix} F'_{aD} \\ \theta'_D \end{matrix} \right\} + \begin{bmatrix} 0 & -(q_D\mathbf{A})' \\ -\mathbf{S}' & 0 \end{bmatrix} \left\{ \begin{matrix} F_{aD} \\ \theta_D \end{matrix} \right\} = 0 \tag{7.2}$$

If we continue following Ref. 6, this equation is multiplied by the left eigenvector, $[F_{aL}^T, \theta_L^T]$, which is defined by

$$[F_{aL}^T, \theta_L^T] \begin{bmatrix} \mathbf{I} & -q_D\mathbf{A} \\ -\mathbf{S} & \mathbf{I} \end{bmatrix} = 0$$

to obtain

$$[F_{aL}^T, \theta_L^T] \begin{bmatrix} 0 & -(q_D\mathbf{A})' \\ -\mathbf{S}' & 0 \end{bmatrix} \left\{ \begin{array}{c} F_{aD} \\ \theta_D \end{array} \right\} = 0 \qquad (7.3)$$

Solving for $q_D'$ we obtain

$$q_D' = -\frac{q_D F_{aL}^T \mathbf{A}' \theta_D + \theta_L^T \mathbf{S}' F_{aD}}{F_{aL}^T \mathbf{A} \theta_D} \qquad (7.4)$$

Unfortunately, the above equation contains derivatives of $\mathbf{A}$ and $\mathbf{S}$ for which care was taken to avoid in the drag calculations. However, this problem can be simplified by looking at the definitions of the respective terms. Looking at $\mathbf{A}'\theta_D$, we see

$$q\mathbf{A}'\theta_D = \frac{\partial}{\partial p}\left(\frac{\partial f_1}{\partial \theta}\right)\theta_D \qquad (7.5)$$

With this formulation it is possible to obtain $q\mathbf{A}'\theta_D$ without calculating $\mathbf{A}'$. This process is outlined in Ref. 6 and represents a considerable time savings. Begin by considering a generic case where $f$ is a function of a vector $X$, and $D$ is a unit vector. The scalar product of $\partial f/\partial X$ and $D$ represents the directional derivative of $f$ in the direction $D$, i.e.

$$\begin{aligned}
\frac{\partial f}{\partial X}\bigg|_{X_0} D &= \lim_{\epsilon \to 0} \frac{1}{\epsilon}[f(X_0 + \epsilon D) - f(X_0)] \\
&= \frac{d}{d\epsilon}[f(X_0 + \epsilon D)]_{\epsilon=0} \qquad (7.6)
\end{aligned}$$

where $X_0$ is the point where the derivative is being evaluated.

Since this equation holds true for a vector $D$ of any magnitude, we can clearly write

$$\frac{\partial f_1}{\partial \theta}\theta_D = \frac{d}{d\epsilon}[f_1(\theta_0 + \epsilon\theta_D)]_{\epsilon=0} \qquad (7.7)$$

noting $f_1$ is a vector operation instead of a scalar one. To obtain the derivative with respect to the design vector, $p$, we perform a finite-difference on the right-hand side of Eq.(7.7), keeping in mind that $\theta_D$ is held constant (note that the finite difference formulation of the right hand side is used for evaluation).

$$q\mathbf{A}'\theta_D = \frac{\left[\frac{d}{d\epsilon}[f_1(\theta_0 + \epsilon\theta_D)]_{\epsilon=0}\right]_{p+\Delta p_i} - \left[\frac{d}{d\epsilon}[f_1(\theta_0 + \epsilon\theta_D)]_{\epsilon=0}\right]_p}{||\Delta p_i||} \qquad (7.8)$$

The number of function evaluations of $f_1$ for this calculation is equal to the number of design variables, $n_p$ (the nominal value on the right hand side of Eq.(7.8) is equal to $\mathbf{A}\theta_D$, so that evaluation does not have to be made). A finite difference calculation for $\mathbf{A}'$ would require $n_p \times n_a$ evaluations, where $n_a$ represents the number of load set nodes. Clearly, there is a substantial savings with the simplification.

The evaluation of $\mathbf{S}'F_{aD}$ follows in exactly the same manner where we write

$$\mathbf{S}'F_{aD} = \frac{\partial}{\partial p}\left(\frac{\partial f_3}{\partial F_a}\right)F_{aD} \qquad (7.9)$$

and

$$\frac{\partial f_3}{\partial F_a}F_{aD} = \frac{d}{d\epsilon}[f_3(F_{a0} + \epsilon F_{aD})]_{\epsilon=0} \qquad (7.10)$$

Once again, a finite difference of the right hand side of Eq.(7.10) (holding $F_{aD}$ constant) will yield $\mathbf{S}'F_{aD}$ with considerably less calculations.

## 7.2. The Numerical Evaluation of Sensitivity Terms

Unlike the drag sensitivity, the divergence sensitivity is analytically evaluated for several of the terms involved (Eq.(7.4)). The exceptions are the $q\mathbf{A}'\theta_D$ and $\mathbf{S}'F_{aD}$ terms which were discussed in the previous section. Therefore, we expect the accuracy of the divergence sensitivity to be entirely dependent on the approximation of these terms. The following section details the results obtained for the sensitivity and the step size considerations involved in the process.

### 7.3. *Discussion and Results*

As mentioned at the beginning of this chapter, the formulation of the divergence sensitivity is exactly the same as that of previous research. The difference in this current study is that these calculations are activated in the optimization process. For the most part, the necessary formulations were present, but no reasonable results were obtained.

Once again, the aerodynamic-structural interface will be the linear shape function approach. The problem of the cubic approach involves the evaluation of the dynamic pressure itself. Since there are only 6 load set nodes along any given chordwise direction, the interpolation of deflections and forces is highly dependent on the boundary conditions selected for the cubic splines (see chapter 5). The divergence is a value which is highly sensitive to the distribution of forces along the chord. An improper selection for the boundary will yield erroneous divergence pressures. Since it is impossible to have a *priori* knowledge of the best boundary condition, the cubic approach is very limited, and will not be used in this study.

### 7.3.1. *Calculation of* $(\partial f_1/\partial\theta)\theta_D$

If we recall Eq.(7.7),

$$\frac{\partial f_1}{\partial\theta}\theta_D = \frac{d}{d\epsilon}[f_1(\theta_0 + \epsilon\theta_D)]_{\epsilon=0} \tag{7.7}$$

a finite difference calculation is needed to evaluate the right hand side (the finite difference calculation is illustrated in Eq.(7.6)). The proper selection of $\epsilon$ is crucial to successfully approximating the directional derivative. The value of this derivative at the nominal conditions (no perturbations on the design variable vector) should be equal to $\mathbf{A}\theta_D$ as indicated in section 7.1. This knowledge provides a check on the proper selection of $\epsilon$.

The initial results of this check met with little success, no value of $\epsilon$ yielded a vector very close to $\mathbf{A}\theta_D$. This error was eventually traced to a problem with consistency. While the above derivative is evaluated at the flexible angle of attack and deformation, the divergence and $\mathbf{A}$ matrix are evaluated at the rigid wing conditions. This inconsistency was discussed in the previous chapter, but was found to have minimal impact on the drag sensitivity. Unfortunately the same cannot be said for the divergence problem. The solution was to evaluate Eq.(7.7) at the rigid wing conditions ($\alpha = \alpha_r$, $\theta_0 = \{0\}$). The optimal selection of $\epsilon$ could now proceed.

The research for the selection of $\epsilon$ was conducted by M. Rais-Rohani, with the optimal found to be 10. This may seem like an extremely large value, but close inspection of 7.7 will reveal that the step size used in the finite difference is actually $\epsilon\theta_D$. For this problem, $\theta_D$ is a vector with very small elements. Therefore, $10 \times \theta_D$ yielded the best results which agreed with $\mathbf{A}\theta_D$ to several significant figures.

### 7.3.2. Calculations for $q'_D$

All the terms remaining in Eq.(7.4) can be analytically obtained from the system of equations in 4.21, with the exception of $\mathbf{S}'F_{aD}$ which was originally formulated by P.J. Kao, and modified by M. Rais-Rohani to obtain accurate results. As with the drag sensitivity calculations, the updating of the interface transformation matrix needs to be considered. If we don't update this matrix the results given in table 7.1 are obtained (once again the complete vector of derivatives would be useful, but the cost was to prohibitive). The application of the update yields the results given in table 7.2. Clearly, the update had an extremely large impact of the accuracy, where we consider the 'correct' solution to be that which is obtained with the direct approach. This discovery is in sharp contrast to the result obtained with the drag sensitivity, where this update only marginally changed the results.

**Table 7.1.** Divergence Sensitivity Results with no Update on Interface Transformation Matrix

| Variable | Direct (Pa/m) | Eq.(7.4) (Pa/m) | $|\text{Error}(q'_D)|$ |
|:---:|:---:|:---:|:---:|
| 1 | $-6.640 \times 10^3$ | $-6.295 \times 10^3$ | 5.2% |
| 2 | $2.993 \times 10^4$ | $5.234 \times 10^4$ | 74.9% |
| 3 | $2.212 \times 10^4$ | $5.389 \times 10^4$ | 143.6% |
| 4 | $8.340 \times 10^3$ | $7.002 \times 10^3$ | 16.0% |
| 5 | $-1.549 \times 10^4$ | $-2.934 \times 10^4$ | 84.1% |
| 6 | $-9.942 \times 10^5$ | $-7.144 \times 10^5$ | 28.1% |
| 7* | $-2.642 \times 10^5$ | $-2.987 \times 10^5$ | 13.0% |
| 8* | $-2.736 \times 10^5$ | $-2.819 \times 10^5$ | 3.0% |
| * Derivatives are per radian | | | |


**Table 7.2.** Divergence Sensitivity Results with Updated Interface Transformation Matrix

| Variable | Direct (Pa/m) | Eq.(7.4) (Pa/m) | $|\text{Error}(q'_D)|$ |
|:---:|:---:|:---:|:---:|
| 1 | $-6.640 \times 10^3$ | $-6.818 \times 10^3$ | 2.7% |
| 2 | $2.993 \times 10^4$ | $2.851 \times 10^4$ | 4.8% |
| 3 | $2.212 \times 10^4$ | $2.129 \times 10^4$ | 3.8% |
| 4 | $8.340 \times 10^3$ | $7.308 \times 10^3$ | 12.4% |
| 5 | $-1.549 \times 10^4$ | $-1.618 \times 10^4$ | 4.4% |
| 6 | $-9.942 \times 10^5$ | $-1.021 \times 10^6$ | 2.6% |
| 7* | $-2.642 \times 10^5$ | $-2.987 \times 10^5$ | 13.0% |
| 8* | $-2.736 \times 10^5$ | $-2.819 \times 10^5$ | 3.0% |
| * Derivatives are per radian | | | |

The accuracy of the results are comparable to those obtained in the drag calculations, with the largest error occurring in the break span and twist terms. Initially, one might expect a greater accuracy because of the small number of finite difference calculations involved. However, offsetting this reduced number of approximations, is the fact that the terms $\mathbf{A}'\boldsymbol{\theta}_D$ and $\mathbf{S}'F_{aD}$ are essentially second derivatives, and the

nested forward differences have errors which build up. In any event, the accuracy obtained is suitable for the optimization problem.

An additional analysis involved selecting the step size in $p$ for the $\mathbf{A}'\boldsymbol{\theta}_D$ calculation. Tables 7.3–7.5 represent step sizes for $\Delta p_i$ of $1 \times 10^{-3}$m and $1 \times 10^{-4}$m respectively. Since there is little variation in the result with these changes, the value was left at $1 \times 10^{-2}$m.

**Table 7.3.** Divergence Sensitivity Results with $\Delta p_i = 1 \times 10^{-3}$m

| Variable | Direct (Pa/m) | Eq.(7.4) (Pa/m) | $|\text{Error}(q'_D)|$ |
|----------|---------------|-----------------|------------------------|
| 1 | $-6.640 \times 10^3$ | $-6.817 \times 10^3$ | 2.7% |
| 2 | $2.993 \times 10^4$ | $2.850 \times 10^4$ | 4.8% |
| 3 | $2.212 \times 10^4$ | $2.130 \times 10^4$ | 3.7% |
| 4 | $8.340 \times 10^3$ | $7.308 \times 10^3$ | 12.4% |
| 5 | $-1.549 \times 10^4$ | $-1.618 \times 10^4$ | 4.5% |
| 6 | $-9.942 \times 10^5$ | $-1.081 \times 10^6$ | 8.8% |
| 7* | $-2.642 \times 10^5$ | $-2.941 \times 10^5$ | 11.3% |
| 8* | $-2.736 \times 10^5$ | $-2.814 \times 10^5$ | 2.8% |
| * Derivatives are per radian | | | |

**Table 7.4.** Divergence Sensitivity Results with $\Delta p_i = 1 \times 10^{-4}$m

| Variable | Direct (Pa/m) | Eq.(7.4) (Pa/m) | $|\text{Error}(q'_D)|$ |
|----------|---------------|-----------------|------------------------|
| 1 | $-6.640 \times 10^3$ | $-6.817 \times 10^3$ | 2.7% |
| 2 | $2.993 \times 10^4$ | $2.850 \times 10^4$ | 4.8% |
| 3 | $2.212 \times 10^4$ | $2.130 \times 10^4$ | 3.7% |
| 4 | $8.340 \times 10^3$ | $7.308 \times 10^3$ | 12.4% |
| 5 | $-1.549 \times 10^4$ | $-1.618 \times 10^4$ | 4.5% |
| 6 | $-9.942 \times 10^5$ | $-1.081 \times 10^6$ | 8.8% |
| 7* | $-2.642 \times 10^5$ | $-2.937 \times 10^5$ | 11.2% |
| 8* | $-2.736 \times 10^5$ | $-2.813 \times 10^5$ | 2.8% |
| * Derivatives are per radian | | | |

Finally, the impact of using the flexible wing conditions in the calculation of $\mathbf{A}'\theta_D$ is given in table 7.5. This selection results in sever errors in several terms, which clearly demonstrates the importance of using the rigid wing conditions.

**Table 7.5.** Divergence Sensitivity Results at Flexible Wing Conditions

| Variable | Direct (Pa/m) | Eq.(7.4) (Pa/m) | $\vert\mathbf{Error}(q_D')\vert$ |
|:---:|:---:|:---:|:---:|
| 1 | $-6.640\times10^3$ | $-6.568\times10^3$ | 1.1% |
| 2 | $2.993\times10^4$ | $1.286\times10^4$ | 57.0% |
| 3 | $2.212\times10^4$ | $-2.550\times10^4$ | 215.3% |
| 4 | $8.340\times10^3$ | $7.350\times10^3$ | 11.9% |
| 5 | $-1.549\times10^4$ | $-4.614\times10^3$ | 70.2% |
| 6 | $-9.942\times10^5$ | $-1.190\times10^6$ | 19.7% |
| 7* | $-2.642\times10^5$ | $-5.023\times10^5$ | 90.1% |
| 8* | $-2.736\times10^5$ | $-4.090\times10^5$ | 49.5% |
| * Derivatives are per radian | | | |

### 7.4. Conclusions for the Divergence Sensitivity

In the final analysis, an acceptable accuracy for the divergence sensitivity can be obtained providing the rigid wing conditions are used and the interface transformation matrix is updated as the planform of the wing is perturbed. Figure 7.1 gives the exact divergence dynamic pressure verses the approximation over the variation of design variables given in table 6.1. Clearly the approximation is tangent to the exact at the initial point, but the variation in the design parameters is too great, which make a linear approximation inadequate for such a large neighborhood. This problem could be corrected by not allowing the design parameters to change to such a degree. This limiting will be discussed in the following chapter on the approximate optimization.
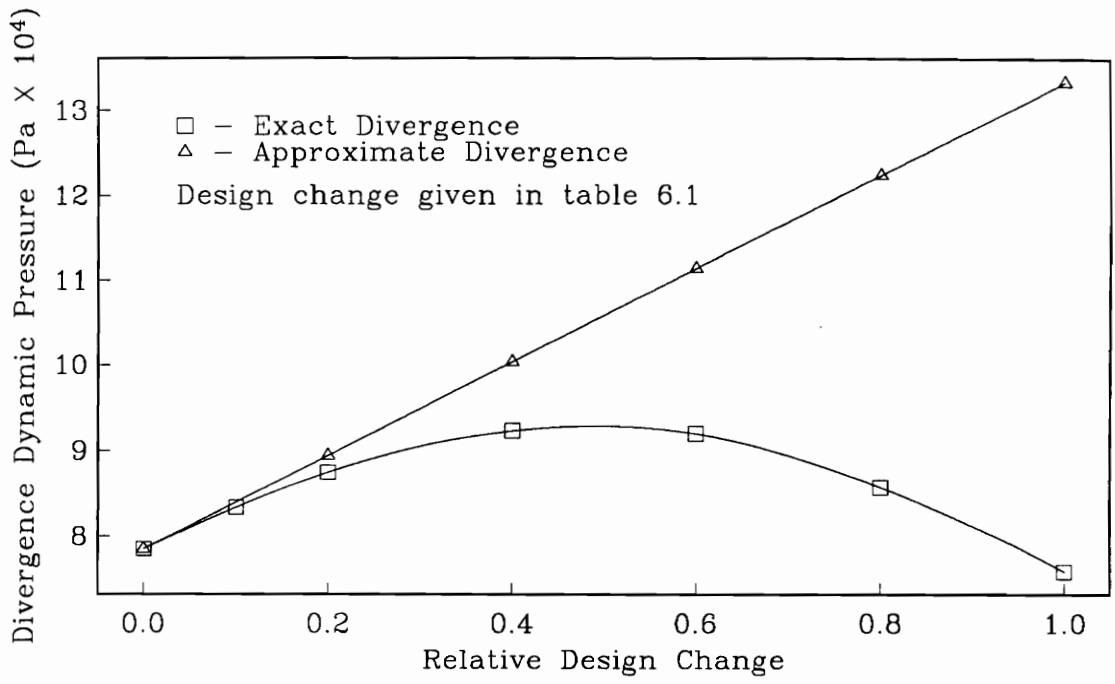
**Figure 7.1.** Exact and Approximate Divergence Dynamic Pressure

# 8.  THE OPTIMIZATION PROCEDURE AND RESULTS

## 8.0. Introduction

The final and most important aspect of the design procedure is the approximate optimization process and results. At this point, all the effects of the changes to the models and sensitivity calculations will come into play. Obviously the change to the drag model will have a negative impact on the range constraint (due to the increased drag). The inclusion of the divergence constraint may also have an effect on the final design if that constraint becomes critical at any time during the design cycles. It is expected that this analysis will be quite difference from previous research due to these changes. Furthermore, it is hoped that the increased accuracy in the sensitivities will make the optimization a smoother process.

## 8.1. The Optimization Formulation

As with any optimization procedure, the goal in this research is to minimize some objective function subject to a set of constraints. Chapter 2 detailed the objective function and constraints of interest for the wing design problem being considered. With these in mind, it is possible to formulate the optimization as:[6]

$$
\begin{aligned}
\text{minimize} \quad & W(p) \\
\text{such that} \quad & g_s(p) \geq 0 \\
& V_s(p) \geq V_r \\
& R_c(p, D) \geq R_r \\
& q_D(p) \geq 1.44 \times q_m
\end{aligned}
\tag{8.1}
$$

where $g_s$ is a vector of functions which represent the structural constraints. The values $V_s$ and $V_r$ represent the available and required wing volume respectively

(needed for fuel storage). The terms $R_c$ and $R_r$, represent the calculated and required aircraft range as discussed in Chapter 2. The final terms $q_D$ and $q_m$ represent the calculated divergence dynamic pressure and the maneuver dynamic pressure respectively.

An exact analysis of the constrained optimization problem given above would result in a monumental computational problem with prohibitive computational costs.* The solution to this problem is to follow Ref. 6 and perform sequential approximate optimizations, where each of the constraints is linearized at some initial condition, and assumed to be accurate in some small neighborhood near that point, $p^0$. This small neighborhood is defined by move limits given for each design variable such that:

$$p_i = p_i^0 \pm \delta_i \tag{8.2}$$

where $\delta_i$ is the move limit for variable $i$. Very small move limits will give the approximations the highest accuracy, but will dramatically slow the convergence.

Each approximate optimization can be written as:[6]

$$
\begin{aligned}
\text{minimize} \quad & W(p) \\
\text{such that} \quad & g_s(p^0) + \sum_{i=1}^{n_p} \frac{\partial g_s}{\partial p_i} \Delta p_i \geq 0 \\
& V_s(p) \geq V_r \\
& R_c(p, D) \geq R_r \\
& q_D(p^0) + \sum_{i=1}^{n_p} \frac{\partial q_D}{\partial p_i} \Delta p_i \geq 1.44 \times q_m \\
\text{where} \quad & D = D(p^0) + \sum_{i=1}^{n_p} \frac{\partial D}{\partial p_i} \Delta p_i
\end{aligned} \tag{8.3}
$$

where $n_p$ represents the number of design variables and $\Delta p_i$ represents the change in the $i^{th}$ design variable. Note that the range is calculated directly from the

---

\* An exact analysis is possible with a much smaller design problem (e.g. Ref. 1).

drag approximation instead of being linearized itself. Also note that while the linear approximations to the structural stresses and strains were never specifically addressed in this study, the methods used for their calculation are similar to that of the other sensitivities.

During each of these approximate optimization cycles, the objective function and associated constraints are analyzed with the NEWSUMT-A program[21]. This code employs an extended interior penalty function procedure to find the minimum aircraft weight subject to the approximate constraints and the allowed move limits for the design variables. Once this optimum is found, the new design point becomes the initial point, $p^0$, for a new cycle. Note that at the beginning of each cycle, the aeroelastic and sensitivity analysis is performed to find the appropriate linearization for the new cycle. This procedure is continued until global convergence is obtained (Figs. 8.1–8.3 illustrate this process and outline the sensitivity calculations).

*8.2. The Initial Design Point*

At the beginning of an optimization process it is necessary to select the initial set of design variables. While the performance and structural design variables were changed in each of the optimization runs made, the initial planform of the wing was the same for all cases (Table 8.1).*

**Table 8.1.** The Initial Planform Variables

| $p_1$: Root Chord(m) | 6.916 | $p_5$: Tip Span(m) | 12.250 |
|---|---|---|---|
| $p_2$: Break Chord(m) | 3.765 | $p_6$: Sweep(deg) | 26.070 |
| $p_3$: Tip Chord(m) | 1.725 | $p_7$: Break Twist(deg) | 0.000 |
| $p_4$: Break Span(m) | 5.754 | $p_8$: Tip Twist(deg) | 0.000 |

---

* The initial point in this context is the value of the design variable vector at the start of the first approximate optimization cycle.
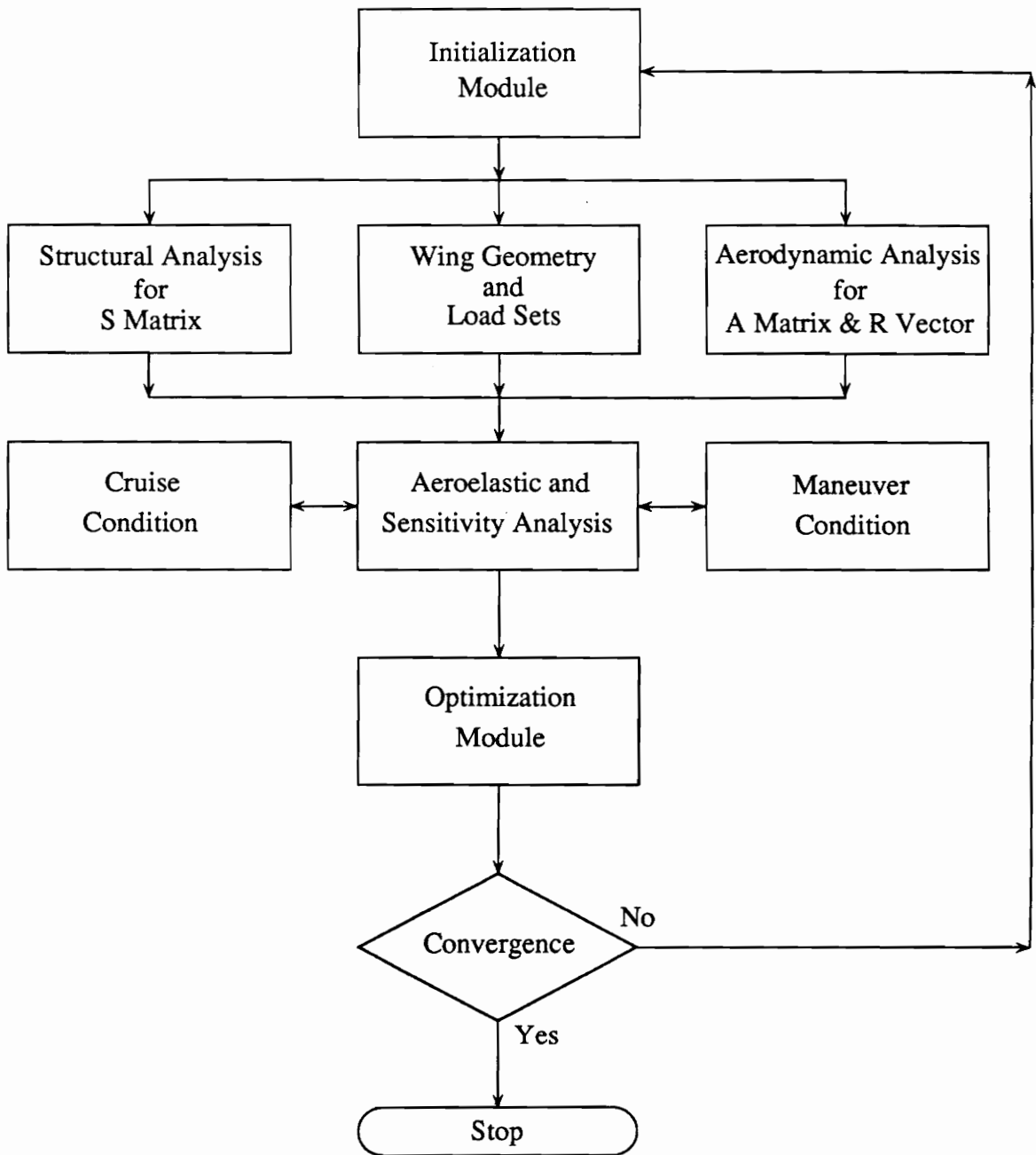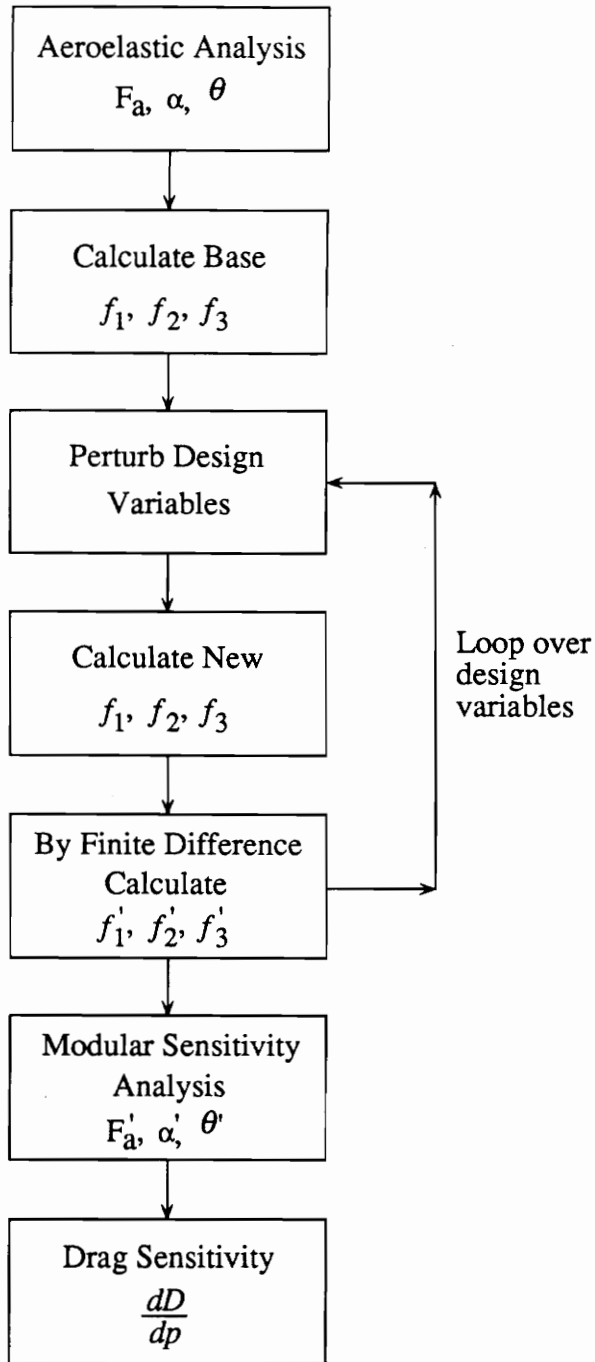
**Figure 8.1.** The Design Process [4]

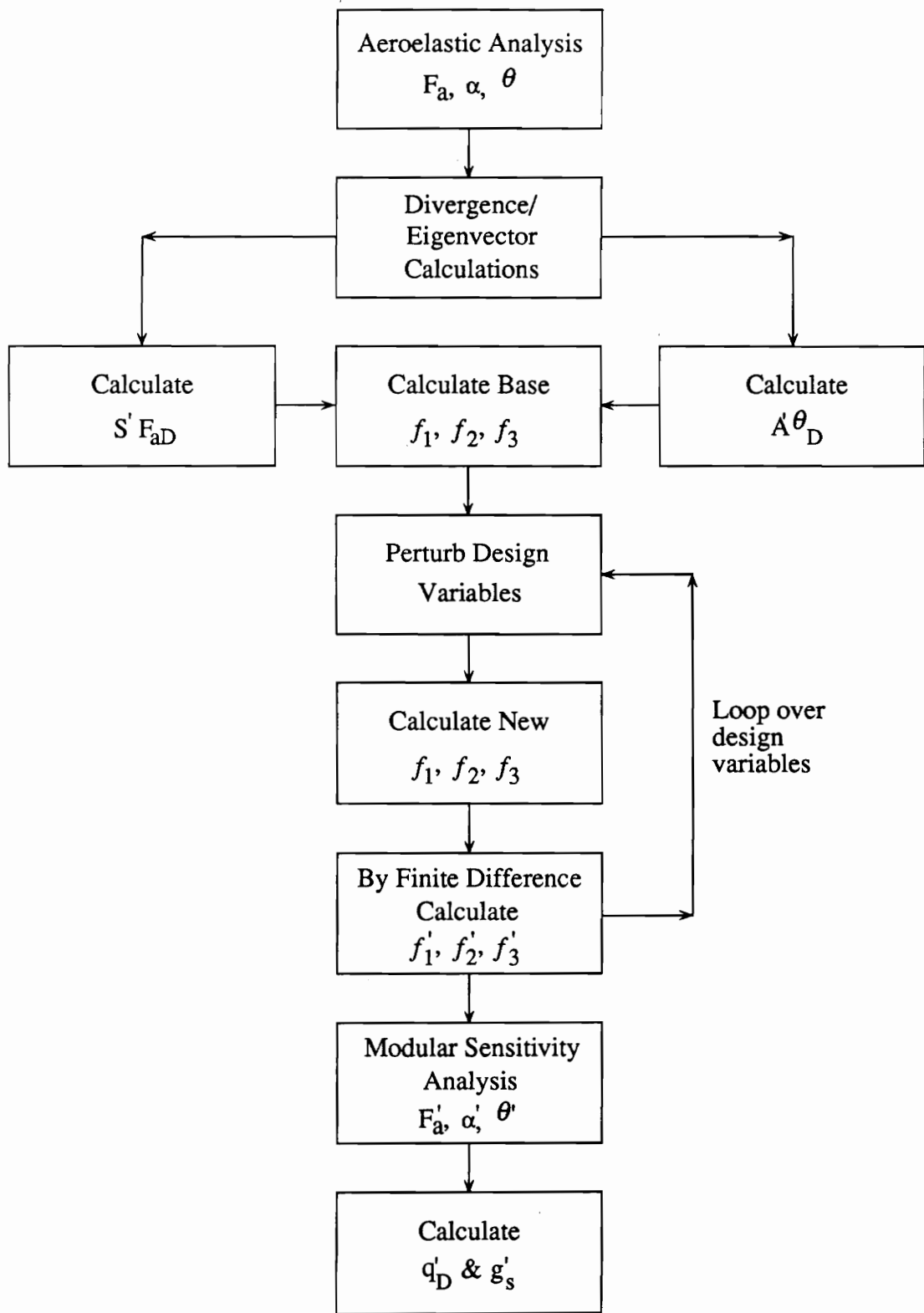**Figure 8.2.** Aeroelastic Sensitivity Analysis for Cruise [4]

**Figure 8.3.** Aeroelastic Sensitivity Analysis for Maneuver [4]

## 8.3. Results and Discussion

As a first attempt at a full optimization, the structural design variables were set at the values used in previous research by P.J. Kao[5] and D. Polen.[4] The dynamic pressure was set at 2674 Pa. and the usable fuel was set at 21902 N which were also used in the past. The move limits for the aerodynamic and performance design variables were set at 4% while the structural variables had very large limits. The large move limits on the structural variables were justified by the belief that the linearization associated with these terms was highly accurate. Table 8.2 gives some pertinent optimization results for seven cycles.

**Table 8.2.** Optimization Results for First Run

| Beg. of Cycle | Move Limits A & P | Str. | Range Margin | No. of Violated Constraints | Most Violated Str. Constraint | |
|---|---|---|---|---|---|---|
| 1 | 4.0% | ∞ | -36.38% | 23 | #47 | 22.12% |
| 2 | 4.0% | ∞ | -22.46% | 31 | #36 | 12.81% |
| 3 | 4.0% | ∞ | -14.94% | 31 | #36 | 12.13% |
| 4 | 4.0% | ∞ | -9.20% | 34 | #47 | 13.81% |
| 5 | 4.0% | ∞ | -4.36% | 40 | #3 | 12.06% |
| 6 | 4.0% | ∞ | -1.58% | 59 | #47 | 20.06% |
| 7 | 4.0% | ∞ | -0.73% | 76 | #47 | 29.76% |

A quick inspection of the above results reveals that the initial design violates a considerable number of constraints. While the optimizer will attempt to satisfy all of the constraints, it is clear that it could not. In fact, both the number of violations and the magnitude of the greatest violation, steadily increased. One possibility for this error, was the excessive move limits for the structural variables. If we recall Fig. 7.1 we saw that the approximation of the divergence dynamic pressure was tangent, but that the exact response was very non-linear in the chosen domain.

This non-linearity may have the same adverse effects on the structural constraint approximations. To investigate this theory, another run with move limits of 15.0% on the structural variables was made. Under these new conditions, it was quickly apparent that the reduced move limits were not sufficient to correct the error. However, it should be noted that the optimization was able to accurately approximate the range, as indicated by the steadily decreasing violation for that term. This accuracy is an excellent indication that the drag approximation is functioning properly. Unfortunately, the divergence constraint never became critical during this entire study. Therefore a similar check could never be made on divergence, but there is no reason to believe the approximation would be inaccurate.

Another possibility for the problem was found by consulting R.T. Haftka who indicated that NEWSUMT-A does not perform very well when an initial condition violates a large number of constraints. A suggestion was made to thicken the structural members and increase the initial fuel and dynamic pressure until most of the violations were alleviated. Table 8.3 give the results for five design cycles with the significantly reduced violations.

**Table 8.3.** Optimization Results for Second Run

| Beg. of Cycle | Move Limits A & P  Str. | Range Margin | No. of Violated Constraints | Most Violated Str.  Constraint |
|---|---|---|---|---|
| 1 | 4.0%  15.0% | -0.25% | 2 | #47    1.79% |
| 2 | 4.0%  15.0% | -0.05% | 2 | #47    6.25% |
| 3 | 4.0%  15.0% | -0.07% | 7 | #47    9.76% |
| 4 | 4.0%  15.0% | -0.06% | 12 | #47    12.36% |
| 5 | 4.0%  15.0% | -0.13% | 19 | #47    14.08% |

Unfortunately, it is clear that the reduced move limits and improved initial conditions, still could not eliminate the violation growth. It was felt that the only

remaining possibility for success, would lie in a further reduction of move limits. A run was made with all the limits set at 4%, and violation growth was again encountered. The next attempt set all the aerodynamic and performance move limits to 3%, and cycled the structural limits between 3% and 7%. Under these conditions, the violation growth was contained and a successful run resulted. The output for this run is given in table 8.4.

**Table 8.4.** Optimization Results for Third Run

| Beg. of Cycle | Move Limits A & P   Str. | | Range Margin | No. of Violated Constraints | Most Violated Str. Constraint | |
|---|---|---|---|---|---|---|
| 1  | 3.0% | 3.0% | -0.25% | 2 | #47 | 1.79% |
| 2  | 3.0% | 3.0% | 0.84%  | 1 | #47 | 1.86% |
| 3  | 3.0% | 7.0% | -0.10% | 2 | #47 | 4.66% |
| 4  | 3.0% | 7.0% | 0.69%  | 1 | #47 | 2.43% |
| 5  | 3.0% | 3.0% | 0.91%  | 1 | #47 | 1.74% |
| 6  | 3.0% | 3.0% | -0.07% | 6 | #47 | 6.10% |
| 7  | 3.0% | 7.0% | 0.70%  | 2 | #3  | 1.12% |
| 8  | 3.0% | 7.0% | 0.92%  | 1 | #3  | 1.63% |
| 9  | 3.0% | 3.0% | 0.95%  | 1 | #3  | 1.97% |
| 10 | 3.0% | 3.0% | 0.88%  | 2 | #3  | 1.19% |
| 11 | 3.0% | 7.0% | 0.87%  | 2 | #3  | 0.72% |
| 12 | 3.0% | 7.0% | 0.86%  | 2 | #3  | 0.64% |

While this last attempt did yield a usable result after 12 cycles*, the design was interesting but not necessarily of practical importance (See Figs. 8.4–8.13 for plots of the convergence history of various terms). The problem is that the optimizer increases the amount of usuable fuel (see Fig. 8.6). While this is not an optimization problem, it does mean that the final design will compromise some fuel economy, which is generally not desirable. For the most part, this increase in fuel is

---

\* The optimization could have been continued, but it was felt that sufficient cycles had been run to demonstrate the success.

economy, which is generally not desirable. For the most part, this increase in fuel is due to a slight increase in the flexible wing drag (see Fig. 8.7). The rise in drag is a result of a complex interaction of wing geometry and the dynamic pressure (Fig. 8.10). In any case, the additional weight of the extra fuel is more than offset by the concurrent savings in structural weight, especially in the wing (Fig. 8.5). Most of these structural saving come from the reduction in wing area (Fig. 8.8).

Other effects which reduce structural weight include the application of a negative twist distribution which places more of the wing loading near the root, and the reduction of aspect ratio. Each of these approaches increase drag, but reduce structural weight by lowering the bending moment at the root. Again, the increased fuel weight is offset by the structural savings.

This initial investigation was successful in terms of the optimization process, but produced unexpected results. What was desired was a more efficient wing, with an increase in aspect ratio, a decrease in wing area, and a removal of the majority of the sweep (because of the subsonic cruise). Since NEWSUMT-A never encountered a range problem, there was no need to optimize the wing for drag considerations. An intelligent approach to a fourth optimization run, would be to add an additional constraint which maximizes the amount of usable fuel. This new design should force the creation of a more efficient wing, because drag increases could no longer be offset by an increase in fuel. The end result would be a more practical design that accounts for some fuel economy. The selection of this maximum, will greatly effect the final design. The more frugal the selection, the more efficient the final wing will be. This efficiency will be at the cost of some weight reduction, because the higher stresses found in high aspect ratio wings necessitate stronger wing members.
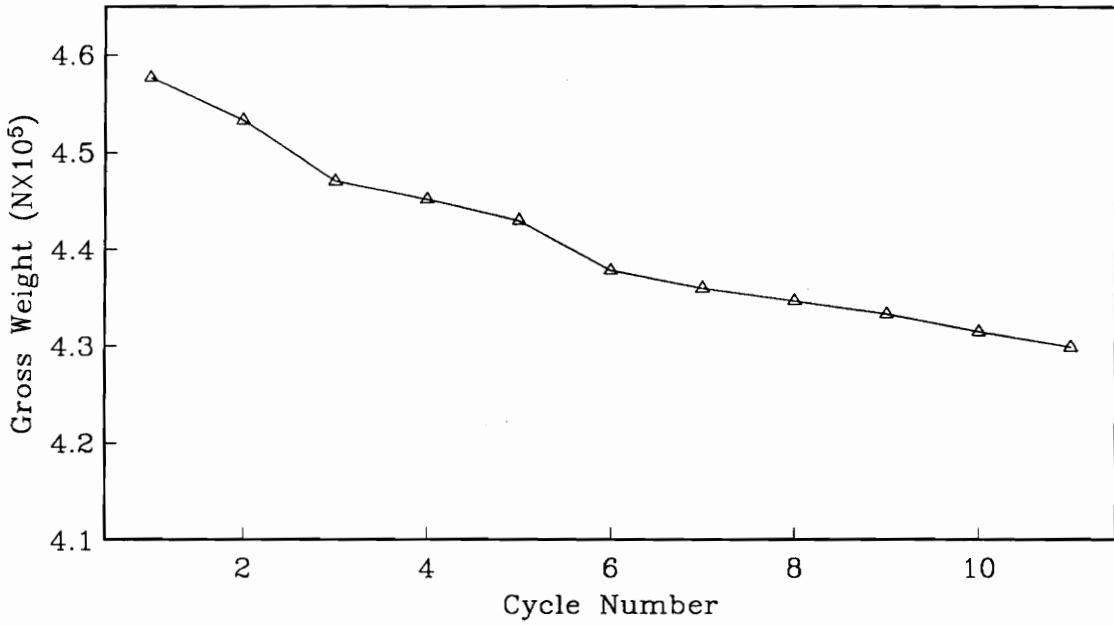
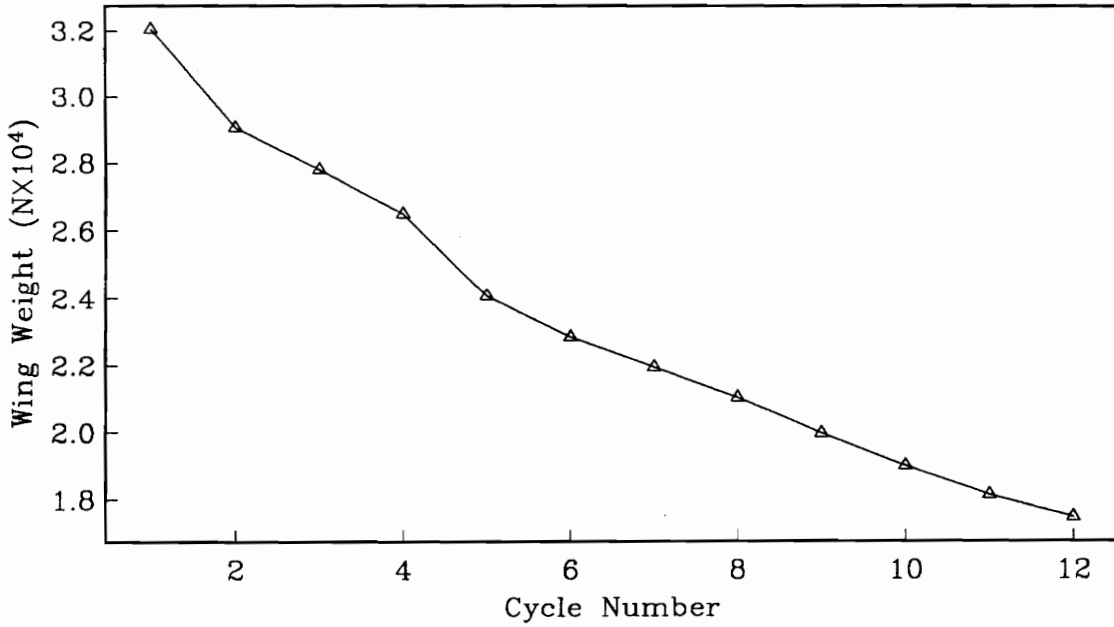**Figure 8.4.** Aircraft Gross Weight vs. Cycle Number for Third Run



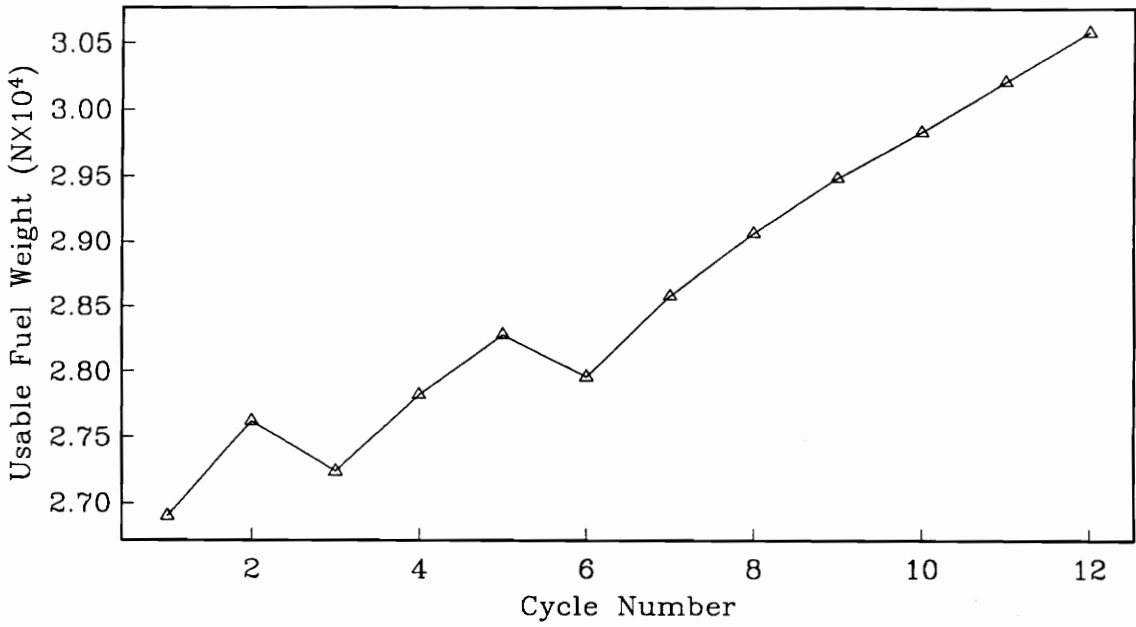**Figure 8.5.** Wing Weight vs. Cycle Number for Third Run

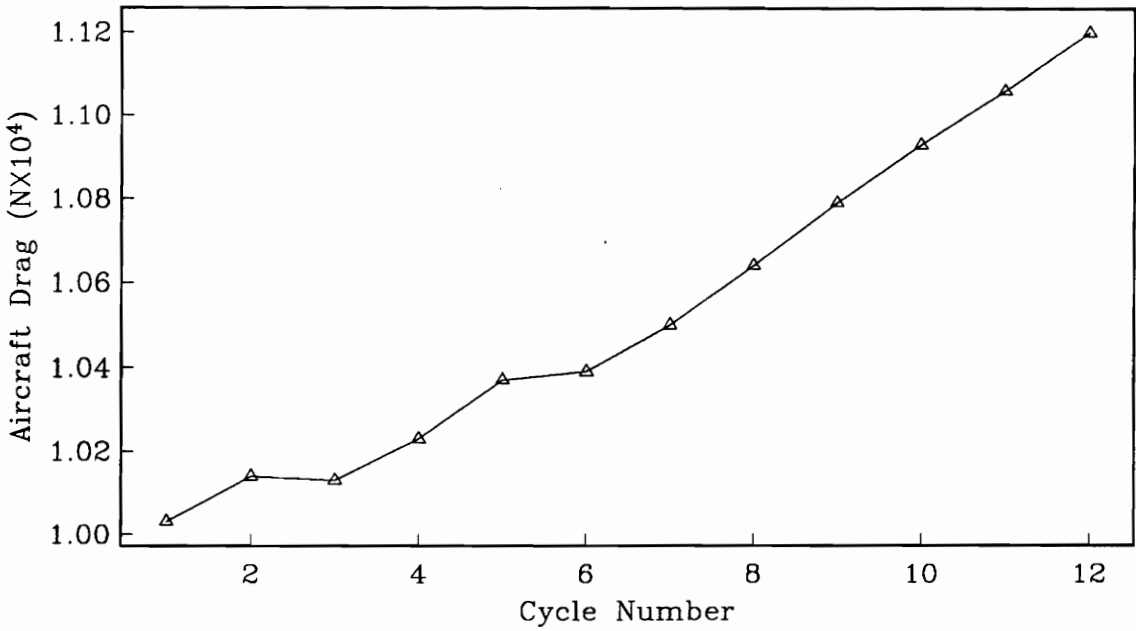**Figure 8.6.** Usable Fuel Weight vs. Cycle Number for Third Run



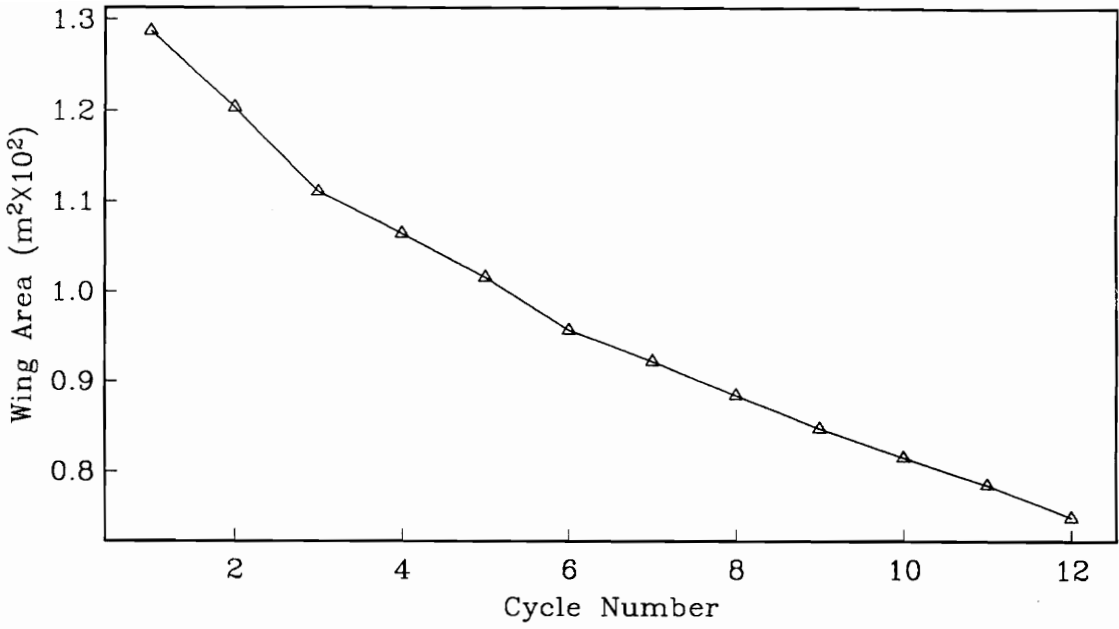**Figure 8.7.** Flexible Wing Drag vs. Cycle Number for Third Run

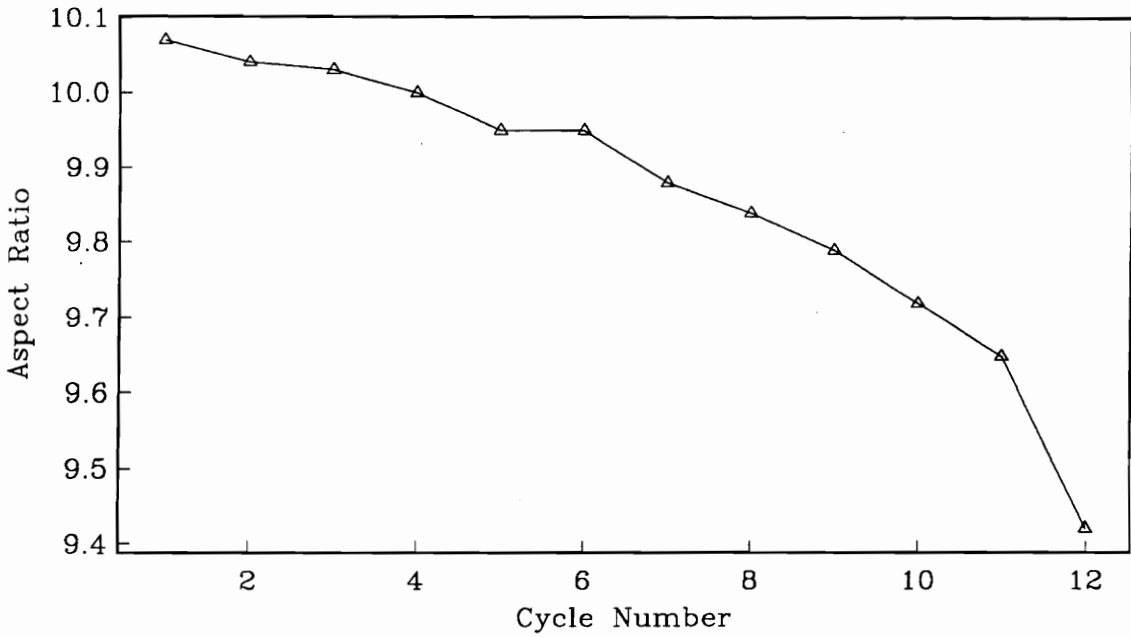**Figure 8.8.** Total Wing Area vs. Cycle Number for Third Run



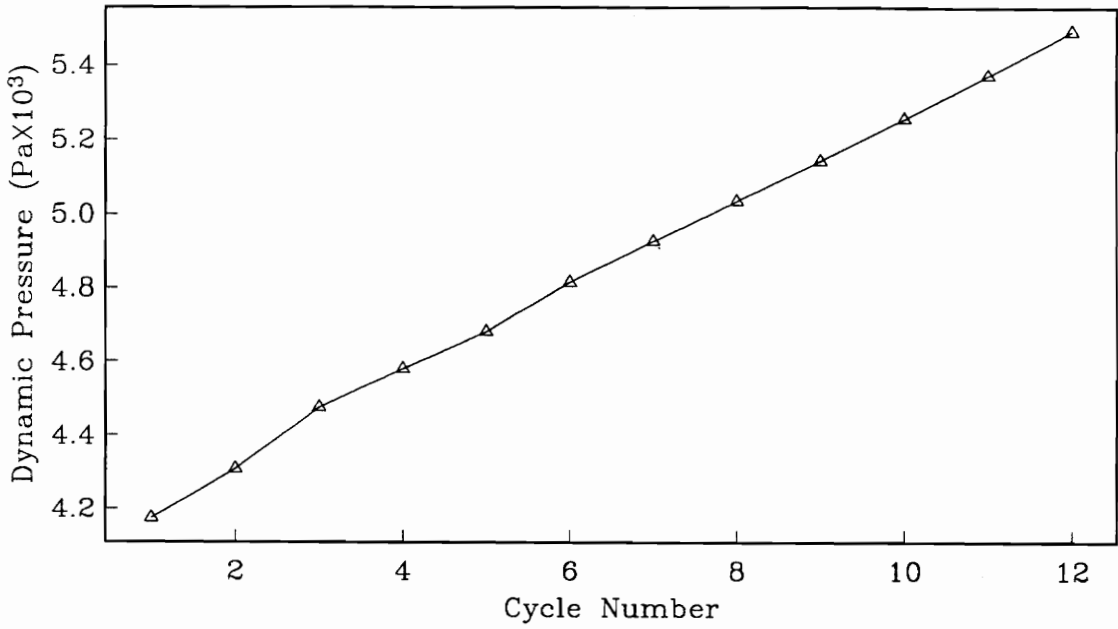**Figure 8.9.** Aspect Ratio vs. Cycle Number for Third Run

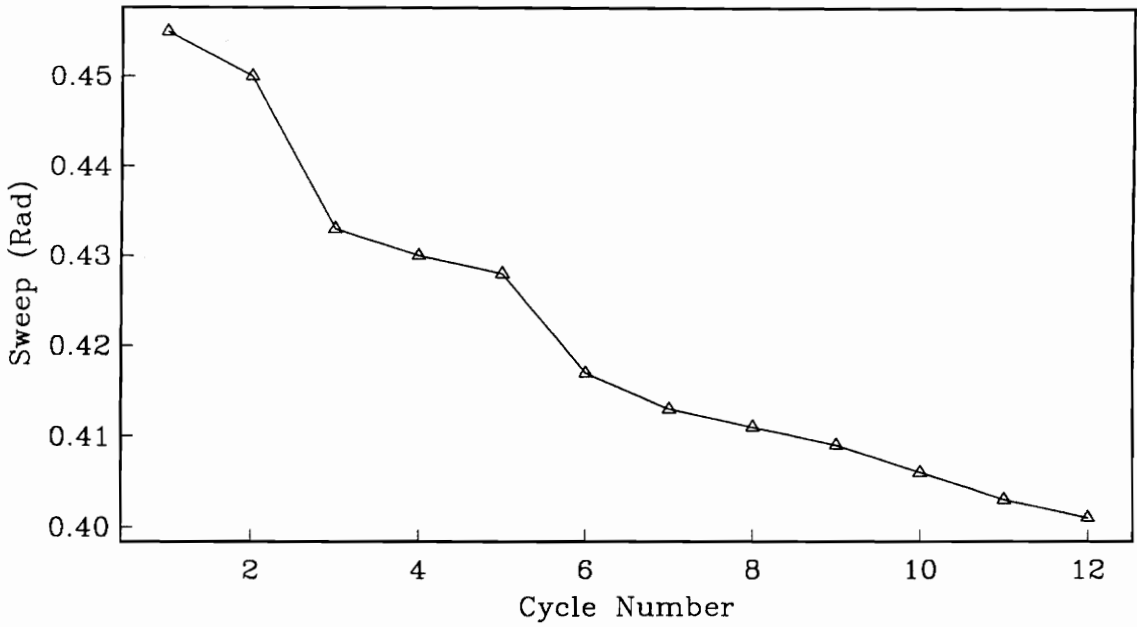**Figure 8.10.** Cruise Dynamic Pressure vs. Cycle Number for Third Run



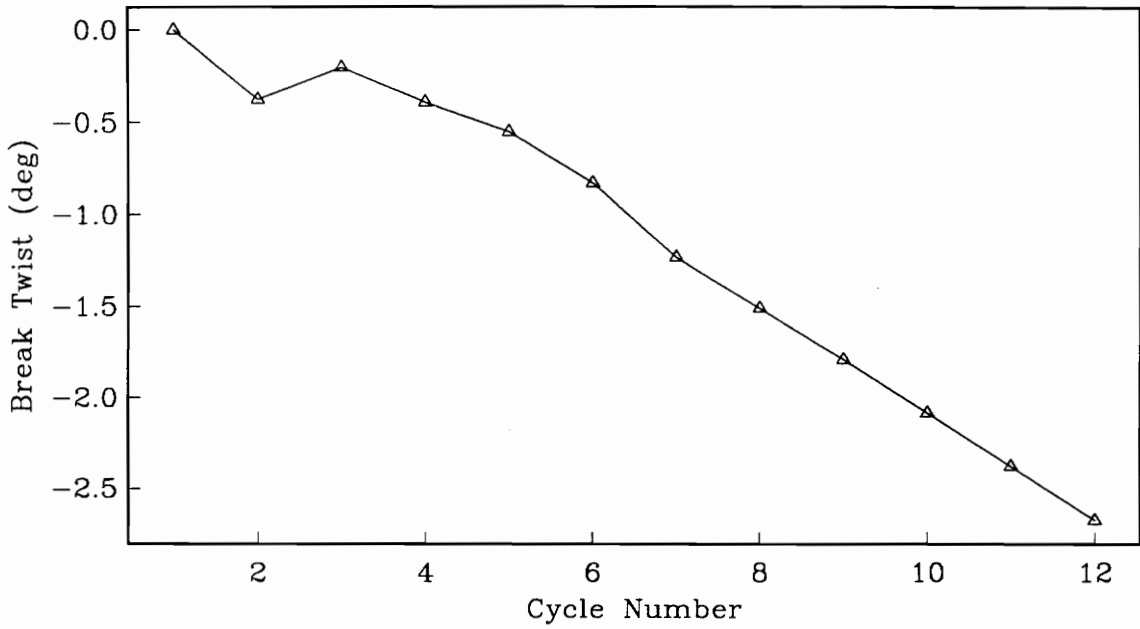**Figure 8.11.** Sweep at Break vs. Cycle Number for Third Run

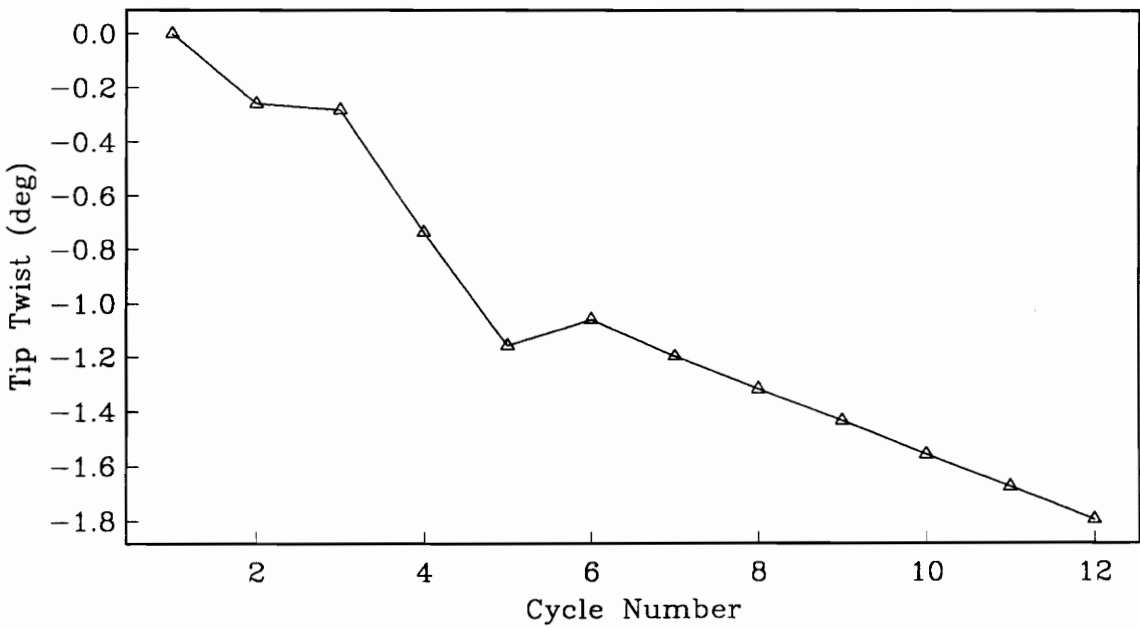**Figure 8.12.** Break Twist (Jig) vs. Cycle Number for Third Run



**Figure 8.13.** Tip Twist (Jig) vs. Cycle Number for Third Run

An attempt with this new constraint was made by selecting the usable fuel maximum to be the initial allotment. Since the design code is not set up for this additional constraint, the maximum fuel amount is maintained by restricting the appropriate move limit. This approach works well providing the range constraint is never violated to any great degree. Therefore, this initial allotment is just enough to complete the mission at the initial set of design variables. Another constraint added to this run involves the dynamic pressure. Since the velocity of the cruise portion of the flight is fixed at 142 m·s$^{-1}$, the dynamic pressure defines the altitude at which the aircraft will fly. Since it was felt that flight below 20k feet was unrealistic, the dynamic pressure was limited to 6553 Pa. If a more sophisticated engine performance model is utilized in the future, this constraint should not be necessary because of substantial fuel consumption penalties at low altitude (the current model holds the specific fuel consumption constant with altitude). Table 8.5 gives the optimization results for this new run.

Figures 8.14–8.23 give the optimization history for several variables during this new run. It is immediately apparent the the behavior of the drag, usable fuel, and aspect ratio is markedly different than the run made with no fuel limit. The drag and usable fuel stayed essentially constant (Figs. 8.16 and 8.17), while the aspect ratio increased to offset the drag rise due to the negative twist distribution (Figs. 8.19 and 8.22–8.23 respectively). These figures also indicate that the dynamic pressure constraint became active at about the 18$^{th}$ design cycle (see Fig. 8.20). Furthermore, it is apparent that the range constraint is slightly more critical than in the previous run, and that this constraint remained active throughout the design optimization.

Of concern during this run was the previously mentioned twist distribution, and the drastic decrease of wing area (see Fig. 8.18). These two factors combined to

produce large angles of attack at the wing root, which makes stall an issue. Since the Vortex Lattice Model cannot model stall, additional constraints need to be implemented to avoid invalidating the aerodynamic model. These new constraints were imposed on the break and tip twists at the $17^{th}$ design cycle. The best approach to this problem is to apply a constraint directly to the local $C_l$'s at the root, break, and tip respectively. But as previously mentioned, no allowance for such a constraint was made in the design code. This approach will be used in the future, but it is beyond the scope of this current study. As expected, the twist limitations were only partially effective in limiting the root angle of attack. At the final design, the root angle of attack was 13° which is the the the stall regime for the airfoil. However, this is not considered a major concern because the basic mechanics of the design process were still effective. Furthermore, it would be a simple task to locate an airfoil which could maintain such a high angle of attach without stall.

This fourth and final optimization run was concluded on the $27^{th}$ cycle were it was felt that total weight of the aircraft was sufficiently converged (see Fig. 8.14). At this point, the area of the wing clearly converged to a value of 63.2 m², and the aspect ratio roughly converged to 11.7. The sweep of the wing was still decreasing at this point, but it did show signs of an eventual leveling off. If the design was continued beyond this point, the sweep would most likely have finally converged to some very low value which is what we expect. However, the savings in total weight with a continuation in the design would be minimal. Furthermore, a continuation would have even further reduced the wing area (slightly), which would have further aggravated the root angle of attack.

**Table 8.5.** Optimization Results for Fourth Run

| Beg. of Cycle | Move Limits A & P | Str. | Range Margin | No. of Violated Constraints | Most Violated Str. | Constraint |
|---|---|---|---|---|---|---|
| 1 | 3.0% | 3.0% | 0.98% | 0 | NA | NA |
| 2 | 3.0% | 3.0% | 0.48% | 0 | NA | NA |
| 3 | 3.0% | 3.0% | 0.49% | 0 | NA | NA |
| 4 | 3.0% | 3.0% | 0.50% | 0 | NA | NA |
| 5 | 3.0% | 5.0% | 0.51% | 1 | #47 | 0.10% |
| 6 | 3.0% | 5.0% | 0.46% | 1 | #47 | 0.57% |
| 7 | 3.0% | 5.0% | 0.44% | 2 | #3 | 0.81% |
| 8 | 4.0% | 5.0% | 0.42% | 2 | #3 | 1.40% |
| 9 | 4.0% | 5.0% | -0.12% | 5 | #3 | 7.43% |
| 10 | 3.0% | 3.0% | 0.21% | 3 | #3 | 4.32% |
| 11 | 3.0% | 3.0% | 0.10% | 2 | #3 | 4.19% |
| 12 | 3.0% | 3.0% | 0.10% | 2 | #3 | 4.21% |
| 13 | 3.0% | 3.0% | 0.28% | 3 | #3 | 5.21% |
| 14 | 3.0% | 3.0% | -0.18% | 4 | #3 | 5.19% |
| 15 | 3.0% | 3.0% | -0.18% | 4 | #47 | 4.91% |
| 16 | 3.0% | 3.0% | -0.24% | 3 | #3 | 1.90% |
| 17 | 3.0% | 3.0% | -0.32% | 3 | #3 | 1.77% |
| 18 | 3.0% | 3.0% | -0.19% | 4 | #3 | 3.31% |
| 19 | 3.0% | 3.0% | -0.41% | 7 | #3 | 2.74% |
| 20 | 3.0% | 3.0% | -0.05% | 6 | #36 | 1.84% |
| 21 | 3.0% | 3.0% | -0.07% | 16 | #36 | 9.58% |
| 22 | 3.0% | 3.0% | -0.06% | 7 | #37 | 1.18% |
| 23 | 3.0% | 3.0% | -0.11% | 12 | #161 | 4.36% |
| 24 | 1.5% | 1.5% | 0.81% | 15 | #119 | 7.33% |
| 25 | 1.5% | 1.5% | -0.15% | 10 | #161 | 3.53% |
| 26 | 1.5% | 1.5% | -0.09% | 9 | #47 | 2.50% |
| 27 | 1.5% | 1.5% | -0.10% | 8 | #47 | 0.99% |
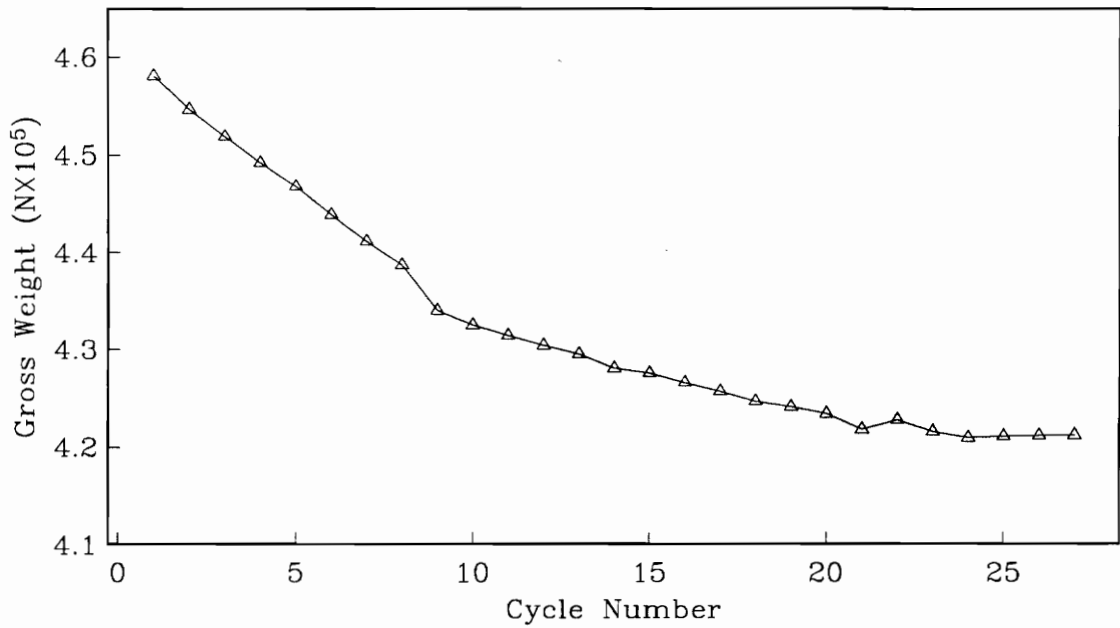
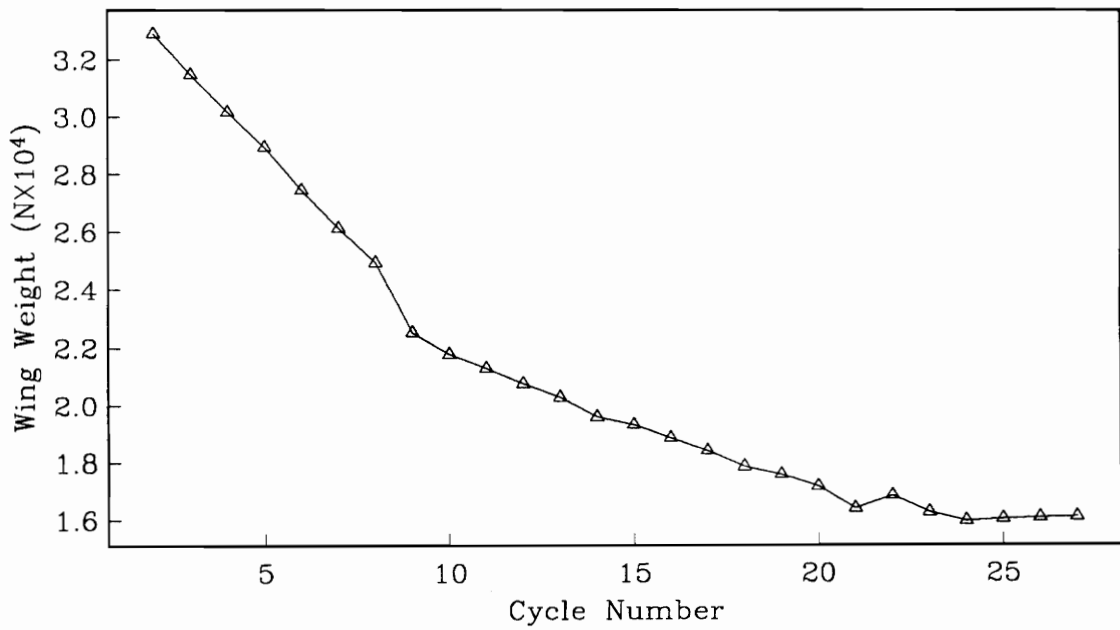**Figure 8.14.** Aircraft Gross Weight vs. Cycle Number for Fourth Run



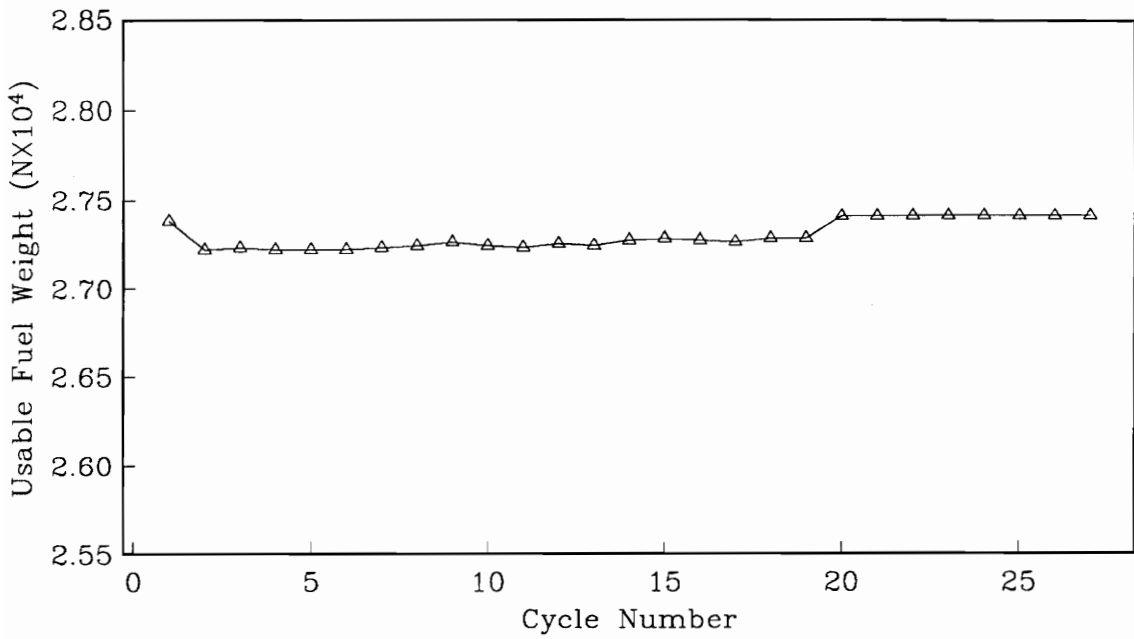**Figure 8.15.** Wing Weight vs. Cycle Number for Fourth Run

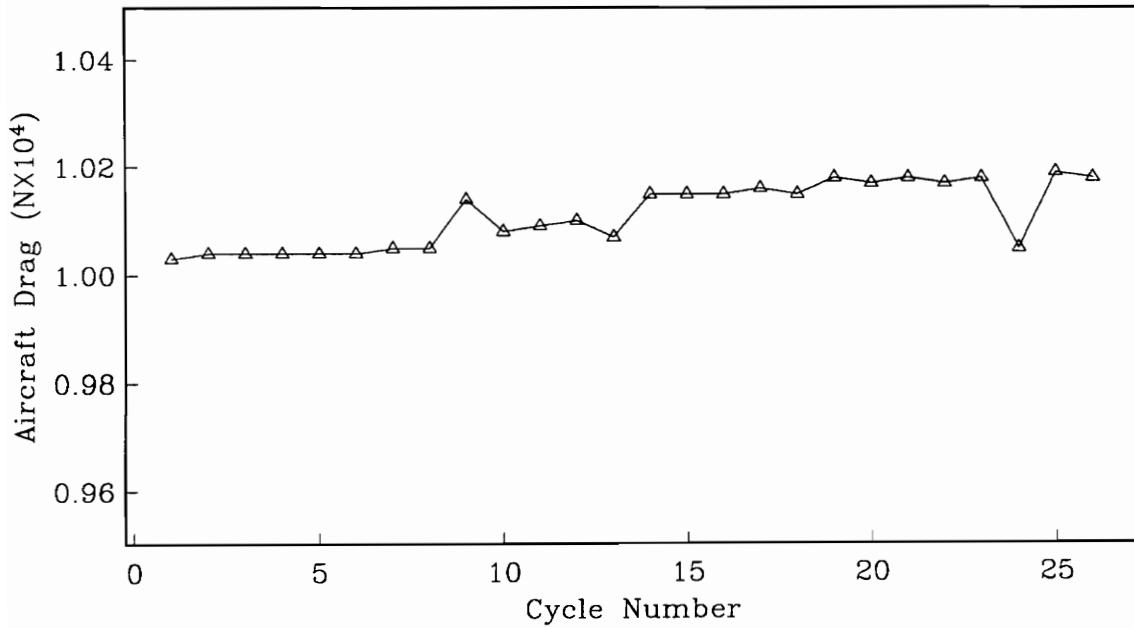**Figure 8.16.** Usable Fuel Weight vs. Cycle Number for Fourth Run



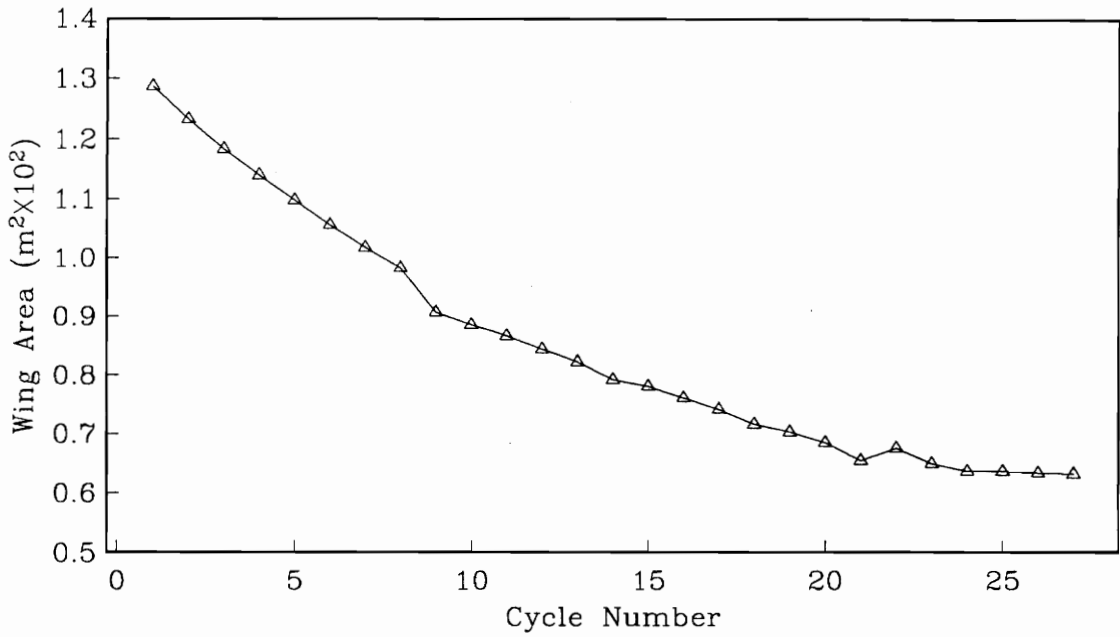**Figure 8.17.** Flexible Wing Drag vs. Cycle Number for Fourth Run

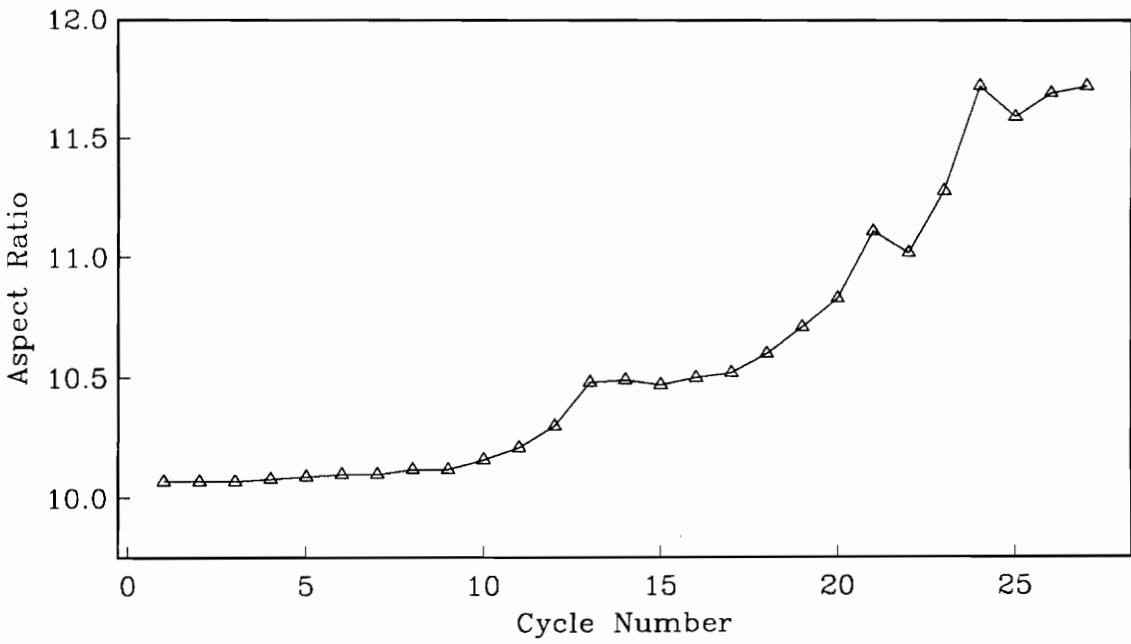**Figure 8.18.** Total Wing Area vs. Cycle Number for Fourth Run



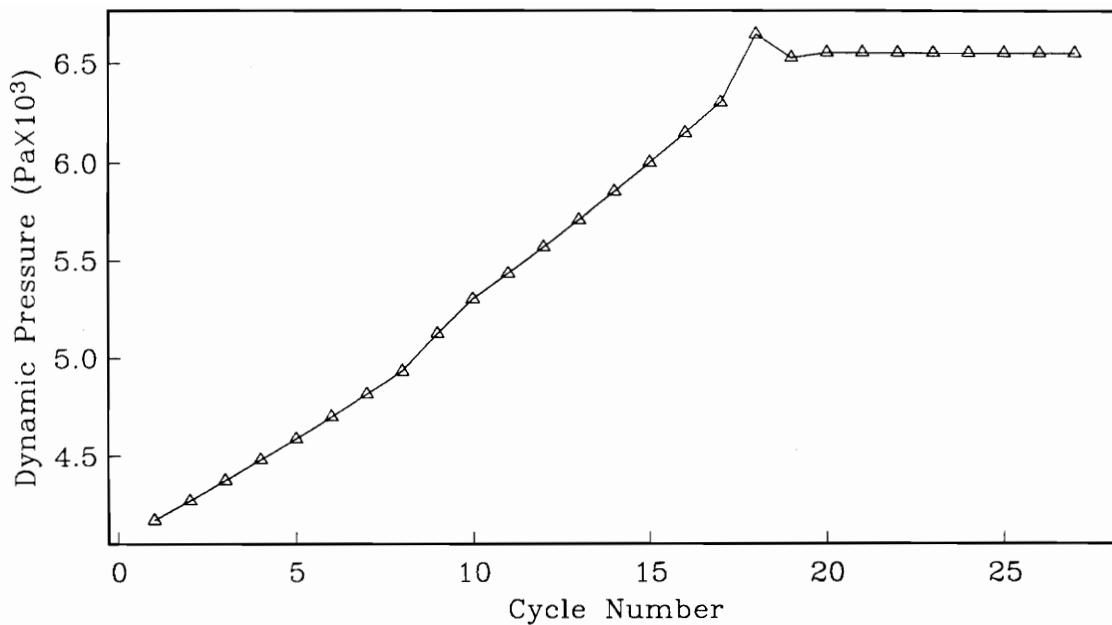**Figure 8.19.** Aspect Ratio vs. Cycle Number for Fourth Run

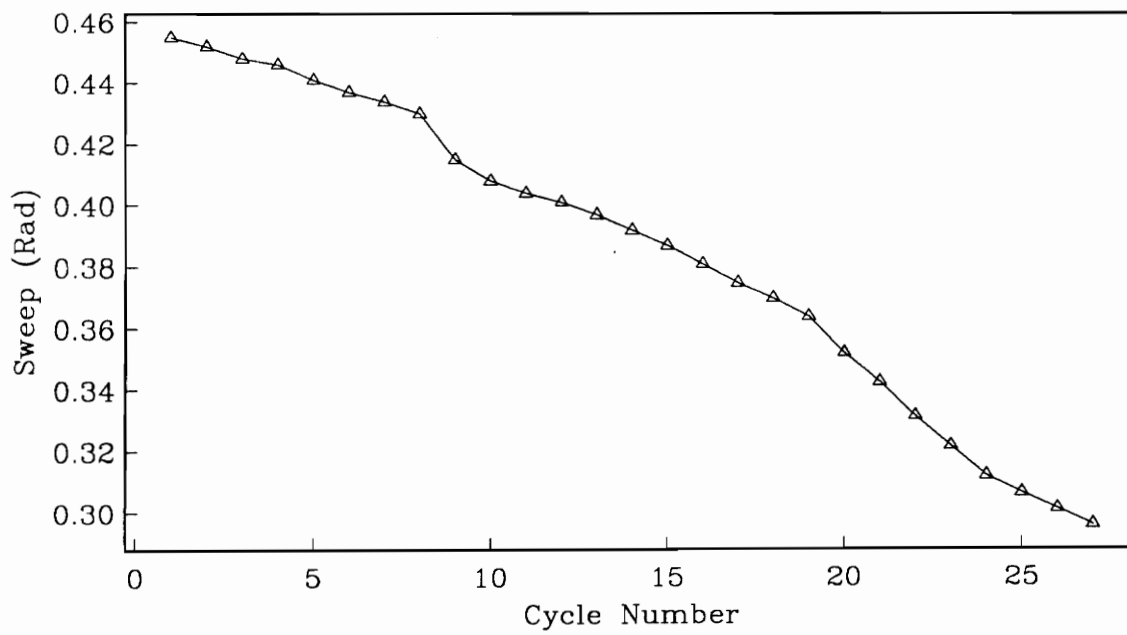**Figure 8.20.** Cruise Dynamic Pressure vs. Cycle Number for Fourth Run



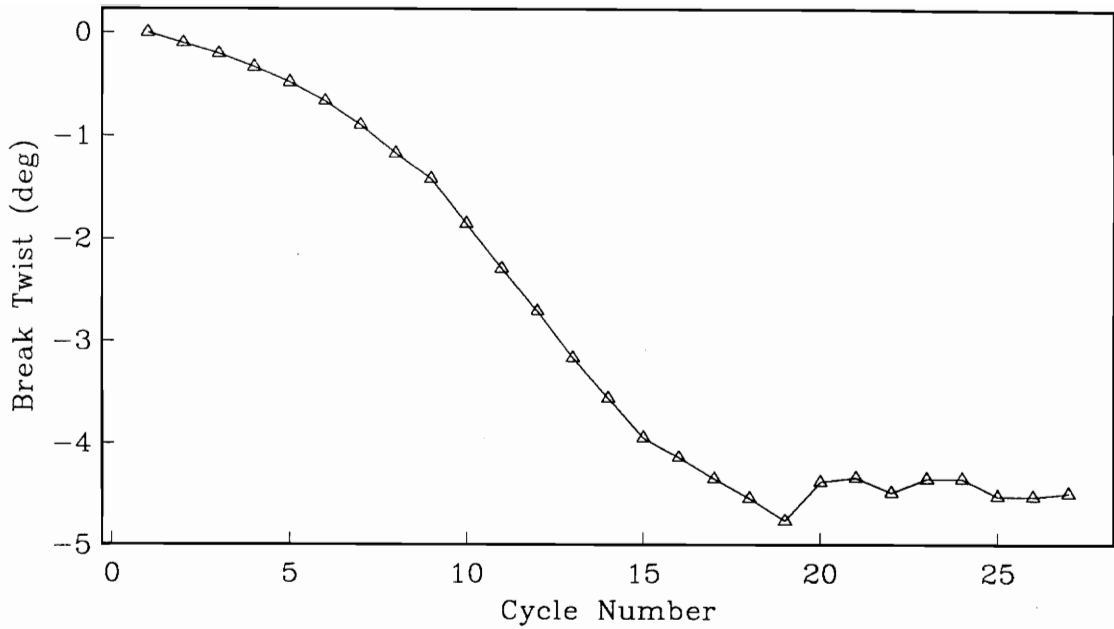**Figure 8.21.** Sweep at Break vs. Cycle Number for Fourth Run

**Figure 8.22.** Break Twist (Jig) vs. Cycle Number for Fourth Run
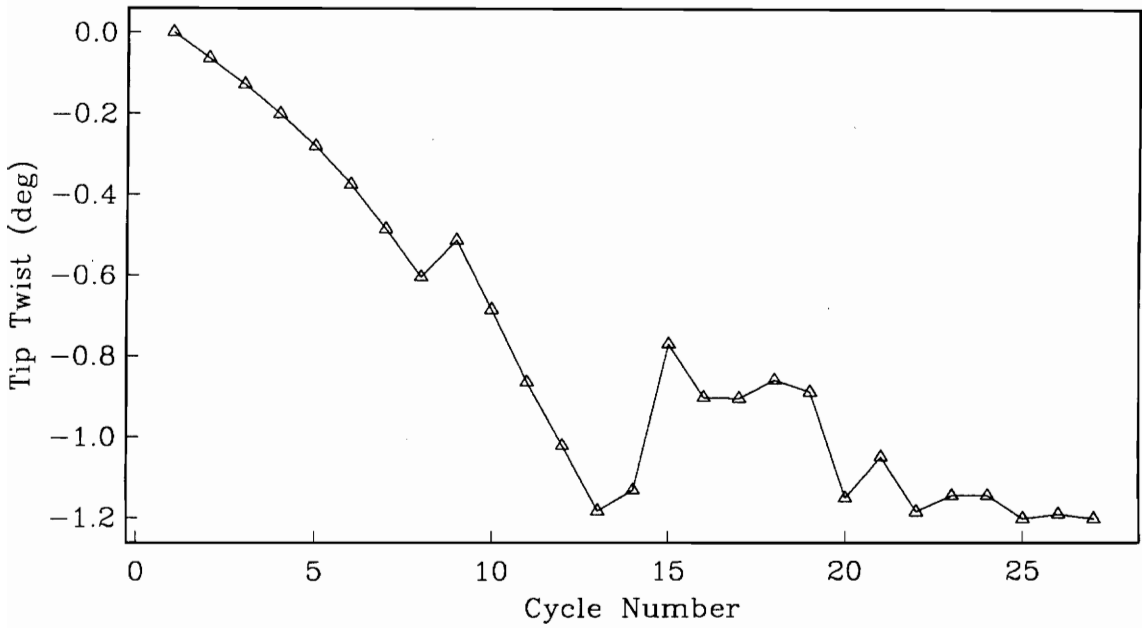


**Figure 8.23.** Tip Twist (Jig) vs. Cycle Number for Fourth Run

## 8.4. Conclusions on the Optimization Process

Table 8.6 gives some of the initial and final set of design variables for the final run. A comparison with the reference aircraft (Table 2.1) reveals that the design aircraft is considerably lighter than that of the reference with similar amounts of fuel. While some of this improvement may be accounted for by the reduced Mach number of the design aircraft, the majority of the reduction comes from the much smaller and lighter wing structure.

**Table 8.6.** Initial and Final Results for Last Run

|  | Initial Design | Final Design |
|---|---|---|
| Gross Weight (N) | $4.581 \times 10^5$ | $4.212 \times 10^5$ |
| Wing Weight (N) | $3.294 \times 10^4$ | $1.609 \times 10^4$ |
| Usable Fuel Weight (N) | $2.738 \times 10^4$ | $2.740 \times 10^4$ |
| Range Margin From Reference | 0.98% | -0.10% |
| Chord Lengths (m) |  |  |
| Root | 6.916 | 4.640 |
| Break | 3.765 | 2.273 |
| Tip | 1.725 | 1.124 |
| Distance from Root to Break (m) | 5.754 | 4.834 |
| Distance from Root to Break (m) | 12.250 | 8.774 |
| Total Wing Area (m$^2$) | 128.7 | 63.22 |
| Aspect Ratio | 10.07 | 11.72 |
| Sweep Angle (deg) | 26.1 | 17.0 |
| Ply Orientation (deg) | 27.2 | 24.4 |

Table 8.7 gives some of the final design results obtained in previous research. Unfortunately, it is difficult to compare these results with the new ones that have been obtained, because the old drag model gave considerably less drag than the new one. Therefore, the previous run had a range surplus at the start which resulted in a very difference final design. Additionally, the old design was only run for 7 cycles.

Table 8.7. Initial and Final Results for Previous Research

| | Initial Design | Final Design |
|---|---|---|
| Gross Weight (N) | $4.391 \times 10^5$ | $4.150 \times 10^5$ |
| Wing Weight (N) | $2.779 \times 10^4$ | $1.728 \times 10^4$ |
| Usable Fuel Weight (N) | $2.190 \times 10^4$ | $1.876 \times 10^4$ |
| | | |
| Range Margin From Reference | 17% | 1% |
| | | |
| Chord Lengths (m) | | |
| Root | 6.916 | 5.912 |
| Break | 3.765 | 3.218 |
| Tip | 1.725 | 1.234 |
| | | |
| Distance from Root to Break (m) | 5.754 | 4.918 |
| | | |
| Distance from Root to Break (m) | 12.250 | 10.443 |
| | | |
| Total Wing Area (m$^2$) | 128.7 | 91.39 |
| | | |
| Aspect Ratio | 10.07 | 10.33 |
| | | |
| Sweep Angle (deg) | 26.1 | 18.8 |
| | | |
| Ply Orientation (deg) | 27.2 | 25.6 |

The optimization procedure revealed interesting interactions between the wing planform and the aircraft weight. The reduction of aspect ratio and a negative twist

distribution, combined with a reduction of wing area were the the optimization's most effective methods to reduce the weight. When a limit on the usable fuel was applied, the aspect ratio was used to offset any drag increases due to the twist distribution. While many more studies are needed into the optimization, the success of the designs indicates that the new sensitivities worked well.

# 9. CONCLUSIONS

The most important accomplishment of this study was a detailed understanding of drag and divergence sensitivity calculations. Associated with that understanding was the ability to greatly improve the accuracy of those calculations over previous work. The calculation error was generally lower than 10% which provided approximations that where very close to the exact tangents of the drag and divergence curves. It was concluded that the majority of the errors from the past could be attributed to the lack of consistency in some of the drag terms and a drag model which produced questionable results.

The improvement in the drag model was provided with a far-field analysis which yielded what was felt to be more reasonable results for drag. An added benefit of the model was a more robust approach which was less sensitive to the wing paneling scheme.

The divergence sensitivity also benefited from this study. While this derivative was never successfully computed in the past, new calculations provided results with accuracy similar to that of the drag sensitivity.

Another important accomplishment was the development of a new model for the aerodynamic–structural interface. This new model employed shape functions over a grid structure defined by the load set nodes. The major advantage of this new approach was the elimination of the discontinuous behavior of the previous interface. Other advantages of the model include a more general and compact interpolation scheme and a considerable reduction in computational times. It is also felt that this shape function approach also contributed significantly to the increased accuracy of the sensitivities.

The study ended with a look at the optimization process and made some observations on the results. These studies also concluded that very tight move limits (3%) were required to keep the structural constraint violations contained. An important topic of future work will be further investigations in the optimization process with a detailed study of additional constraint problems. These additional problems could include fuel minimization and range maximization studies. It is also hoped that future work can determine approaches which will allow much larger move limits.

Another area of future work includes the incorporation of FLOPS[22] which is a flight optimization code for preliminary design. This code would be employed for a more accurate model the aircraft weight. Another obvious improvement to the multi-disciplinary design would be a more accurate aerodynamic model (such as small disturbance theory). While this is an attractive topic for future research, the computational requirements for such a problem are staggering. Preliminary investigations on small disturbance codes (CAPTSD[23] and TRO3D[24]) indicated that the computation times involved in solving the flow field are on the order of 300 times greater than that of the vortex lattice method. This would result in almost 40 hours of CPU time on a IBM 3090 for each optimization cycle. It is clear that a significant amount of research will have to be conducted to reduce this run time to make the problem feasible.

One approach to reducing the necessary number of flow analyses is suggested by Sheena and Karpel[25], who proposed the analysis of the aeroelastic response using vibration modes. With this approach, all deflections are represented with a linear combination of the vibration modes. Since any given object has an infinite number of modes, only the first several are taken into account. While this is only an approximation, it takes relatively few modes to model a problem with sufficient accuracy. This reduced number of degrees of freedom would result in considerable time savings but still not enough to consider a small disturbance model feasible in the immediate future.

# REFERENCES

1. Grossman, B., Strauch, G. J., Eppard W. M., Gurdal, Z. and Haftka, R. T., "Combined Aerodynamic-Structural Design of a Sailplane Wing", *Journal of Aircraft*, Vol. 25, No. 9, pp. 855–860, 1988.

2. Haftka, R. T., Grossman, B., Eppard, W. M., Kao, P.J. and Polen, D. M., "Efficient Optimization of Integrated Aerodynamic-Structural Design", *International Journal for Numerical Methods in Engineering*, Vol. 28, pp. 593–607, 1989.

3. Sobieszczanski-Sobieski, J., "On the Sensitivity of Complex Internally Coupled Systems", AIAA Paper No. CP-88-2378, also *AIAA Journal*, 1989.

4. Polen, D. M., "Integrated Aerodynamic-Structural Design of a Subsonic, Forward-Swept Transport Wing", MS Thesis, Virginia Polytechnic Institute and State University, May 1989.

5. Kao, P. J., "Efficient Methods for Integrated Structural-Aerodynamic Wing Optimum Design", PhD Dissertation, Virginia Polytechnic Institute and State University, March 1989.

6. Grossman, B., Haftka, R. T., Kao, P.J., Polen, D. M., Rais-Rohani, M., Sobieszczanski-Sobieski, J., "Integrated Aerodynamic-Structural Design of a Transport Wing", AIAA Paper No. 89-2129, 1989.

7. Turriziani, R. V., "Continuation of a Study of the Effects of Advanced Technologies on the Sizing and Fuel Efficiency of a 150 Passenger 1220 N.Mi. Airplane", File: 3-92000/5LTR-007, Jan. 1985.
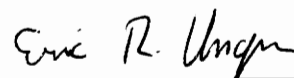
8. Paulson, J. W. Jr., "Applications of Vortex-Lattice Theory to Preliminary Aerodynamic Design", *Vortex-Lattice Utilization*, NASA SP–405, A Workshop Held at Langley Research Center, May 17–18, 1976.

9. Bertin, J. J. and Smith, M. L., "Aerodynamics for Engineers", Prentice Hall Inc., 1979.

10. Moran, J., "An Introduction to Theoretical and Computational Aerodynamics", John Wiley & Sons, Inc., 1984.

11. Mason, W. H., Private Communication, 1989.

12. Margason, R. J. and Lamar, J. E., "Vortex-Lattice Fortran Program for Estimating Subsonic Aerodynamic Characteristics of Complex Planforms", NASA TN D-6142, Feb. 1971.

13. Karamcheti, K., "Principles of Ideal-Fluid Aerodynamics", John Wiley & Sons, Inc., 1966.

14. Ives, D., "LIDRAG", Subroutine for the calculation of the span efficiency, Contained in TRO3D, April 1972.

15. Mason, W. H., "Wing-Canard Aerodynamics at Transonic Speeds - Fundamental Considerations on Minimum Drag Spanloads", AIAA Paper No. 82-0097, Jan. 1982.

16. Viken, J. K., et. al., "Wind Tunnel Results for a High-Speed, Natural Laminar-Flow Airfoil Designed for General Aviation Aircraft", NASA TM-87602, Nov. 1987.

17. Shapiro, A. H., "The Dynamics and Thermodynamics of Compressible Fluid Flow", John Wiley & Sons, Inc., 1953.

18. Haftka, R. T. and Starnes, J. H. Jr., "WIDOWAC: Wing Design Optimization with Aeroelastic Constraints—Program Manual", NASA TM X-3071, 1974.

19. Appa, K., "Finite-Surface Spline", *Journal of Aircraft*, Vol. 26, No. 5, pp. 495–496, May 1989.

20. Reddy, J. N., "An Introduction to the Finite Element Method", McGraw-Hill Book Company, Inc., 1984.

21. Grandhi, R. V., Thareja, R., and Haftka, R. T., "NEWSUMT-A: A General Purpose Program for Constrained Optimization using Constraint Approximations", *ASME Journal of Mechanisms, Transmissions, and Automation in Design*, Vol. 107, pp. 94–99, 1985.

22. McCullers, L. A., "FLOPS: Flight Optimization System—Release 2.0 User's Guide", Oct. 1990.

23. Batina, J. T., Seidel, D. A., Bennett, R. M., and Bland, S. R., "CAP-TSD A Program for Solving the Unsteady Transonic Small-Disturbance Equation for Aeroelastic Analysis of Realistic Aircraft Configurations —Preliminary Users Manual (Version 1.0)", Unsteady Aerodynamics Branch, Langely Research Center, Dec. 1987.

24. Davis, W. H. Jr., Aidala, P. V., and Mason, W. H., "A Study to Develop Improved Methods for the Design of Transonic Fighter Wings by the Use of Numerical Optimization", NASA Contractor Report 3995, August 1986.

25. Shenna, Z. and Karpel, M., "Static Aeroelastic analysis using Aircraft Vibration Modes", Presented at the $2^{nd}$ International Symposium on Aeroelasticity and Structural Dynamics, DGLR Bericht 85-02, Aachen W. Germany, April 1985.

26. Kálmán, P., Giesing, J. P., and Rodden, W. P., "Spanwise Distribution of Induced Drag in Subsonic Flow by the Vortex Lattice Method", *Journal of Aircraft*, Vol.7, No. 6, pp. 574–576, Dec. 1970.

27. Harder, R. L. and Desmarais, R. N., "Interpolation Using Surface Splines", *Journal of Aircraft*, Vol. 9, No. 2, pp. 189–191, Feb. 1972.

28. Rodden, W. P., McGrew, J. A., and Kálmán, P., "Comment on "Interpolation Using Surface Splines" ", *Journal of Aircraft*, Vol. 9, No. 12, pp. 869–871, Dec. 1972.

# VITA

The author was born in Hampton, Virginia on June 14, 1965. In 1983, he attended Virginia Polytechnic Institute and State University (VPI & SU) and entered the engineering CO-OP program. In 1988 he received his B.S. in Aerospace Engineering. Upon completion of his degree, the author married his then fiance, Susan. He then continued his education at VPI & SU to receive his Masters Degree. Upon graduation, the author intends to continue in pursuit of a Ph.D.

_Eric R. Unger_

Eric R. Unger